論文 / 著書情報
Article / Book Information

題目(和文)	
Title(English)	Correlation between triboluminescence and mechanical deformation of ZnS:Mn dispersed in polymeric material
著者(和文)	ﾘｰﾗｰｼｬｳｽｨﾘﾁｬｲ
Author(English)	Sirichai Leelachao
出典(和文)	学位:博士（工学）, 学位授与機関:東京工業大学, 報告番号:甲第10028号, 授与年月日:2015年12月31日, 学位の種別:課程博士, 審査員:中村 吉男,村右 信二,史 蹟,三宮 工,高橋 邦夫
Citation(English)	Degree:, Conferring organization: Tokyo Institute of Technology, Report number:甲第10028号, Conferred date:2015/12/31, Degree Type:Course doctor, Examiner:,,,,
学位種別(和文)	博士論文
Type(English)	Doctoral Thesis

Correlation between triboluminescence and mechanical deformation of ZnS:Mn dispersed in polymeric material

Graduate School of Science and Engineering
Department of Metallurgy and Ceramics Science
Tokyo Institute of Technology

Sirichai Leelachao

Correlation between triboluminescence and mechanical deformation of ZnS:Mn dispersed in polymeric material

A dissertation submitted in partial fulfillment
of the requirements for the degree of
Doctor of Engineering

by

Sirichai Leelachao

Directed by

Professor Yoshio Nakamura

Graduate School of Science and Engineering
Department of Metallurgy and Ceramics Science
Tokyo Institute of Technology

August, 2015

(This page intentionally left blank.)

Abstract

Deformation-induced luminescence of ZnS:Mn phosphors dispersed in polyester resin is investigated using pin-on-disc triboluminescence measuring system and impact testing device. The results shows the emission quantity increases with higher applied force and striking energy; the relationship is expressed in linearity. In addition, several factors such as the volumetric content of phosphors, friction coefficient and contact geometry are found to effectively influence on light emission behavior of the composite. By employing contact mechanics, it allows us to elucidate their contribution and inter-correlations. Therefore, the luminescence is strongly suggested to be expressed as a function of applied stress where the relationship is found to be in non-linear fashion. Alternative theoretical model is also proposed on the basis of thermodynamics and energy conservation. As the phosphors is deformed, the electrons is more energetic due to the piezoelectric enthalpy and thus deliberate form shallow traps. Possibility of finding excited electrons in conduction band is approximated by Fermi-Dirac distribution function and might be quantified as the shift of Fermi level. Theoretical expression is given as $A\left[\exp\left(B\sigma^2\right)-1\right]$ where σ is applied stress; the function is in good agreement to the observed results.

Contents

List of Figures

List of Tables

Chapter 1

Introduction

Luminescence is an optical phenomenon ascribed to a photonic emission from substances. The behavior can be typically recognized in natures; ranging from organic/inorganic compounds to living organisms which has a particular characteristics and properties. For humans, it is resulting into a drastic wide spectrum of applications depending on the type of emissions and the purpose of usages, such as light/photon sources (x-ray tubes, fluorescent light bulbs, white/colored LEDs and LASERs), scientific characterizing equipments and detectors (XRF, ESCA, scintillator, etc.) or leisure products (radium dials, glowsticks). Of course, *luminescence* is generally referred to a visible light emission behavior, that is $380\,\text{nm} < \lambda_{\text{emit}} < 730\,\text{nm}$. If the emitted photons are specifically contributed to sub-atomic levels, it is rather termed as *fluorescence*.

Of all types of luminescence, mechanoluminescence is referred to a visible light emission from a solid upon an external mechanical excitation. It may be further categorized into elastico-, plastico- and fractoluminescence, according to the types of deformation. Although 'triboluminescence' linguistically means an emission as the consequence of rubbing against two bodies, the definition is partly contradict to that of IUPAC which being defined as "*luminescence resulting from the rubbing together of the surface of certain solids. It can be produced, for example, when solids are crushed*" [1]. This is likely to cause an interchangeability among those terms in many literatures.

To avoid confusion, hereafter, in the thesis, 'triboluminescence' will be referred to the following definition unless otherwise mentioned:

Definition 1. *Luminescence as a consequence of two interacting surfaces in relative motion.*

The probably first scientific report of mechanoluminescence is attributed to an observation

from Sir Francis Bacon, a British scholar, in *Novum Organum* mentioned that [2],

> "It is well known that all sugar, whether candied or plain, if it be hard, will sparkle when broken or scraped in the dark."

The phenomenon has also been demonstrated as an blue light spark emitted during crushing of sugar crystals, especially for Wint-O-Green Lifesavers® candy. In general, the results suggested that the emission spectra from a single-crystal sucrose and the candy composed of two components: a near-ultraviolet photons from a gaseous discharge, probably N_2, during the fracture of the surface which resembles a lightning storm and a thermoluminescence and/or fluorescence after fracture. It is believed that the discharged photons are responsible for the characteristic luminescence of sucrose. Full description on experimental procedures are discussed elsewhere [3–5].

In addition to sugary substances, heretofore, several kinds of inorganic compounds have been discovered to exhibit a stress-induced light emission such as coloured alkali halides, doped ZnS, doped $ZnAl_2O_4$, $SrAl_2O_4$:Eu, $SrAl_2O_4$:Eu,Dy or $BaAl_2Si_2O_8$:rare-earth elements [6–13]. Nonetheless, the practical application of mechanoluminescent materials has not been currently established due to very short emission period, in order of hundred milliseconds, yet the prospective use is suggested as the novel nondestructive techniques for damage detections and structural health monitoring systems [9, 14].

1.1 Band theory on electrical properties and luminescence in crystalline materials

For an isolated atom, energy levels where electrons being occupied are discretized as described by the notable Rutherford-Bohr model. Those quantized states, so-called orbitals, contribute to the characteristic spectral lines for individual element. Such energy levels should be multiplied as a number of atoms increases, however, according to Pauli exclusive principle stating that two identical fermions, e.g. electrons, are not able to simultaneously occupy the similar quantum state, an infinitesimally energy splitting takes place and gives rise to broader spectral bands.

With the presence of a periodically arrangement in crystalline solids, i.e. symmetries, a representative diagram of the allowed energy states at different **k**-vectors, called as electronic band structure, are therefore obtainable. Another important parameter describing the number of states at a certain energy level which usually shown along with the band structure diagram is 'Density of states (DOS)'. Recently, a quantum mechanic calculation is employed to generate those diagrams by solving for the solutions of the Schrödinger equations with multiple intra- and inter-atomic interactions. Details of the methods are extensively discussed in many textbooks such as [15].

Bound electrons preferred to occupy in lower energy states in which are named *valence bands* while high-energy empty levels are called *conduction bands* where the delocalized electrons are relatively mobile and contribute to an electric conductivity, mainly in metals and n-type semiconductors. It should be note that positively charged holes are also considered as carriers in p-type semiconductors where those fermions are dominant.

The region between the valence band maximum (VBM) and the conduction band minimum (CBM) where energy states are not available is called as *forbidden gap*, *bandgap* or *energy band*; its value also shared the identical terminology. Such energy gap is generally used to determine the electric conductivity of condensed solids. Insulators are likely to possess considerably large bandgap than that of conductive materials. The explicit criteria is not, nonetheless, well defined.

When the crystals are subjected to the external energy sources such as irradiation or electric field, bounded electrons are being excited. In semiconductors, an electronic transition into conduction bands is possible if the providing energy is sufficiently absorbed. It consequently generates holes in the valence bands; this process is called *absorption* or *excitation*. As lower energy is more preferable, the excited electrons will recombine with holes and release stored energy which is then called *relaxation* process. If a transformation into a lattice vibration does not occur, photons are therefore emitted and being referred to *radiative emission*. The mentioned processes are schematically illustrated as figure 1.1.

By introducing defects into the crystals, intermediate quantum states can be emerged within forbidden gap whose locations depend on the type of imperfections; it is beneficial for alter-

nating an electric properties of semiconductors. Under certain circumstances, the radiative energy levels, attributed to doping elements, which produce visible wavelength of photons are generated. Crystal field theory is usually used to describe the conditions that allows the appearance of the states. The different in the atomic electrostatic fields, due to a substitution of dopants in cation sites of the host crystals, results in further splitting of the spectral bands of the impurities. The behavior have been studied by Japanese researchers, *Tanabe and Sugano*, whom successfully determined the influence of the crystal field strength on the energy splitting of various electronic configurations. As the reference, Tanabe-Sugano diagrams for transition elements are fully provided in the second chapter of [16].

1.2 Characteristics and applications of zinc sulfide

Zinc sulfide is one of the famous IIb-VIb semiconductors which has been widely employed in fields of optic-relating applications, for instance, cathode-ray tube phosphors, thin-films electroluminescence (TFEL) devices, UV-filtered coating layer or optoelectronic devices [13, 16–18] arising from its promising optical and electrical characteristics as a direct-type large value of bandgap [16, 19].

It naturally has two allotropes: a cubic modification, called sphalerite (β) and a polymorphic hexagonal structure named wurtzite (α). They possesses the identical Zn-S coordinate geometry of tetrahedral pattern. According to an equilibrium phase diagram of Zn-S binary system, displayed in figure 1.3, the cubic structure is more thermodynamically stable at room temperature where a phase transformation congruently takes place at about 1,720°C. Piezoelectric properties should be existed since both crystal structures are non-centrosymmetric.

Calculated electronic band structure of cubic ZnS is illustrated in figure 1.4 where s-orbitals of Zn^{2+} cations contribute to the bottom of the conduction bands while the top of the valence bands mainly composes of p-orbitals from sulfur anions [20].

The luminescence properties of doped ZnS was unintentionally discovered by Théodore Sidot, a French chemist, since 1866 during his experiments on the crystal growth via sublimation process. Later, the emission behavior has been confirmed and verified with the copper-

activated ones of which exhibited a phosphorescence. Further details relating to the history of the luminescent doped ZnS phosphors is mentioned elsewhere [16]. In addition to the fact that Mn-doped ZnS produced the most intense emission among other primitive compounds [13], it is likely to be less expensive, effortlessly to be prepared by conventional processes such as ion plating [21] or sputtering technique [17] and commercially available comparing to other synthesized complex luminophors. Therefore, ZnS draws our attention for investigating the luminescence produced by deformation of this alloy system.

Selected important optical, crystallographic properties and mechanical-related coefficients of ZnS employed throughout the thesis are summarized in table 1.1.

1.3 Literature reviews on the history in mechanically driven emission behavior of ZnS phosphors

Despite the stress-induced emission has been discovered for decades, the proposed mechanisms for this phenomenon are very limited, especially for mathematically expressions. Extensive systematical experiments on ZnS crystals had not been fully established until 1960s. *Alzetta et. al* [22] reported that Mn-doped hexagonal ZnS luminophors exhibit luminescence when a hydrostatic pressure was abruptly imposed and released whereas the intensity decays exponentially once the pressure was maintained constant. Moreover, they also found that the integral quantities of emitted light increases with higher magnitude of applied pressure as the following relationship where k is a constant and ΔP is the applied pressure,

$$I = \exp\left[k\left(\Delta P\right)^2\right]. \tag{1.1}$$

Since the emission could be observed regardless of electrical conductivity of pressurized hydraulic fluids, they thus suggested that the stress-induced luminescence should not be attributed to the triboelectrical field generated on the crystal surface by friction in which proposed by *Lenard* [23]. Also, the cleavage of crystals is likely to be improbable explanation due to non-destructive deformation.

Excitation of triboluminescence by elastic and plastic deformation and by fracture of various single crystals had been studied by *Alzetta et. al* (1970). Transverse force, exerting on the center of specimens which freely supported at its ends, was applied and caused bending deformation at different loading rates. Details of the experimental setup are given in [7]. The emission behavior is able to be detected in the elastic deformation region in Mn-doped ZnS, Mn-doped NaCl and X-ray irradiated colored alkali halides. For Mn-activated ZnS phosphors, the intensity monotonously increases with the degree of elastic deformation. At the onset of plastic deformation, light peaks suddenly appear. They found that the maximum of emission peak coincides with the region where the second derivative of force with respect to bending deformation, i.e. an abrupt change in applied force. The influence of loading rate was also investigated as the emission intensity is qualitatively proportional to the rate of deformation whereas the total amount of emitted light is found to be moderately invariant: the energy conservation is likely to be occurred.

Later, USSR scientists were conducting intensively investigation on strain-induced emission of monocrystalline hexagonal ZnS crystals undergoing uniaxial compressive stress. In case of pure samples, the emission could only be taken place when the applied stress was greater than the elastic limit. The luminescence waveform is a series of discontinuous light pulses which mainly constitutes of a broad 3.56 eV emission peak, it is suggested to be an attribution of oxygen impurities [24]. The number of flashes non-linearly increases with increasing applied stress and contributed to the change in the dimension of specimen. As the deformation corresponding to single luminescence pulse is significantly larger than that of the lattice constant, they concluded that the emission is a consequence of a motion and a multiplication of the dislocations. They however emphasized that the observations should not be considered as triboluminescence or an emission produced by friction as reported in [7].

Taking into consideration the nature of dislocations in ZnS phosphors of which inherently being charged, the external electrical environments are obviously to show the significant role on the emission behavior. According to the results observed by *S.I. Bredikhin and S.Z. Shmurak* (1975) [25], an electric field applied on $(10\bar{1}1)$ faces of the crystal of where highly charged dislocations are moving toward strongly causes a change in the total number of light flashes

generated during plastic deformation as well as a remarkable reduction in the pulses occurs when the polarity in which promoting the emission was reversed. They concluded that the phenomenon called as electroplastic effect (EPE) is likely due to a consequence of the applied field that either enhancing or hindering a mobility and a multiplication process of the dislocations, in other words, it is identical to a modification of mechanical behavior.

Yu.A. Osip'yan and V.F. Petrenko (1975) examined the influence of electrical boundaries on the mechanical properties of sphalerite ZnS single crystals [26], whose the crystallographic orientation was prepared to be equivalent to those of [24] and [25]. In addition to the hardening and softening caused by applied electric field, they also reported of interesting observations as a plastic flow stress of the specimen is lowered when $(\bar{1}\bar{1}2)$ and its parallel face were short-circuited; the decrease is independent of the methods and the electrode metals used in the experiments and the deformation induces an electric current flow, in order of picoamperes, in the external circuit in which linearly proportional to the rate of deformation. The current is suggested to be a leakage of the charges emerging onto the surface into an electrometer whose impedance are drastically smaller than that of the crystal.

Manganese- and copper-activated microtwinned ZnS phosphors mainly exhibited pulse-like emission behavior as same as of which produced in the pure crystal. The studies from *S.I. Bredikhin and S.Z. Shmurak* deduced that there is a potential difference developed across the surfaces of the sample as a result of an accumulation of charged partial dislocations during the deformation. Luminescence is produced when the generated field strength overcomes the breakdown threshold; it is analogous to electroluminescence. The voltage drops to zero as photons emitted and the process then starts over. This observation gives an explanation for pulses-like luminescence. In fact, the emission can be induced by an additional stimulation of short-wavelength photon (N_2 laser at $\lambda \approx 340$ nm) even if the threshold voltage is not attained. Light-assisted luminescence is nonetheless described as a result of electroplasticity due to an observation of an abruptly change of birefringence upon the illumination [27].

In addition, a stationary continuous waveform is then observed in the activated crystals whose spectral lines and temperature-dependency resemble those of photoluminescence [28]. Such luminescence is explained as a consequence of the electric field being emanated inside

the space near the core of charged dislocations. The luminescence centers (C) are excited by an interaction with moving dislocations (D); the equation of excitation process is given as $C^+ = C + h$. Tunneling of electrons (e) from the impurities levels into conduction bands are therefore allowed in the presence of the field. Consequently, the excited carriers can radiatively recombine with holes produced earlier and release the energy by photonic emission. A schematic equation is shown as the following:

$$[D] + [C] \rightarrow e + [C^+],$$
$$e + [C^+] \rightarrow [\dot{C}] + h\nu.$$

So far, in spite of the fact the results obtained from above experiments are remarkably pursuant and strongly supportive to the concept of an correlation between luminescence and charged dislocations. However, there are several disadvantages on these mechanisms: the improbable explanation for the emission reported in [22] since dislocation lines are immobile under hydrostatic pressure, the inconsistency of the fact whether the luminescence can occur under the elastic deformation region and the electrical short-circuit condition and the unavailability to a mathematical expression given for the relationship between the luminescence intensity and the applied stress.

Qualitative investigations were initiated by *B.P. Chandra and J.I. Zink* to derive a dynamic expression for time- and impact velocity- dependence of the triboluminescence intensity of single crystalline tartaric acid ($C_4H_6O_6$), sugar, ammonium tartrate ($C_4H_{12}N_2O_6$), lithium-sulfate monohydrate ($Li_2SiO_4 \cdot H_2O$) and citric-acid monohydrate ($C_6H_8O_7 \cdot H_2O$) [29]. A relationship between the maximum intensity and the velocity was, experimentally and empirically, nonlinearity whereas the total emission was found to be saturated at the certain speed, all expressions and derivation can be found in the literature. They suggested that the excitation source of triboluminescence in the crystals is due to the motion of cracks and the creation of freshly new surfaces. Despite the pioneer explicit formulations, the possibility of using the equations for the case of deformation-induced emission of ZnS crystals had not been confirmed.

Although researches on the topic of stress-stimulated emission behavior of various kinds of materials continued and found out that such luminescence also being observed for the case of elastic deformation [8, 13, 17, 21, 30–34], any perspicuous expression and the detailed mechanism particularly for explaining elastico-mechanoluminescence of phosphors was not completely developed and studied, in consequence of that, the proposal of dislocation-associated emission was being accepted.

Eventually, the exact theoretical models describing a relationship between the intensity of luminescence and the mechanical stress or strain in elastic deformation region for irradiated alkali halides, doped strontium aluminate and Mn-incorporated ZnS nanoparticles were established in [35], [36] and [10], respectively. Derivation of the analytical expressions is basically performed in the similar manner to which being used in [29]. In fact, discrepancies in the final formulations among those models are due to the dissimilarity of assumptions utilized in during development.

In case of coloured alkali halide crystals, F-centers corresponds to electrons trapped into anion vacancies [37] of which creating during a bombardment of energized particles. Such centers are responsible for the luminescence. As the point defects are able to be regarded as sources of electrons, that is energetically unstable if being excited [38], it possible to hypothesize the excitation of F-centers are caused by an interaction with a dislocation bending which occurring elastic deformation [6, 39] or its motions when the applied stress exceeds the proportional limit of the crystals [6]. In fact, the excitation also occurred in doping luminescence centers as well [6, 39]. According to the definition described in [37, 38], for pure irradiated crystals, F-centers might be able to be stimulated into the excited states, for instance, by an optical absorption so that the subsequent de-excitation is responsible for fluorescence or photon emission. Meanwhile, the mechanism proposed in [35] suggests that the transition of electrons from the interactive F-centers into dislocation band is a consequence of comparable thermal activation energy (kT = 0.026 eV) to the potential barrier (about 0.1 eV) which is the energy difference between the ground states of the interactive and the non-interactive F-centers. Electrons are then captured into dislocation bands and then transfered to hole centers which subsequently causes an emission.

Some faults of the latter theory are listed here: (i) there is no description on the kind of centers of where holes being occupied and (ii) it is still questionable whether the thermal energy at room temperature is sufficient to surmount the activation and provides a significant transition of carriers since $\exp(-E_a/kT) = \exp(-0.1/0.026) = 2.14\%$. Details on the mathematical derivation, the final expressions and explanation can be found in [35].

On the other hand, the situation should be different in $SrAl_2O_4$-based and ZnS-based phosphors. In the first proposed mechanism for strontium aluminate crystals [36], the mechanoluminescence is explained in respect to the following processes:

Mechanism for doped $SrAl_2O_4$ and its derivatives.

1. Piezoelectric field is produced in the doped crystals by the application of external pressure which is due to the non-centrosymmetric.

2. The field causes a reduction in the trap-depth of hole traps (T).
   $[T^+] \xrightarrow{\text{field}} [T] + \oplus$

3. Holes are generated in the valence band and the traps are then occupied by electrons.

4. Detrapped holes recombine with $(Eu^{1+})^*$ ions and therefore produce the excited $(Eu^{2+})^*$.
   $(Eu^{1+})^* + \oplus \rightarrow (Eu^{2+})^*$

5. Characteristic emission is a result of the de-excitation of $(Eu^{2+})^*$ ions.
   $(Eu^{2+})^* \rightarrow (Eu^{2+}) + h\nu$

Although the important equations are selectively shown on which the conclusions are deduced, one can pursue a full process of the development of mathematical expressions in the original article,

$$P(t) = P_0\left[1 - \exp(-\zeta t)\right], \tag{1.3}$$

$$I_{max}(P_0) \propto \begin{cases} [\exp(\alpha P_0) - 1] & \text{if } P_0 \text{ is high.} \\ (P_0) & \text{if } P_0 \text{ is low.,} \end{cases} \tag{1.4}$$

$$I_{df} = I_{max} \exp\left(-\frac{(t-t_m)}{\tau_f}\right), \tag{1.5}$$

$$I_{df} = I_{max} \exp\left(-\frac{(t-t_0)}{\tau_r}\right), \tag{1.6}$$

where ζ is a machine constant, α is a coefficient, t_m is the time when the maximum intensity attained, t_0 is the time when fast decaying process are negligible, τ_f is a lifetime of the trapped holes and τ_r is a lifetime of detrapped holes in shallow traps which will be released and cause an emission.

According to equation 1.4, the maximum intensity should be proportional to the applied pressure at low stress while a non-linearity may appear for undergoing in moderate deformation. Additionally, the distinctive properties of stress-activated emission of strontium aluminate doped with rare-earth elements, and probably its derivatives, are also mentioned;

- Emission spectra from mechanoluminescence (ML) is identical to that of photoluminescence (PL).
- The ML intensity increases with time and reaches the peak value I_{max} at t_m even the applied load reaches the designated value and kept constant.
- For a post-deformation period, the intensity decreases exponentially with time at two different rates: the fast decay is corresponding to the lifetime of the trapped holes in the compound and a characteristic lifetime of holes in shallow traps is responsible for the slow decay process.
- Piezoelectrification may contribute the emission since the luminescence also observed during unloading of stress which resemble to the generated voltage signal in PZT [40].

The proposed mechanism had been postulated for explaining of mechanoluminescence on manganese-associated zinc sulfide because of the piezoelectricity in both compounds. Although the physical concept and the mathematically deriving processes are intimately identical to that of [36], some differences are distinguishable. In the latter case, electrons are regarded as

mobile carriers and the localized electric field was suggested be sufficiently intense to yield a transition of electrons of which is due to the local change of the host crystal structure adjacent to those impurities [41]. The following steps are proposed to be as a mechanism of mechano-luminescence in ZnS,

Mechanism for doped ZnS phosphors.

1. Piezoelectric field is produced in doped crystals by the application of external pressure which is due to the non-centrosymmetric.

2. The generated field reduces the trap-depth of filled electron traps which allows electrons to be tunneled into the conduction band.

3. A recombination of the excited electrons and holes in which located either in defects or valence band may non-radiatively occur.

4. Non-radiative energy may be responsible for the excitation of Mn^{2+} ions.

5. Characteristic emission is a result of the de-excitation of $(Mn^{2+})^*$ ions.

In previous research [10], an emission peak intensity, an integral quantity of the luminance and a decaying characteristic functions are different from those aforementioned in particular manner since the rate of deformation is taken into consideration. Therefore, a quadratic relationship between the total intensity to the designated applied stress is expected whereas a linearity of the peak emission to the stress is influenced by the deformation rate.In contrast, an effectiveness of the instruments and mechanical response of the specimen turns out to govern the rate of fast-decaying of the luminescence while the slow-decaying process depends on the relaxation of surface charges generated by piezoelectric effect.

$$I_{max} = \begin{cases} k_1 P_0^2 & \\ k_1 P_0 & \text{if the deformation rate, i.e. dP/dt, is constant.,} \end{cases} \tag{1.7}$$

$$I_{total} \equiv \int_{t_c}^{\infty} I dt = k_2 P_O^2, \tag{1.8}$$

$$I_{df} = I_{max}\left[\exp\left(-(\zeta+\gamma)(t-t_m)\right)\right], \tag{1.9}$$

$$I_{ds} = I_{max}\left[\exp\left(-(\gamma)(t-t_m)\right)\right], \tag{1.10}$$

where k_1 and k_2 are a proportional constant containing the influence of (i) localized piezoelectric coefficient and (ii) efficiency of radiative emission of Mn^{2+} centers, $\zeta = 1/\tau_m$ is a machine constant and $\gamma = 1/\tau_q$ when τ_q is a time constant of the relaxation process of surface charges.

So far, it can be generally seen that the luminescent intensity, both of the maximum and the integral value, should transiently increase with higher loading stress with the specified relationship depending on several measuring conditions and/or other physical parameters, e.g. the rate of deformation, the magnitude of the applied force or temperature.

1.4 Current research themes relating on the mechanoluminescent phosphors

1. *Proposal of explanatory mechanisms and mathematical expressions*

   As aforementioned in section 1.3.

2. *Improvement of new high-performance phosphors and its synthesizing process*

   In spite of the availability and inexpensiveness of doped ZnS phosphor, its thermal stability, emission intensity and persistence, i.e. a period of luminescence being observed after removal of the excitation source which is often measured as the lifetime, are likely to be inferior to doped monoclinic $SrAl_2O_4$, the improvement of the luminescent properties of ZnS becomes remarkably incomprehensive. Other host crystals being investigated are ranging from the chemically-synthesized metal complexes such as tetrakis (dibenzoylmethide)-triethylammonium to the complexed mixture of oxides, including alloyed-$SrAl_2O_4$, alloyed-silicates ($SrCaMgSi_2O_7$, for example), alloyed-aluminates or alloyed-titanates. Further lists can be found in [9, 11, 14, 42].

3. *Development of acquisition setups and measurements*

   Apart from typical compression or frictional tests, the deformation may be introduced to samples by different methods such as a direct impact [31, 43, 44], a three-points bending [45], a cyclic loading [46, 46] or a torsion [47].

4. *Identification and proposal of practical applications*

   Mechanical parameters are able to be estimated by converting the deformation into other measurable forms such as electrical output (strain gauges and transducers), a change of optical birefringence (a photoelastic effect) or a positional difference of laser-reflecting method, however, each technique has unique benefits and disadvantages which governing the suitability for specific uses. By using of mechanoluminescent-based technique, it may applicable to services of which require a visual detection without wiring connection.

1.5 Objectives and scopes of the study

Despite the claims that the proposed empirical relationships are in accordance to various observations, in fact, it seems that *B.P. Chandra* and his colleagues have been currently attempting to revise their mathematical models for elastic deformation-induced emission behavior of IIb-IVb semiconductors and doped strontium aluminate crystals which results in several literatures recently published [11, 48–53]. Oddly, only the definitions and assumptions on particular functions and parameters with some mathematical treatments are selected to be intemperately modified while the overall underlying concept remains merely unchanged. For instance, an idea of the decrement of piezoelectric charges is utilized in [49–51] instead of considering the time constant of excited electrons in conduction band [11, 48] without any explanation or supporting evidence.

Of course, theoretical formulations should be changed due to the differences in analytical approaches, however, it is quite doubtful whether the assumptions using in dissimilar models are considerably interchangeable or equivalent.

Since the emission is a characteristic property to phosphors, the influence of its volume fraction (demonstrated in [34, 44, 45, 54, 55]) as well as the presence of multiple crystallo-

graphic phases on the emission intensity should be importantly taken into consideration during development of the theoretical models for the case of a composite containing non-emittable components.

Moreover, at the present time, a specialized mechanoluminescence measuring setup is not commercially available, most researches are relying on a simple combination of mechanical testing machines and the optical detectors; these approaches may be acceptable for whose configuration does not cause a significant blockage of light path. However, the triboluminescent emission is likely to be probed by sensors locating adjacent to a non-transparent sliding pin [13], an optical obstruction is unavoidable and may result in the error for quantitative analyses, therefore, it is essential to develop the customized measuring instrument which is most suitable for the experiments.

In summary, the objectives of the study are addressed as below,

1. Understanding a relationship between deformation-induced luminescence of ZnS:Mn and mechanical stimulations, i.e. forces or stresses.

2. Proposal of alternative mechanism for elastico-triboluminescence of Mn-doped ZnS phosphors embedded in polymer matrix as a consequence of piezoelectric coupling energy.

3. Demonstration of the applicability of theoretical expressions modeling for the composite of non-luminescent transparent polymeric matrix and phosphors.

1.6 Organization of the thesis

Chapter 1 Introduction: Fundamental of phosphors, the properties of luminescent doped ZnS crystals, a chronicle of development of mechanism and mathematical formulations, the current research themes on for mechanoluminescence as well as the objectives of the study are given here.

Chapter 2 Construction of triboluminescence acquisition instrument: The chapter includes basic principles regarding to the construction of pin-on-disc triboluminescence system and its validation test.

Chapter 3 Estimation of mechanical behavior of phosphor-embedded composite: Analytical methods utilized for an estimation of mechanical properties of particulate composite of luminophors/polymeric matrix and contact stresses exerted during sliding motion are discussed.

Chapter 4 Influence of applied loads on triboluminescence behavior of the particulate luminescent composites: Experimental observation of triboluminescence at different loading conditions and volume fractions of phosphor are shown in the chapter.

Chapter 5 Mechanoluminescence and its correlation to impact energy and contact geometry: Additional experiment to investigate the effect of different contact geometry on mechanoluminescence by means of impact testing.

Chapter 6 Mechanism and its mathematical expressions of stress-induced luminescence of ZnS:Mn phosphors: A logical flow of thoughts which give rise to theoretical expressions on the basis of piezoelectricity are discussed.

Chapter 7 Applicability of the proposed mechanism and discussions: Obtained experimental results are quantitatively analyzed using the proposed theoretical models. Physical explanation for individual parameters appeared in the models are also mentioned.

Chapter 8 Conclusions: General conclusions deduced from the study are given in this chapter.

Reference

[1] Verhoeven, J. *Pure and Applied Chemistry* **68**(12), 2223–2286 (1996).

[2] Bacon, F. `http://web.lemoyne.edu/~GIUNTA/bacon.html`, (1620). Online; accessed October, 2012.

[3] Dickinson, J., Brix, L., and Jensen, L. *J. Phys. Chem.* **88**(9), 1698–1701 (1984).

[4] Sweeting, L. `http://pages.towson.edu/ladon/wg/candywww.htm`, Septempber (1998). Online; accessed October, 2012.

[5] Chang, K. `http://www.nytimes.com/2007/06/19/science/19winto.html?_r=0`, June (2007). Online; accessed October, 2012.

[6] Shmurak, S. Z. *Sov. Phys.-Solid State* **10**(7), 1526–1530 (1969).

[7] Alzetta, G., Chudáček, I., and Scarmozzino, R. *Phys. Stat. Sol. (a)* **1**, 775–785 (1970).

[8] Akiyama, M., Xu, C., Matsui, H., Nanoka, K., and Watanabe, T. *Appl. Phys. Lett.* **75**(17), 2548–2550 (1999).

[9] Olawale, D., Dickens, T., Sullivan, W., Okoli, O., Sobanjo, J., and Wang, B. *J. Lumin.* **131**, 1407–1418 (2011).

[10] Chandra, B., Xu, C., Yamada, H., and Zheng, X. *J. Lumin.* **130**, 442–450 (2010).

[11] Chandra, V. and Chandra, B. *Opt. Mater.* **34**, 194–200 (2011).

[12] Matsui, H., Xu, C., Liu, Y., and Tateyama, H. *Phys. Rev. B* **69**, 235109 (2004).

[13] Xu, C., Watanabe, T., Akiyama, M., and Zheng, X. *Mater. Res. Bull.* **34**, 1491–1500 (1999).

[14] Xu, C. *Mechanoluminescence and Novel Structural Health Diagnosis*. NTS shuppan, (2012).

[15] Hamaguchi, C. *Basic Semiconductor Physics*. Springer-Verlac, (2001).

[16] Yen, W., Shionoya, S., and Yamamoto, H. *Fundamentals of Phosphors*. CRC Press, (2007).

[17] Agyeman, O., Xu, C., Suzuki, M., and Zheng, X. *J. Mater. Res.* **17**(5), 959–963 (2002).

[18] Boutaud, G., Cranton, W., Koutsogeorgis, D., Ranson, R., Tsakonasm, C., and Thomas, C. *Mater. Sci. Eng., B* **165**(3), 202–206 (2009).

[19] Shimaoka, G., Arakawa, T., and Suzuki, Y. *Appl. Surf. Sci.* **212–213**, 694–700 (2003).

[20] Eckelt, P., Madelung, O., and Treusch, J. *Phys. Rev. Lett.* **18**(16), 656–658 (1967).

[21] Xu, C., Watanabe, T., and Akiyama, M. *J. Am. Ceram. Soc.* **82**(9), 2342–2344 (1999).

[22] Alzetta, G., Minnaja, N., and Santucci, S. *Il Nouvo Cimento* **23**, 910–913 (1962).

[23] Lenard, P. *PHand. der Exp. Phys.; Fluorescenze und Phosphorescenz*.

[24] Bredikhin, S. I. and Shmurak, S. Z. *JETP Lett.* **19**(12), 367–368 (1974).

[25] Bredikhin, S. and Shmurak, S. *JETP Lett.* **21**(6), 156–157 (1975).

[26] Osip'yan, Y. A. and Petrenko, V. F. *Sov. Phys.-JETP* **42**(4), 695–696 (1975).

[27] Bredikhin, S. and Shmurak, S. *Sov. Phys.-JETP* **46**(4), 768–773 (1977).

[28] Bredikhin, S. and Shmurak, S. *Sov. Phys.-JETP* **49**(3), 520–524 (1979).

[29] Chandra, B. and Zink, J. *Phys. Rev. B* **21**(2), 816–826 (1980).

[30] Akiyama, M., Xu, C., Matsui, H., Nanoka, K., and Watanabe, T. *Appl. Phys. Lett.* **73**(21), 3046–3048 (1998).

[31] Xu, C., Watanabe, T., Akiyama, M., and Zheng, X. *Appl. Phys. Lett.* **74**(9), 1236–1238 (1999).

[32] Shon, K.-S., Seo, S., Kwon, Y., and Park, H. *J. Am. Ceram. Soc.* **85**(3), 712–714 (2002).

[33] Akiyama, M., Xu, C., Liu, Y., Nanoka, K., and Watanabe, T. *J. Lumin.* **97**(1), 13–18 (2002).

[34] Jia, Y., Yei, M., and Jia, W. *Opt. Mater.* **28**(8–9), 974–979 (2006).

[35] Chandra, B. *J. Lumin.* **128**(7), 1217–1224 (2008).

[36] Chandra, B., Baghel, R., Luka, A., Sanodiya, T., Kuraria, R., and Kuraria, S. *J. Lumin.* **129**(7), 760–766 (2009).

[37] Muto, T. *Prog. Theor. Phys.* **4**(2), 181–192 (1949).

[38] Pick, H. *Del Nouvo Cimento* **7**(2), 498–522 (1958).

[39] Senchokov, F. and Shmurak, S. *Sov. Phys.-Solid State* **12**(1), 6–8 (1970).

[40] Xu, C., Akiyama, M., Nanoka, K., and Watanabe, T. *IEEE Trans. Ultrason., Ferroelectric, Freq. Control* **45**(4), 1065–1070 (1998).

[41] Chudáček, I. *Czech. J. Phys. B* **16**(6), 520–524 (1966).

[42] Sage, I. and Bourhill, G. *J. Mater. Chem.* **23**(2), 231–245 (2001).

[43] Fontenot, R., Hollerman, W., Aggarwal, M., Bhat, K., and Geodeke, S. *Measurement* **45**(3), 431–436 (2012).

[44] Dickens, T., Olawale, D., Sullivan, W., Breaux, J., Okoli, O., and Wang, B. *Proc. SPIE* **7981**, 79810J–79810J–13 (2011).

[45] Dickens, T., Breaux, J., Olawale, D., Sullivan, W., and Okoli, O. *J. Lumin.* **132**(7), 1714–1719 (2012).

[46] Jeong, S., Song, S., Lee, S., and Choi, B. *Appl. Phys. Lett.* **102**(5), 051110–1–5 (2013).

[47] Kim, G. and Kim, J. *Meas. Sci. Technol.* **25**(1), 1–6 (2014).

[48] Chandra, B., Baghe, R., and Chandra, V. *Chalcogenide Letters* **7**(1), 1–9 (2010).

[49] Chandra, B. *The Open Nanoscience Journal* **5**, 45–58 (2011).

[50] Chandra, B. *Int. J. Lumin. Appl.* **2**(3), 44–72 (2012).

[51] Tiwari, R., Dubey, V., and Chandra, B. *Mater. Phys. Mech.* **19**, 25–38 (2014).

[52] Chandra, V., Chandra, B., and Jha, P. *Appl. Phys. Lett.* **103**(16), 161113–1–5 (2013).

[53] Chandra, B., Chandra, V., and Jha, P. *Appl. Phys. Lett.* **104**(3), 031102–1–5 (2014).

[54] Someya, S., Ishii, K., Saeki, M., and Munakata, T. *Opt. Lett.* **38**(7), 1095–1097 (2013).

[55] Ishii, K., Someya, S., Saeki, M., and Munakata, T. *T. Jpn. Soc. Mech. Eng. C* **79**(806), 3721–3731 (2013).

[56] Sharma, R. and Chang, Y. *J. Phase Equilib.* **17**(3), 261–266 (1996).

[57] Ludeke, R. *J. Vac. Sci. Technol.* **8**(1), 199–209 (1971).

[58] Chung, D. and Buessem, W. *J. Appl. Phys.* **38**(6), 2535–2540 (1967).

[59] Cline, C., Dunegan, H., and Henderson, G. *J. Appl. Phys.* **38**(4), 1944–1948 (1967).

[60] *JAMME* **31**(1), 29–34 (2008).

[61] Kobyakov, I. *Soviet. Phys.-Cryst.* **11**(3), 369–370 (1966).

[62] Martin, R. *Phys. Rev. B* **1**(10), 4005–4011 (1970).

[63] Berlincourt, D., Jaffe, H., and Shiozawa, L. *Phys. Rev.* **129**(3), 1009–1017 (1963).

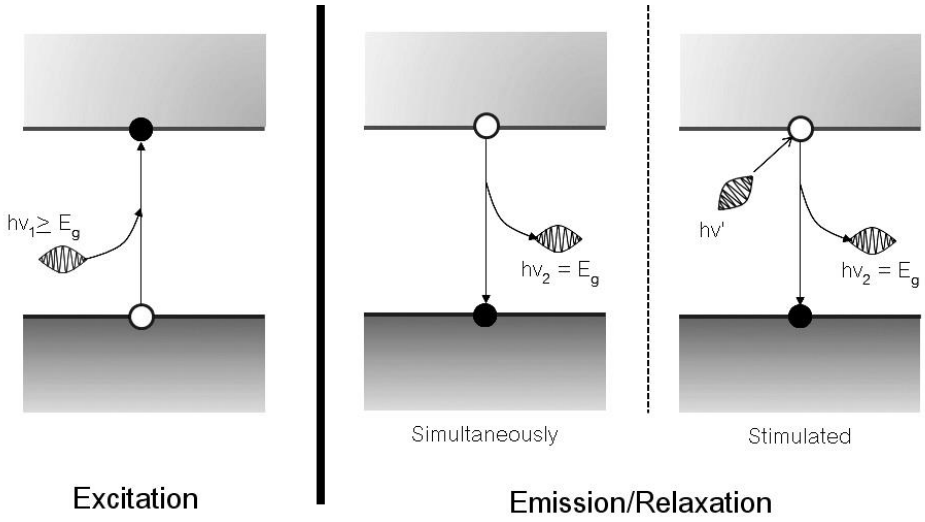

Figure 1.1: Schematic diagram of a process of excitation and radiative emission when subjected to an irradiation.

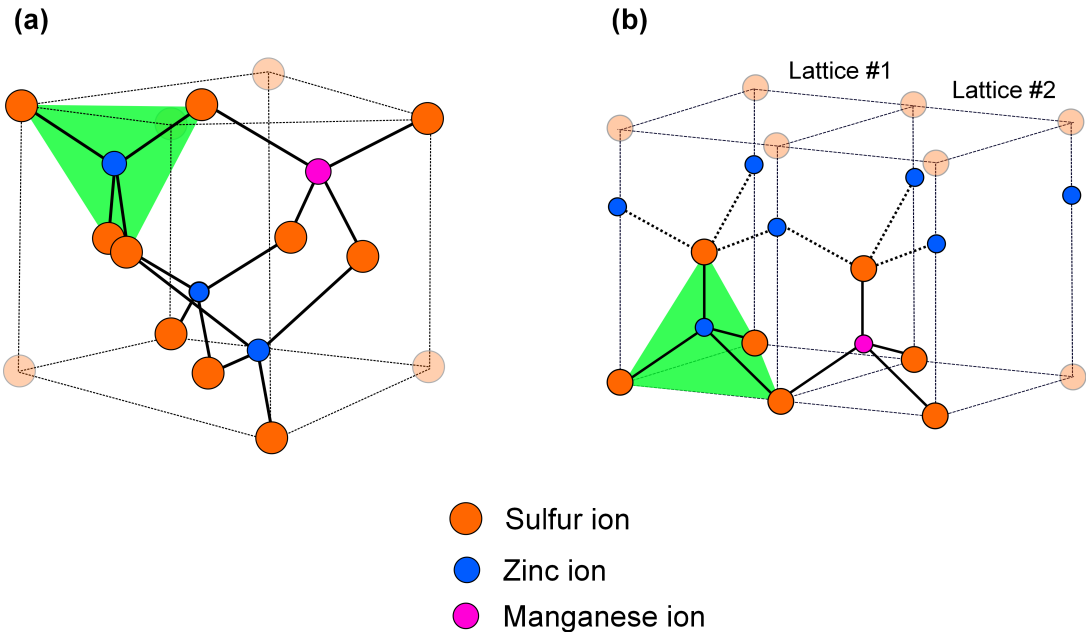

Figure 1.2: Two allotropes of ZnS (a) cubic sphalerite, space group of $F\bar{4}3M$ and (b) hexagonal wurtzite, space group of P63MC. Green shaded region represents tetrahedral coordinate of the structures.

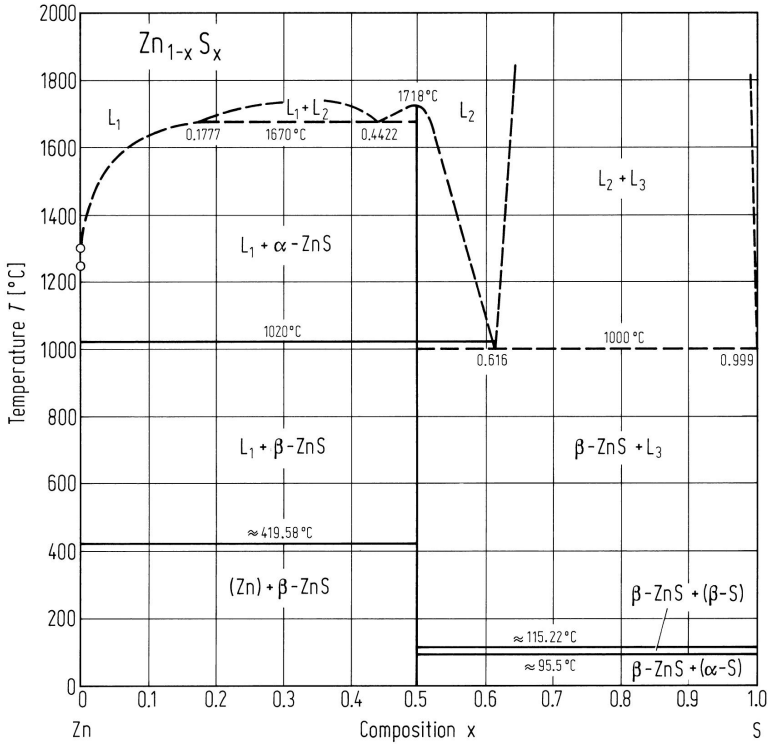

Figure 1.3: Zn-S phase diagram. (Reprinted from [56])

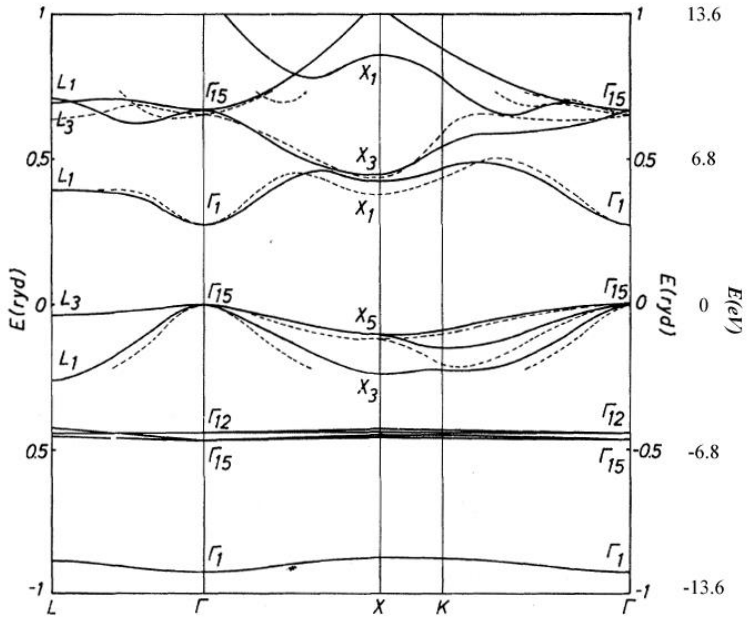

Figure 1.4: The electronic band structure of sphalerite ZnS calculated by KORRINGA-KOHN-ROSTOKER method. (Reprinted from [20])

Table 1.1: Summary of related optical, physical and mechanical constants of crystalline ZnS at room temperature.

Corresponding parameters		**Cubic sphalerite (β)**	**Hexagonal wurtzite (α)**
Lattice constant (Å)		a = 5.4093 [a]	a = 3.820 [a] c = 6.260 [a]
Bandgap (eV)		3.66 [b]	3.87 $\perp$c [b]
Effective mass	m_e^*/m_0	0.34 [b]	0.28 $\perp$c [b]
	m_h^*/m_0	-	0.49 $\perp$c [b] 1.4 $\parallel$c [b]
Young modulus (GPa)		83.8 [c]	90.622 [d]
Poisson ratio		0.28 [c]	0.415 [d]
Dielectric constant ($/\varepsilon_0$)	ε_{11}	8.37 [e]	8.7 [f]
	ε_{33}	-	8.7 [f]
Elastic stiffness (GPa)	C_{11}	104.0 [g]	124.2 [d]
	C_{12}	65.0 [g]	60.1 [d]
	C_{13}	-	45.5 [d]
	C_{33}	-	140.0 [d]
	C_{44}	46.2 [g]	28.6 [d]
	C_{66}	-	32.0 [d]
Elastic compliance (GPa^{-1})	s_{11}	1.8817 x 10^{-2} [c]	1.112 x 10^{-2} [f]
	s_{12}	-0.709 x 10^{-2} [c]	-0.456 x 10^{-2} [f]
	s_{13}	-	-0.14 x 10^{-2} [f]
	s_{33}	-	0.847 x 10^{-2} [f]
	s_{44}	2.2173 x 10^{-2} [c]	3.44 x 10^{-2} [f]
	s_{66}	-	3.14 x 10^{-2} [f]
Piezoelectric strain constants (pC N^{-1})	d_{14}	3.18 [h]	-
	d_{13}	-	-1.134 [f] -
	d_{33}	-	3.235 [f] -
	d_{15}	-	-2.802 [f] -

[a] Reference [16].
[b] Reference [57].
[c] Reference [58].
[d] Reference [59].
[e] Reference [60].
[f] Reference [61].
[g] Reference [62].
[h] Reference [63].

Chapter 2

Construction of triboluminescence acquisition instrument

In tribological researches, a performance of hard-coatings and lubrications is commonly evaluated by a rate of wear, a morphology and character of wear tracks or a friction coefficient. Those parameters, however, depend greatly on various factors such as types of materials and its counterparts, operating modes (pin-on-disc or ball-on-disc, for instance) and experimental conditions, it therefore makes such experiments extremely delicate and complicated [1].

To measure tribological quantities, a tribometer is used for introducing abrasion onto the surface of specimen and measuring the frictional force in which estimated from the deflection of the elastic arm. While the wear rate and track morphology are subsequently observed by scanning electron microscope or profilometer, the coefficient of friction μ can be determined as the ratio between the measured lateral force f and the applied load W, a magnitude of normal force can be either assumed to equal to a weight of mass blocks or determined by the same manner to that of used for friction force determination, depending on machine configurations,

$$\mu = \frac{f}{W}. \tag{2.1}$$

Hence, an observation of triboluminescence can be carried out by an installation of optical measuring equipments onto a tribometer.

Figure 2.1 illustrates a schematic drawing of the designed triboluminescence measuring system which mainly composed of three segments: (i) a mechanical loading mechanism (ii) a load determination circuit and (iii) optical measuring systems.

2.1 Mechanically loading mechanism [2, 3]

Machine frame consists of two thick steel plates with 4 supporting pillars. Sample stage is an assemble of bearing-supported aluminum plate which driven by conveyor belt connecting to a speed-controllable motor. Sliding pin attached to an elastic arm is stationary relative to a rotation of the mounted sample; it resembles a pin-on-disc operational tribometer. A horizontality of the system is determined by a tabular spirit level.

By controlling a tensional force in a threaded cable, the exerting normal load is then adjustable without interfering an optical isolation of the system.

2.1.1 Elastic beam

For a high-accuracy determination of friction coefficient, the frictional and the normal applied force are simultaneously recorded during the experiments. Dimensions of the designed beam are given in figure 2.3, it is made of poly (methyl methacrylate) (PMMA) thermosetting polymer with young modulus of about 3.2 GPa at room temperature [4].

Bending strains were measured by miniature general-purpose strain gauges with resistance of 120 Ω (KFG-2-120-C1 series). For normal force determination, a single gauge was attached to top surface of loading section of the arm at a distance of 15 mm horizontally away from a fulcrum which corresponding to a position of a bearing pin. The friction force is evaluated from two gauges connected-in-series attached on the side of the beam section which a sliding pin is mounted. For the latter configuration, each gauge was 15 mm horizontally away from the fulcrum and $\pm$ 10 mm from a vertical neutral axis of the beam; a minimization of the error attributed to the strain produced by twisting is expected.

Normal load

According to a free body diagram of the arm represented in figure 2.4, it can be seen that a magnitude of force acting on the specimen equals to that of provided from the cable. Also, one can express the internal moment $m_N = W \times L.$ at the center of the gauge as the following equation where L (97.5 mm) is a distance from the gauge to a location where the cable attached

and W is a tensional force,

Compressive stress and strain at the center of the gauge can be therefore described as Eq. 2.2a and Eq. 2.2b accordingly, where M is an internal moment, y is a distance from its neutral axis to the top surface, I is a second-moment of inertia and b (10 mm) and h (30 mm) is a width and height of the cross-section respectively,

$$\sigma_N = \frac{My}{I} = \frac{m_N \cdot (h/2)}{(bh^3/12)} = \frac{6WL}{bh^2}, \tag{2.2a}$$

$$\varepsilon_N = \frac{WL}{E} \cdot \frac{6}{bh^2}. \tag{2.2b}$$

Frictional load

It is possible to consider the arm subjected to the lateral force as a simple cantilever beam due to a restriction of horizontal displacement at the bearing pin. Regarding to figure 2.5 and the identical approaches, one can derive formulations for the stress and strain occurring at the center of the beam where b is 30 mm and h is 5 mm. Coefficient of friction is denoted by μ,

$$m_f = \mu W \times L, \tag{2.3a}$$

$$\sigma_f = \frac{My}{I} = \frac{m_f \cdot (h/2)}{(bh^3/12)} = \frac{6\mu WL}{bh^2}, \tag{2.3b}$$

$$\varepsilon_f = \frac{\mu WL}{E} \cdot \frac{6}{bh^2}. \tag{2.3c}$$

For a single-active gauge configuration, the output voltage from strain ε is expressed as the following equation where v is an excitation voltage in Wheatstone bridge and G is a gauge factor of the gauge; the value is 2.14 for KFG-2-120-C1.

$$\Delta V_{bridge} \approx \frac{\varepsilon \cdot v \cdot G}{4} \tag{2.4}$$

2.1.2 Sliding pin

Soda-lime glass rod was chosen as a sliding pin material since it can be used as a direct waveguide for a transmission of the emitted photons to the optical measuring equipments during experiments which may avoid a light blockage by the components. Two difference ends of the stylus were intentionally prepared: (i) a round hemispherical end ($\phi \approx 5$ mm) utilized as a focusing lens being coupled to the optical fiber probe and (ii) a sharp tip with a diameter of 825 μm was manually formed by grinding process in order to intensify the contact stress exerting on the sample surface. Both ends were fine-polished with 0.3 μm alumina suspension to prevent any surface scattering loss. Figure 2.6 is an image of the contacting end taken by an optical microscope.

2.2 Strain amplifying circuit

The strain gauge signal is amplified by an amplifying circuit that constructed from operational amplifying ICs. The amplified signals are measured by a multichannels GL900, Graphtec^{TM} data logger, simultaneously with the signal of photomultiplier tube.

2.2.1 Electronic circuit diagram

Figure 2.7 provides an electrical diagram of the constructed circuits. Strain gauge (SG1 and SG2) is connected to Wheatstone bridge composing of 3 constants 1%-tolerance resistors (Rb) as dummy gauges, the value is 120 Ω and 240 Ω for the normal force and the frictional force determination, respectively. Additional fixed 3 kΩ resistor (Rn4) and a 10 kΩ potentiometer (VR1) were connected to the bridge for balancing and adjusting the output signal [5]. Dry-cell alkali battery at about 1.50 V was used as the excitation source to minimize high-frequency input noise.

A ratio of the output to the input signal is called *gain* and generally adjusted by resistors (Rg) using in the amplifying circuit. Characteristic equation for calculating the gain is given in the datasheet. For a LT1167 high-precision instrumentation op-amp (Linear Technology,

United States) utilizing in the circuit, the equation is given by,

$$A = 1 + \frac{4.94 \times 10^4}{Rg}. \tag{2.5}$$

In this study, an amplifying circuit are constructed from two cascading op-amps for better bandwidth performance. The total gain is a arithmetic multiplication of the gain in each stages, i.e. $A_{total} = \prod_i A_i$. Dual-supply configuration was utilized for expanding the working range; a theoretical voltage difference span should be 18 volts ($\pm 9\mathrm{V}_{cc}$, also supplied by dry-cell batteries). Nonetheless, it is impossible to reach the expected rails due to the properties of LT1167 op-amp.

2.2.2 Evaluating and validating test of the circuit

To achieve high-accuracy, an equivalence of 4-probes measurement was carried out to calculate resistance value using a Keithley$^{\mathrm{TM}}$ 2000 multimeter, at different constant DC currents in which supplied by a Advantest$^{\mathrm{TM}}$ R6142 DC voltage/current generator. The testing configuration is illustrated as figure 2.8. A resistance is a reciprocal of the slope determined form the plot of response voltages. Table 2.1 shows the results with calculated value of gain factors.

Introducing the gain factor into Eq. 2.4, the applied normal load and friction force can be calculated from measured voltages by using the following equations, respectively.

$$W = \frac{2E b_N h_N^2}{3\nu G L A_N} \cdot \Delta V_N \tag{2.6a}$$

$$\mu W = \frac{2E b_f h_f^2}{3\nu G L A_f} \cdot \Delta V_f. \tag{2.6b}$$

A coefficient of friction can be calculated by dividing Eq. 2.6b with Eq. 2.6a,

$$\mu = \frac{b_f h_f^2 A_N}{b_N h_N^2 A_f} \cdot \frac{\Delta V_f}{\Delta V_N} \tag{2.7}$$

To verify a reliability of the circuit, the friction coefficient of 100% polyester resin were measured and compared to the reported literature value. Disc samples with diameter of 30 mm were prepared by casting process of a generic polyester resin mixed with 4wt% of methyl ethyl

Table 2.1: Determined values of gain resistors using in each amplifying circuits and their corresponding gain factors.

	Normal force	Frictional force
Rg1 (Ω)	50.889	466.832
A1	971.735	106.820
Rg2 (Ω)	465.674	466.832
A2	107.083	107.331
A_{total}	1.0406×10^5	1.1465×10^4

ketone peroxide which subsequently cured in evacuated atmosphere to avoid bubble formation. Hardened sample was abraded with 800 grit abrasive paper. Preparation methods are also used for fabricating the composite. Three experimental sets were conducted for individual conditions.

By assuming that the error produced from LT1167 is negligible or identical for both circuits, the determined coefficient should be compared. As shown by red circles in figure 2.9, the calculated coefficient is found to be load-independent at the value of about 0.4, it is considerably consistent to the reported value from low PV-limit test of about 0.55 [6]; a dissimilarity is suggested to be due to the difference in preparation technique. The results are also presented along with the values determined from a DPM-951A commercial strain amplifier (Kyowa Electronic Instruments, Japan) which also shows an adequate coherency.

For evaluating the accuracy of LT1167 op-amps, the bending strain of normal loading arm calculated from the self-constructed circuit are plotted against the values of which determined from the commercial amplifier at the identical applied forces, i.e. a relative displacement of a linear feed-through that used in a cable pulling mechanic. The plot uses the averaging values from three experimental tests. As depicted in figure 2.10, a linear relationship indicates an excellent accuracy of the circuit constructed from two operational amplifiers whereas its precision can be illustrated by the slope of fitting curve which is close to a unity. In spite of the fact that the obtained strain is found to be about 7% smaller than those of measured by the commercial available amplifier, it is considerably acceptable for quantitative measurement.

It has been experimentally proven that an self-constructed amplifying circuit with dual precision operational amplifier ICs provides a satisfactory performance in reliability, consistency

and accuracy compared to the commercial one.

2.3 Optical measuring systems

Voltage-output type H10723-20 photomultiplier tube (Hamamatsu Photonics, Japan) and a C10083-CA high-sensitivity spectrometer (Hamamatsu Photonics, Japan) are used as the optical measuring systems of the triboluminescence acquisition setup. Voltage signal from photomultiplier tube will be analyzed as the intensity-relating optical quantity while the spectrometer is employed for an observation of spectral characteristics of the emission.

2.3.1 Mathematical treatments for quantitative analysis

Due to a wave-particle duality, it is possible to consider an electromagnetic wave with a wavelength of λ as a photon packet containing the energy of $E = hc/\lambda$ where h is Planck's constant (6.626×10^{-34} J s) and c is a speed of light ($\approx 3\times10^{8}$ m s^{-1}).

Although there is only a specific spectral range of photons around 380–730 nm which is perceptible to human; it is named as visible light, the typical photodetectors are sometimes capable to detect a wider range of wavelength of radiation. Therefore, the spectral response of optical sensors are always described as 'radiant sensitivity' and 'luminous sensitivity' referring to its most sensitive wavelength and for the full-range of visible light, accordingly.

A number of incident photons per second is defined as $n = dN/dt$ at a wavelength of λ where N is the number of those photons. Radiant flux Φ_r of the given photon energy of E can be expressed as Eq. 2.8 which also named as the optical power due to a similarity of dimension,

$$\Phi_r(E) = n \cdot \frac{hc}{\lambda} = \frac{dN}{dt} \cdot E. \tag{2.8}$$

On the other hand, the luminous flux ψ, using the unit of lumens (lm), requires additional correcting factor relating to the typical sensitivity of human eyes,

$$\psi(E) = k_{\mathrm{m}} \cdot v(E) \cdot \frac{dN}{dt} \cdot E, \tag{2.9}$$

where k_m = 683.002 lm W^{-1} is a conversion coefficient from the radiant quantity to the luminous one and v(E) is the eye sensitivity as a function of wavelength of light, standardized by International Commission on Illumination (CIE) in 1931 [7].

Despite the sensitivity is originally described as a function of wavelength, in the study, it was converted into a photonic energy-dependent expression.

For a broad-spectral emitted light, a probability of observation of each wavelength $p(E)$ needs to be taken into consideration which can be depicted by a normalized TrL spectrum. Thus, the luminous flux is given as follows,

$$\psi(E) = k_m \cdot v(E) \cdot p(E) \cdot \frac{dN}{dt} \cdot E. \tag{2.10}$$

Total luminous flux is a summation of the flux within TrL emission whose spectrum are ranging from $E_1 = hc/\lambda_1$ to $E_2 = hc/\lambda_2$, .

$$\begin{aligned} \hat{\psi} = \sum_{\psi(E_1)}^{\psi(E_2)} \psi(E) &\approx \int_{E_1}^{E_2} \psi(E) dE \\ &= \int_{E_1}^{E_2} k_m \cdot v(E) \cdot p(E) \cdot \frac{dN}{dt} \cdot E dE \\ &= k_m \cdot \frac{dN}{dt} \cdot \left[\int_{E_1}^{E_2} v(E) \cdot p(E) \cdot E \, dE \right]. \end{aligned} \tag{2.11}$$

Due to the resemblance to Gaussian function of $p(E)$ and $v(E)$, a numerical calculation is required for determining of an integral value of Eq. 2.11 as an area under $p(E) \cdot v(E) \cdot E$ curve plotted against E illustrated in figure 2.11 for known emission character. The constant $\bar{E}$ is interpreted as an *effective* energy of photon.

Luminous sensitivity LS of photomultiplier tube is determined for a given controlling voltage supplied to the detector. Therefore, a measured PMT voltage V_{pmt} can be estimated by the following equation which is proportional to a flux of incoming photons.

$$V_{pmt} = LS \cdot k_m \cdot \bar{E} \cdot \frac{dN}{dt}. \tag{2.12}$$

Integration of Eq. 2.12 yields,

$$\int_{t=0}^{t=t} V_{pmt}\, dt = \int_{N=0}^{N=N} LS \cdot k_{\mathrm{m}} \cdot \bar{E} dN = LS \cdot k_{\mathrm{m}} \cdot \bar{E} \cdot N. \tag{2.13}$$

Applying the mean-value-theorem, $\frac{1}{b-a}\int_a^b f(x)dx = F_{ave}$ where F_{ave} is the mean value of $f(x)$ on the interval [a,b], an expression for estimating the number of photon emitted from deformation occurring in a period of time Δt from the average PMT voltage $\bar{V}_{pmt}$ is given by,

$$\bar{V}_{pmt} = LS \cdot k_{\mathrm{m}} \cdot \bar{E} \cdot \frac{N}{\Delta t}. \tag{2.14}$$

In conclusion, a triboluminescence measuring setup has been successfully designed and constructed which allows us for further investigating on the emission behavior of ZnS:Mn crystals due to sliding deformation. Also, it is possible to approximate the number of emitted photons from measured voltage signal of photomultiplier tube.

Reference

[1] Stachowiak, G. and Batchelor, A. *Engineering Tribology-3rd edition*. Butterworth-Heinemann, (2005).

[2] Hibbeler, R. *Statics and Mechanics of Materials - SI edition*. Prentice Hall, (2004).

[3] Gere, J. and Goodno, B. *Mechanics of Materials – Seventh edition*. Cengage Learning, (2008).

[4] C.Ishiyama and Higo, Y. *J. Polym. Sci., Part B: Polym. Phys.* **40**(5), 460–465 (2002).

[5] `http://soliton.ae.gatech.edu/people/jcraig/classes/ae3145/Lab2/strain-gages.pdf`. Online; accessed January, 2013.

[6] El-Sayed, A., El-Sherbiny, M., Abo-El-Ezz, A., and Aggag, G. *Wear* **184**(1), 45–53 (1995).

[7] International Committee on Illumination. `http://www.cie.co.at/index.php/LEFTMENUE/index.php?i_ca_id=298`. Online; accessed October, 2014.

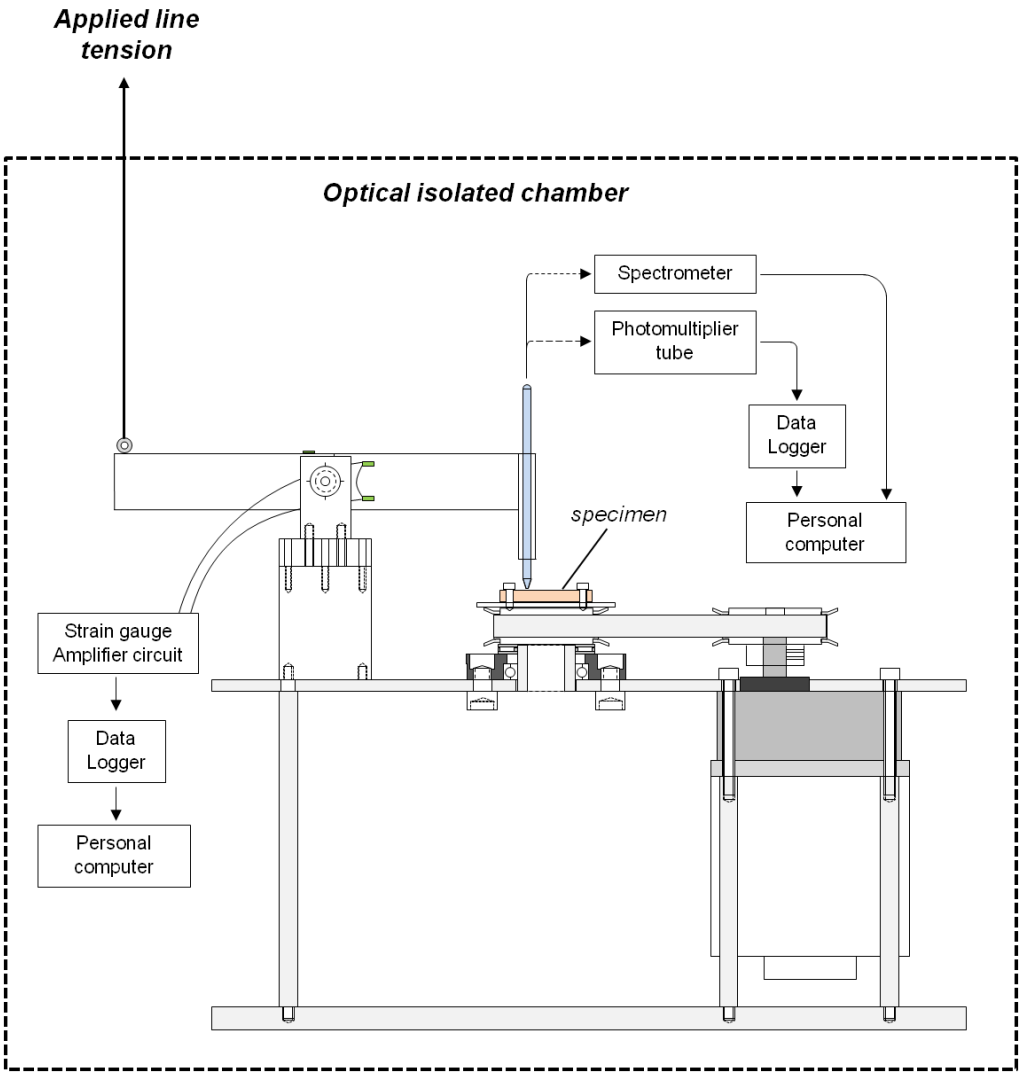

Figure 2.1: Schematic diagram of triboluminescence acquisition system.

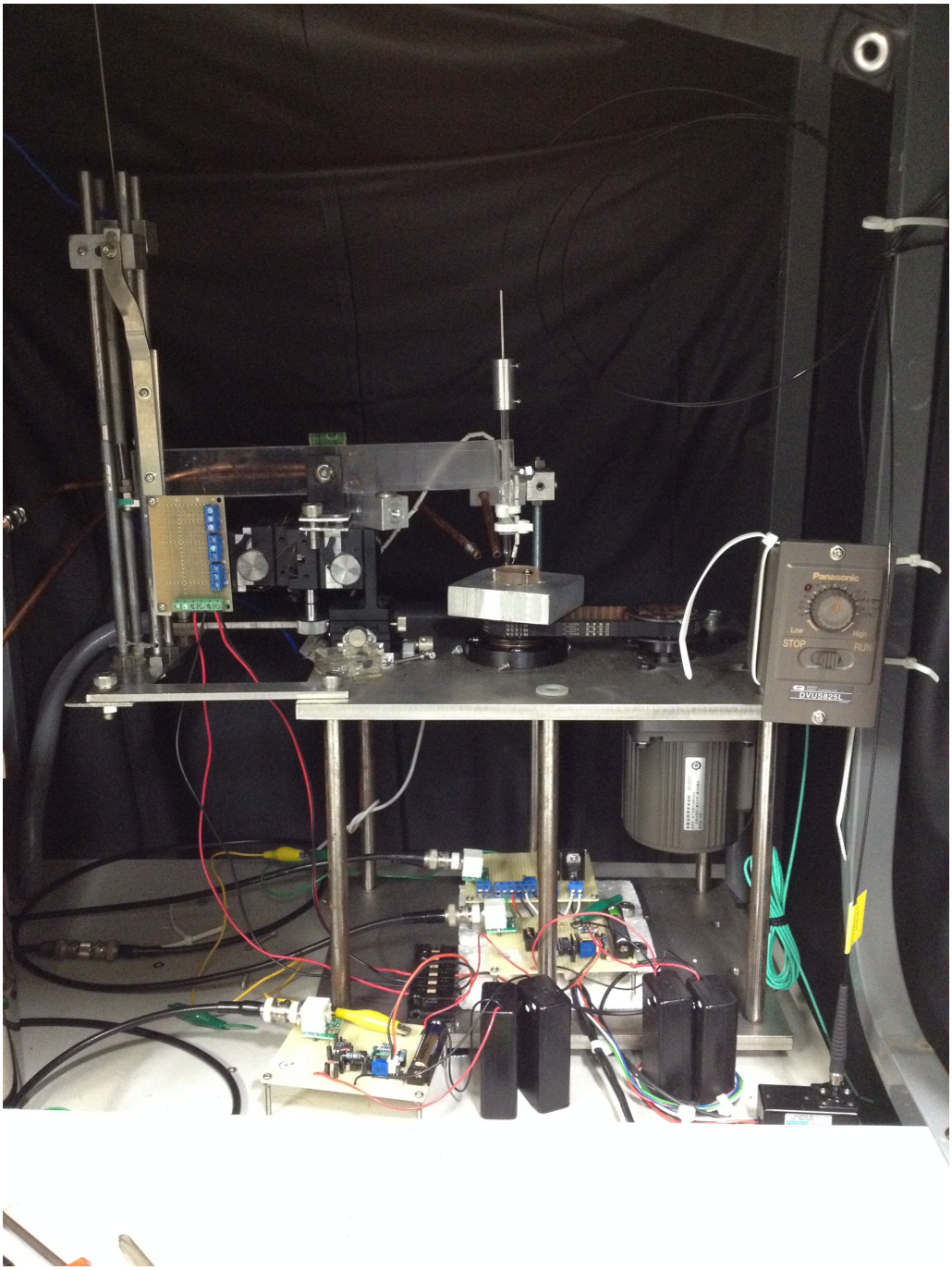

Figure 2.2: Photograph of the final version of triboluminescence acquisition system constructed and being employed throughout the study.

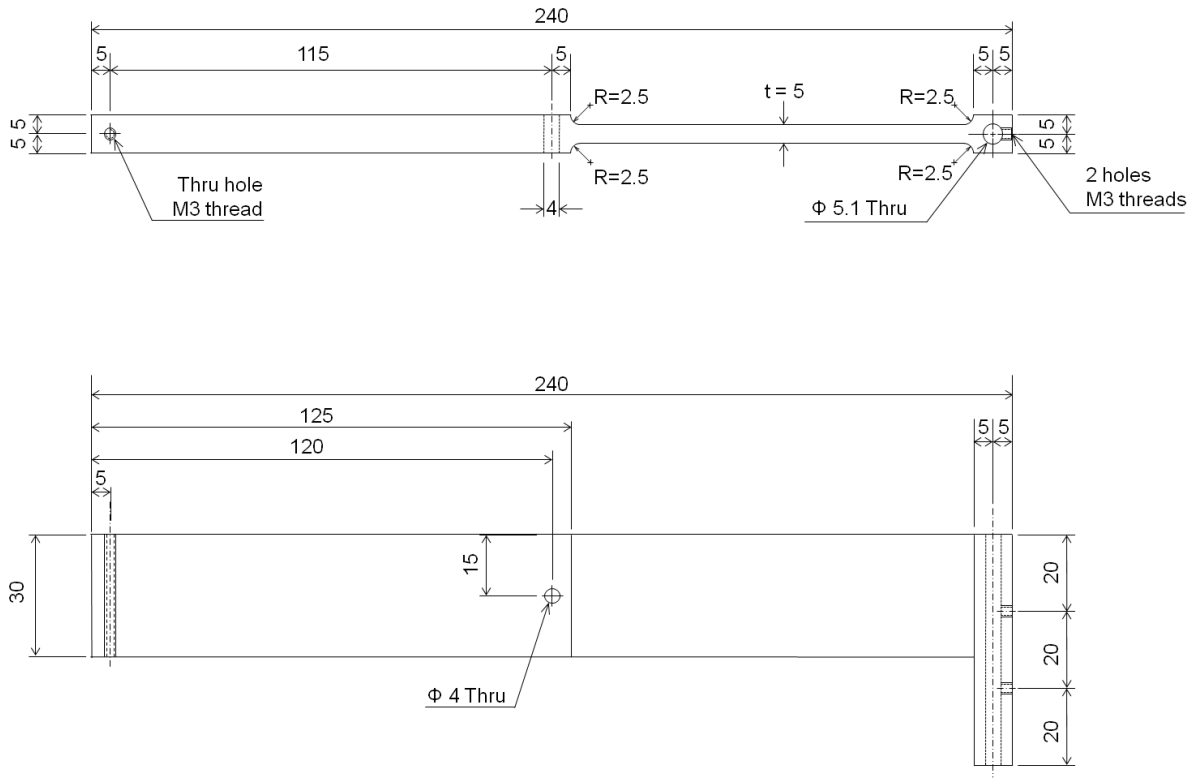

Figure 2.3: Drawing with dimensions of elastic arm using for determination of forces.

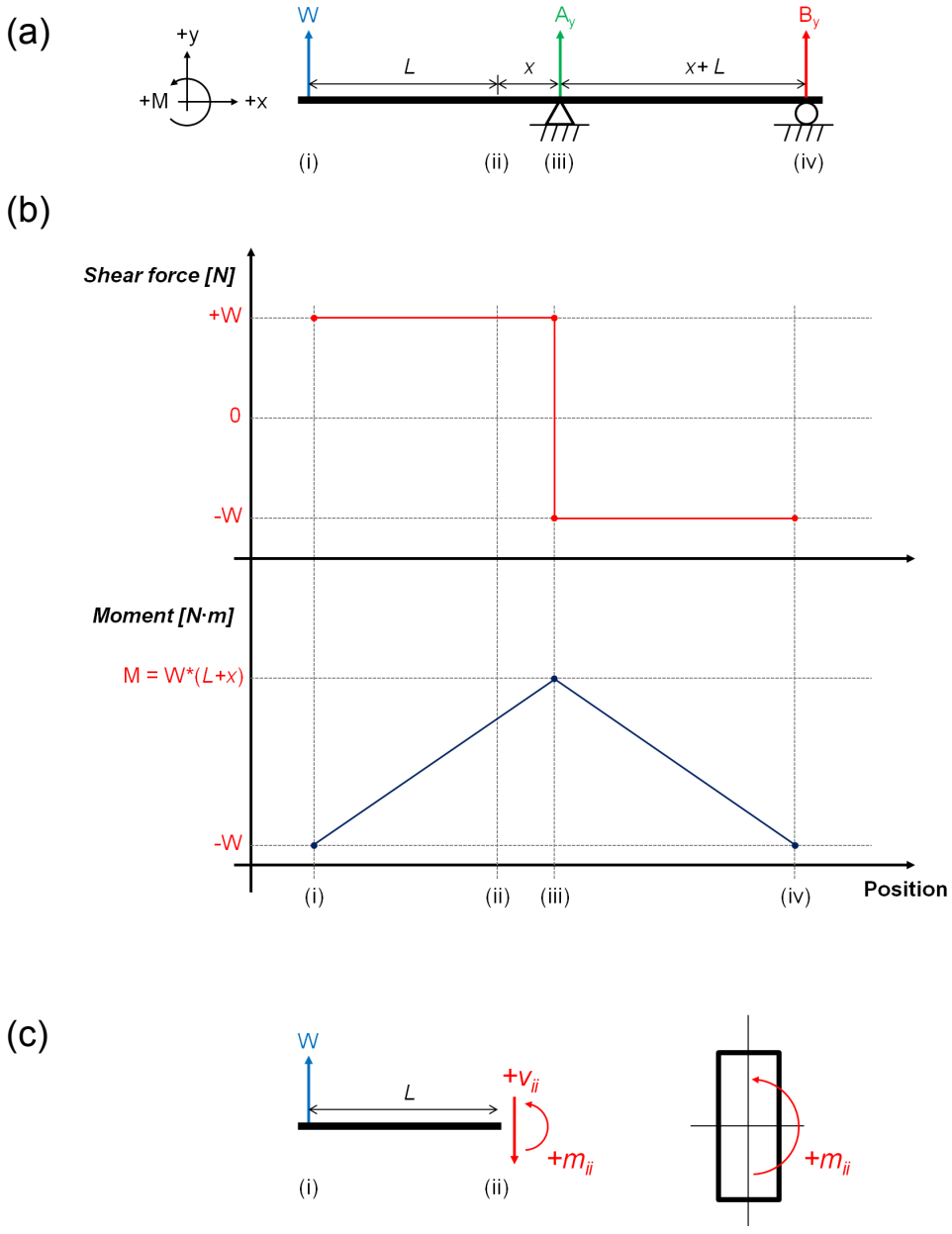

Figure 2.4: Free body diagram (a), Shear-moment diagram (b) and the internal moment along with a cross-section (c) of the beam for normal load determination. *W* represents the tensional force acting on the cable.

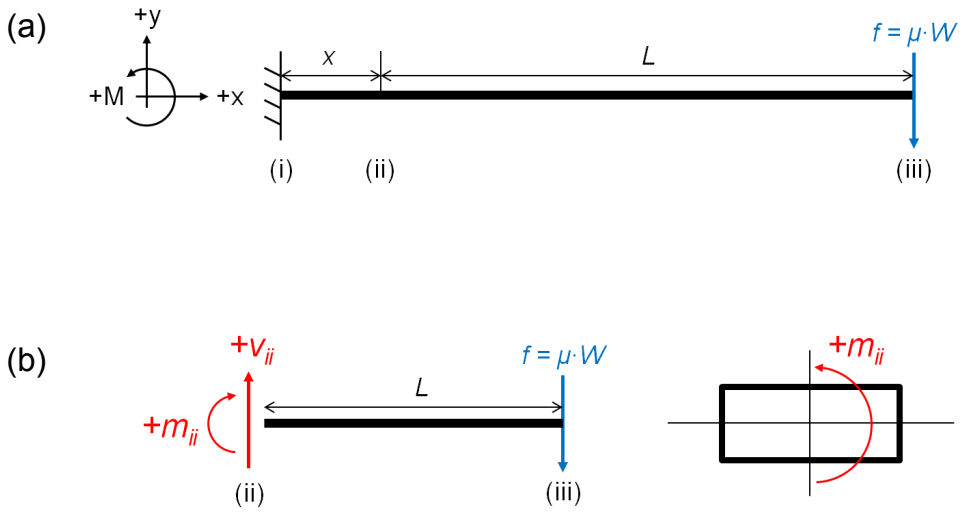

Figure 2.5: Free body diagram (a) and the internal moment along with a cross-section (b) of the beam for frictional force determination where μ is a coefficient of friction.

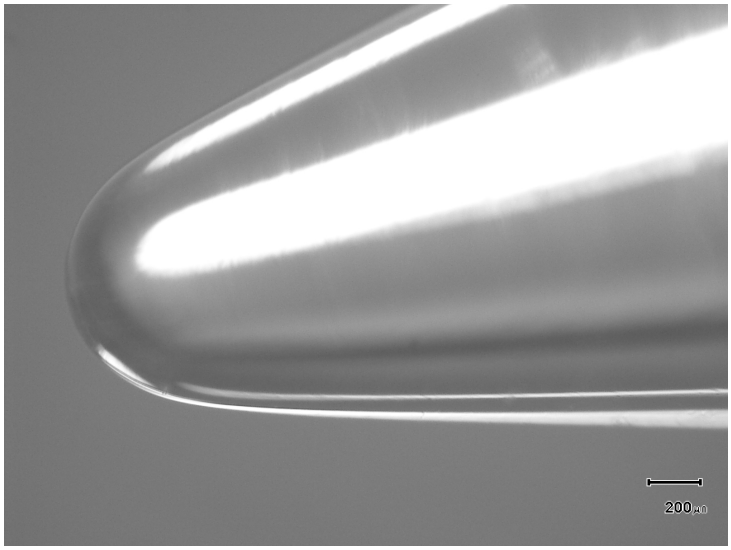

Figure 2.6: An optical image of the contacting end of the stylus using in the study which manually prepared by grinding process.

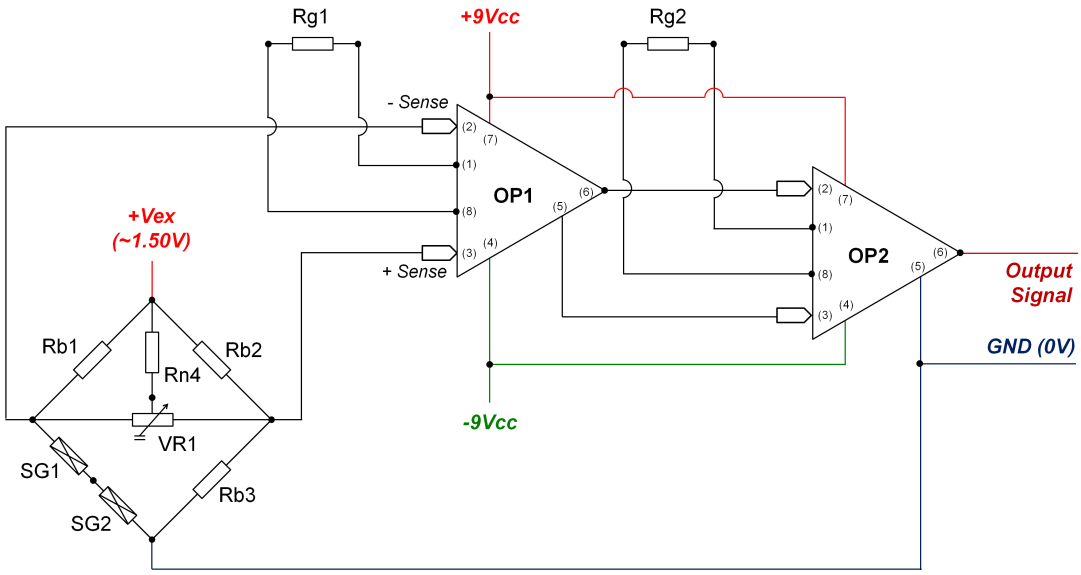

Figure 2.7: Electronic diagram of constructed amplifying circuits by high-precision instrumentation operational amplifier ICs.

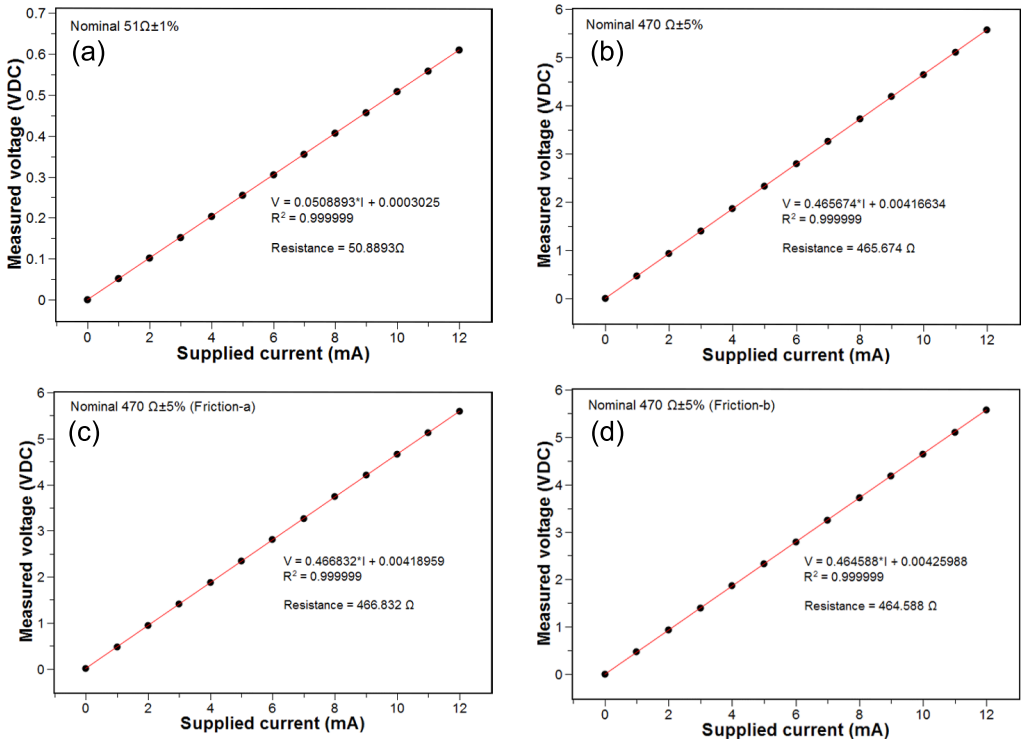

Figure 2.8: V-I plots of individual gain resistors determined by an equivalent 4-probes measurement: (a) & (b) and (c) & (d) are resistors used in the amplifying circuits for the normal and the frictional force determination, accordingly. All plots are in accordance to Ohm's law.

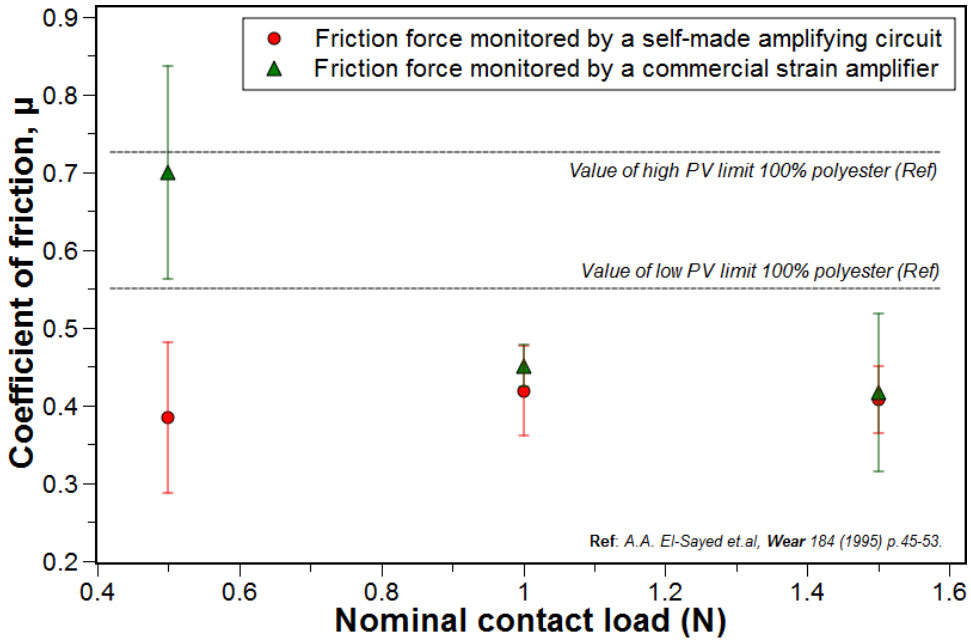

Figure 2.9: Friction coefficients of pure polyester resin. Red and green circles represent the value determined from self-constructed circuit and a commercial strain amplifier, respectively. The reported values are shown as dotted lines for comparison [6].

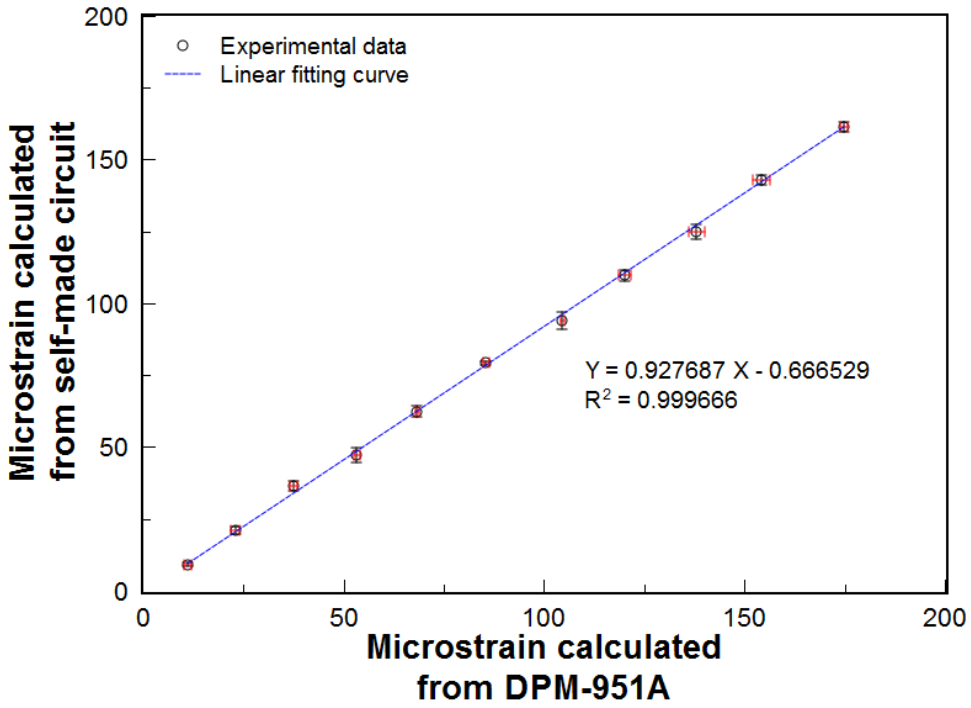

Figure 2.10: Comparison plot of the bending strain measured from the constructed amplifying circuits with respect to those of evaluated from a commercial amplifier.

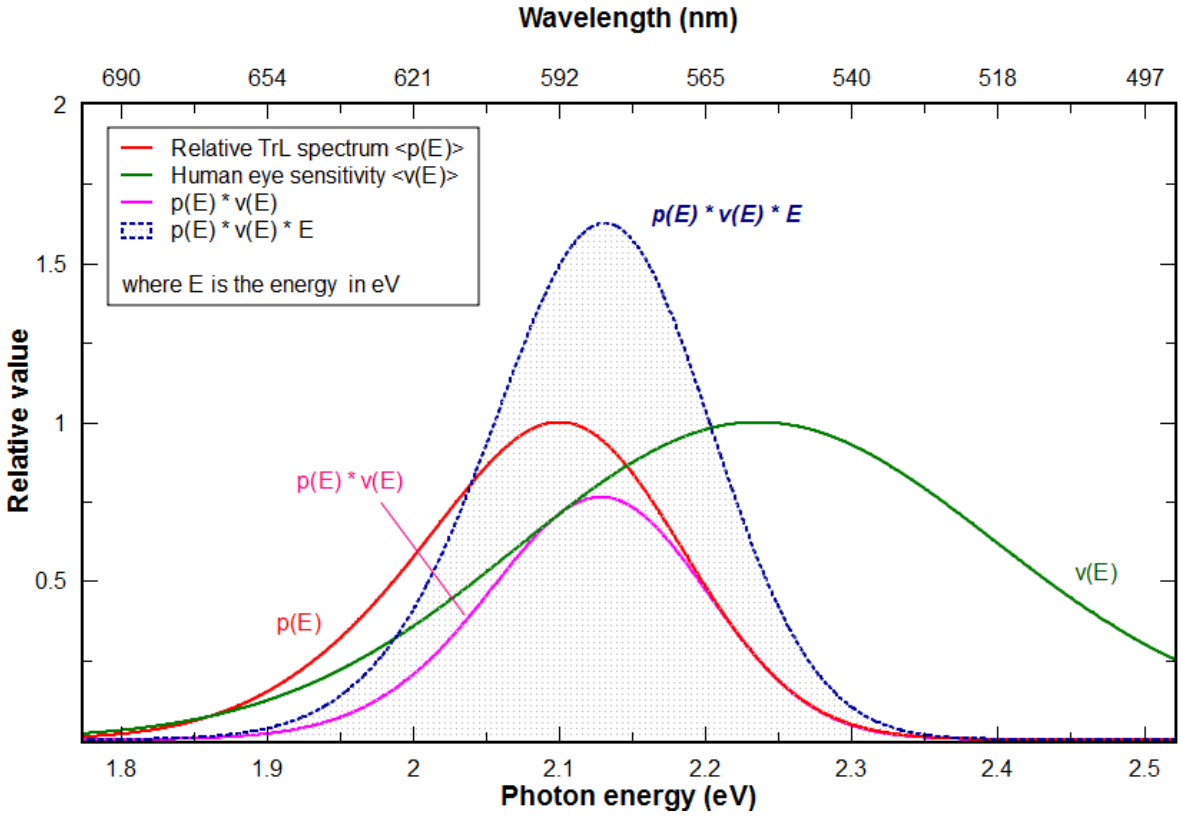

Figure 2.11: Comparison plots of the normalized TrL of ZnS:Mn, the CIE-1931 luminosity sensitivity, and the product of those functions for estimating the number of emitted photons.

Chapter 3

Estimation of mechanical behavior of phosphor-embedded composite

Due to the fact that a mechanoluminescence is rather relating to the exerted stress, for sliding contact, it is less realistic to utilize the applied force as a representative of the stress since the apparent contact area increases with higher load. Determination of contact stresses from experimental parameters will be discussed in the chapter.

3.1 Morphology and phase identification of the phosphors

Manganese-doped ZnS phosphors were provided by Kojundo Chemical Laboratory, Japan with doping concentration of 0.5 at%. Appearance and size distribution of as-received particles were observed using a JOEL JSM-7000F field-emission scanning electron microscope whereas a phase identification was performed using a Bruker AXS D8-Advance X-ray diffractometer.

According to XRD diffraction patterns, Fig. 3.1(b), a hexagonal wurtzite is a predominant structure with nearly random orientation. Crystallite size of the phosphor is about 65 nm, calculated from (002) diffraction plane using the well-known Debye-Scherrer formula. As-received powders show pebble-like appearance with an average size of 4.68 ± 1.95 μm shown in Fig. 3.1(a). Stacking fault is responsible for strip lines on the surface of particle. A presence of the hexagonal at room temperature contradicts an equilibrium phase diagram of ZnS-MnS [1]; it might be due to rapid cooling after heat treatment required for producing luminescent doped ZnS [2, 3].

3.2 Sub-surface stress fields under a sliding contact

3.2.1 Hertzian elastic contact theory and contact area determination [4]

According to the observations of interference fringes of two glass lenses by *Heinrich Hertz*, a shape of contact region is generally ellipse. Besides of a uniform distribution of force over contact region, he suggested that an applied pressure p is rather expressed as a function of the x-y coordination which being maximized at the center of the area,

$$p = p_0 \left\{ 1 - (x/a)^2 - (y/b)^2 \right\}^{1/2}. \tag{3.1}$$

For a circular contact patch, having $a = b$, the pressure distribution can be given in a spherical coordinate where r is a radius of the circle,

$$p = p_0 \left\{ 1 - (r/a)^2 \right\}^{1/2}. \tag{3.2}$$

For the bodies whose radius of curvature R_1 and R_2, the relative curvature R' can be given as,

$$\frac{1}{R'} = \frac{1}{R_1} + \frac{1}{R_2}. \tag{3.3}$$

Giving the elastic moduli of each component as E_1 and E_2, it allows us to describe the effective young modulus as the following equation since the exerting stress on both bodies are identical,

$$\frac{1}{E'} = \frac{1-\nu_1^2}{E_1} + \frac{1-\nu_2^2}{E_2}. \tag{3.4}$$

Thus, for the compressive loading force W, a radius of contact circle a can be written as,

$$a = \left(\frac{3WR'}{4E'} \right)^{1/3}. \tag{3.5}$$

For a static contact between a sphere and a plane, illustrated in figure 3.2, a circular contact is created whose diameter $2a$ is governed by a magnitude of applied force and the mechanical and geometrical parameters of two bodies [4–7]. Suffices p, s refer to the sliding pin and the

sample, respectively, where d is a tip diameter, E is elastic modulus, ν is Poisson ratio and W is an applied load,

$$a = \left[\frac{3}{8}\, d_p \left(\frac{1-\nu_p^2}{E_p} + \frac{1-\nu_s^2}{E_s}\right)\right]^{1/3} \sqrt[3]{W}$$
$$= k_a \sqrt[3]{W}. \tag{3.6}$$

Since the pin is made of soda-lime glass, the value of E_p and ν_p is reported as 70.0 GPa and 0.23, accordingly [8]. On the other hand, the physical parameters of composite materials are controlled by volume fraction of reinforcements.

3.2.2 Determination of mechanical properties of the composite

Poisson ratio

It can be approximated from a simple mixture rule as the difference in Poisson ratio of common engineering materials are considerably small where v_f refers to a volume fraction of ZnS phosphors.

$$\nu_c = v_f \nu_Z + \left(1 - v_f\right) \nu_M. \tag{3.7}$$

Young modulus

(A) Boundaries of the moduli of the composite [9] Let us consider a continuous unidirectional fibrous composite. For the case that a deformation direction is parallel to an alignment of the reinforcement, the total load is shared on each phases and consequently yields Eq. 3.8 which is in turns analogous to a rule of mixture; the relationship is also known as *Voigt model* whereas the so-called *Reuss Model* describes the behavior of transverse loading scenario (Eq. 3.9). It is worth mentioning that the calculated vale from both models is approximately identical when

the modulus of the matrix is close to that of reinforcement.

$$E_c = E_Z(v_Z) + E_M(1 - v_Z) \tag{3.8}$$

$$\frac{1}{E_c} = \frac{v_Z}{E_Z} + \frac{1 - v_Z}{E_M}. \tag{3.9}$$

Although those expressions are usually regarded as an upper- and lower-boundary of the modulus of the composite, respectively, the calculated values are not satisfactory for the prediction on particle-embedded composites.

(B) Infinitely diluted particulate composite [10] The elastic moduli of an *infinitely dilute* concentration of spheroidal particles in the composite are given as,

$$\frac{G_c}{G_M} = 1 + \left[\frac{15(1-\nu_M)(G_Z - G_M)}{2G_Z(4-5\nu_M) + G_M(7-5\nu_M)}\right] v_f \tag{3.10}$$

$$\frac{K_c}{K_M} = 1 + \left[\left(\frac{3K_M + 4G_M}{3K_M}\right)\left(\frac{3K_Z - 3K_M}{3K_Z + 4G_M}\right)\right] v_f \tag{3.11}$$

where G is shear modulus, K is bulk modulus and ν is Poisson ratio while subscripts c, M and Z refer to the composite, the matrix and the particles accordingly. Volume fraction denotes as v_f.

Taking into account the isotropy of particulate composite, an elastic modulus E can be expressed as,

$$E_c = \frac{9K_cG_c}{3K_C + G_c}. \tag{3.12}$$

Inserting Eq. 3.10 into Eq. 3.12 yields,

$$\frac{E_c}{E_M} = 1 + [10\beta_1(1+\nu_M) + \beta_2(1 - s\nu_M)]\, v_f \tag{3.13}$$

where β_1 and β_2 are given as:

$$\beta_1 = \left[\frac{\alpha_1(E_Z/E_M) - \alpha_2}{2\alpha_3(E_Z/E_M) + \alpha_4}\right] \tag{3.14}$$

$$\beta_2 = \left[\frac{\alpha_2[(E_Z/E_M) - \alpha_5]}{(E_Z/E_M) + 2\alpha_6}\right]. \tag{3.15}$$

In above equations, α's are functions of Poisson ratio of the components which are described as follow;

$$\alpha_1 = \frac{1-\nu_M}{1+\nu_Z} \tag{3.16}$$

$$\alpha_2 = \frac{1-\nu_M}{1+\nu_M} \tag{3.17}$$

$$\alpha_3 = \frac{4-5\nu_M}{1+\nu_Z} \tag{3.18}$$

$$\alpha_4 = \frac{7-5\nu_M}{1+\nu_M} \tag{3.19}$$

$$\alpha_5 = \frac{1-2\nu_Z}{1-2\nu_M} \tag{3.20}$$

$$\alpha_6 = \frac{1-2\nu_Z}{1+\nu_M}. \tag{3.21}$$

If the matrix phase is incompressible, that is $\nu_M = 0.5$, Eq. 3.13 can be simplified as Eq. 3.22 which is only valid for low volumetric content.

$$\frac{E_c}{E_M} = 1 + \left\{ \left[\frac{15\,(E_Z/E_M) - 10\,(1+\nu_Z)}{6\,(E_Z/E_M) + 6\,(1+\nu_Z)} \right] - \left[\frac{(1-2\nu_Z)}{3\,(E_Z/E_M) + 4\,(1-2\nu_Z)} \right] \right\} v_f. \tag{3.22}$$

Differentiation of the equation with respect to the volume fraction yields,

$$\mathrm{d}E_c = E_c \left[\frac{15E_Z - 10E_c\,(1+\nu_Z)}{6E_Z + 6E_c\,(1+\nu_Z)} - \frac{(1-2\nu_Z)\,E_c}{3E_Z + 4E_c\,(1-2\nu_Z)} \right] \mathrm{d}v_f. \tag{3.23}$$

Integration of the increment of reinforcement phases with the limit of $E_c \to E_M$ at $v_F \to 0$ produces,

$$\left(\frac{E_c}{E_Z}\right) \left[\frac{ME_M - 3E_Z(P+Q)}{ME_c - 3E_Z(P+Q)} \right]^{(N+53)/46} \left[\frac{ME_c - 3E_Z(P-Q)}{ME_M - 3E_Z(P-Q)} \right]^{(N-53)/46} = \exp(2.5v_f). \tag{3.24}$$

where

$$M = 46\,(1+\nu_Z)\,(1-\nu_Z) \tag{3.25}$$

$$P = 4 - 23\nu_Z \tag{3.26}$$

$$Q = \sqrt{3\left(23\nu_Z^2 - 138\nu_Z + 82\right)} \tag{3.27}$$

$$N = \frac{833 - 736\nu_Z}{46Q}. \tag{3.28}$$

In fact, an increment of actual volume fraction of dispersed particles should be described as $\mathrm{d}v_f/(1-v_f)$. Upon the integration with similar limit as the previous, one can write a relationship of an effective modulus of the particulate composite to the volume fraction,

$$\left(\frac{E_c}{E_Z}\right)\left[\frac{ME_M - 3E_Z(P+Q)}{ME_c - 3E_Z(P+Q)}\right]^{(N+53)/46}\left[\frac{ME_c - 3E_Z(P-Q)}{ME_M - 3E_Z(P-Q)}\right]^{(N-53)/46} = \left(1-v_f\right)^{-2.5}. \tag{3.29}$$

Although the models are in excellent agreement to other reported experimental results, it is substantially difficult to be used in practice as a numerical approach is required.

(C) Brick-wall model [11] *W.F. Hosford* has proposed an alternative less-complex model as a superimposition of the uniaxial stressed continuous fibrous composite composing a network frame of matrix with thickness t reinforcing by columns of alternating layers of hard-phase cubes at length of $1-t$ and matrix phase. Geometrical illustration of the model is shown in figure 3.3. In fact, this expression has not taken into account the influence of packing efficiency and distribution of particle sizes. Alphabetical suffix Z and M denotes reinforcement (ZnS) and matrix (polyester resin) accordingly while the direction corresponds to numeric suffices.

One can express a volume fraction v_f of particles as a function of matrix thickness as,

$$v_f = (1-t)^3. \tag{3.30}$$

Considering that the load is applied in 1-direction, the effective modulus of stack-like

columns is identical to the Ruess model,

$$\frac{1}{E'} = \frac{1-t}{E_Z} + \frac{t}{E_M}. \tag{3.31}$$

Hookes's law yields,

$$\varepsilon_{1M} = \frac{1}{E_M}\left[\sigma_{1M} - \nu_M\left(\sigma_{2M} + \sigma_{3M}\right)\right], \tag{3.32}$$

$$\varepsilon_{2M} = \frac{1}{E_M}\left[\sigma_{2M} - \nu_M\left(\sigma_{1M} + \sigma_{3M}\right)\right], \tag{3.33}$$

$$\varepsilon_{3M} = \frac{1}{E_M}\left[\sigma_{3M} - \nu_M\left(\sigma_{1M} + \sigma_{2M}\right)\right]. \tag{3.34}$$

which can be also implemented on the reinforcement phase.

Due to the symmetry, the stress acting in 2-direction is required to equal to that of 3-direction, i.e. $\sigma_{3M} = \sigma_{2M}$ and $\sigma_{3Z} = \sigma_{2Z}$ while the 1-direction stress equals in both phases, that is $\sigma_1 = \sigma_{1Z} = \sigma_{1M}$,

$$\begin{aligned}\varepsilon_{2Z} &= \frac{1}{E_Z}\left[\left(1-\nu_Z\right)\sigma_{2Z} - \nu_Z\sigma_1\right] \\ \varepsilon_{2M} &= \frac{1}{E_M}\left[\left(1-\nu_Z\right)\sigma_{2M} - \nu_M\sigma_1\right]\end{aligned} \tag{3.35}$$

For more realistic approximation, a condition of $\varepsilon_{2Z} = \varepsilon_{2M}$ is assumed as well as the force balance in 2-direction in which yields $\sigma_{2M} = -\frac{t}{(1-t)}\sigma_{2Z}$,

$$\begin{aligned}\sigma_{2B}\left[\left\{\frac{1-\nu_M}{E_M}\right\} + \left\{\left(\frac{t}{1-t}\right)\left(\frac{1-\nu_Z}{E_Z}\right)\right\}\right] &= \left(\frac{\nu_M}{E_M} - \frac{\nu_Z}{E_Z}\right)\sigma_1 \\ \frac{\sigma_{2M}}{\sigma_1} &= \left[\frac{\nu_M}{E_M} - \frac{\nu_Z}{E_Z}\right] / \left[\left(\frac{1-\nu_M}{E_M}\right) + \left(\frac{t}{1-t}\right)\left(\frac{1-\nu_Z}{E_Z}\right)\right]\end{aligned} \tag{3.36}$$

Inserting Eq. 3.36 into Eq. 3.32, it yields,

$$\frac{\varepsilon_{1M}}{\sigma_1} = \left(\frac{1}{E_M}\right)\left[1 - 2\nu_M\left(\frac{\sigma_{2M}}{\sigma_1}\right)\right] \tag{3.37a}$$

$$\frac{\varepsilon_{1Z}}{\sigma_1} = \left(\frac{1}{E_Z}\right)\left[1 - 2\nu_M\left(\frac{\sigma_{2M}}{\sigma_1}\right)\left(\frac{t}{1-t}\right)\right]. \tag{3.37b}$$

Equation 3.37a and Eq. 3.37b are not only the representative of constrained young moduli of each component in the reinforcement columns but also being able to estimate the stress exerting on individual component.

Substituting above expressions into Eq. 3.31,

$$E' = 1/\left[t\frac{\varepsilon_{1M}}{\sigma_1} + (1-t)\frac{\varepsilon_{1Z}}{\sigma_1}\right]. \tag{3.38}$$

Cross-sectional area of the columnar reinforcements equals to $(1-t)^2$ while $1-(1-t)^2 = t(2-t)$ is for matrix structure. Therefore, it is possible to calculate the total modulus of such composite by the Reuss model,

$$E_c = (1-t)^2 E' + t(2-t)E_M. \tag{3.39}$$

Comparison of the mentioned models Figure 3.4 illustrates a comparison plot of the predicted effective Young moduli by various models. Physical constants of phosphors are listed in table 1.1 whereas the elastic modulus and Poisson ratio of the resin is 4.0 GPa and 0.4, respectively [12]. It can be seen that both the modified diluted model and the brick-wall model are an intermediate value within the boundaries up to moderate concentration. At a volume fraction of 22.28%, one of volumetric contents using in the experiments, a brick-wall model predicts the young modulus of the composite about 27% higher than that of obtained from Eq. 3.29.

According to the results, a prediction from the brick-wall model is likely to be acceptable with an expense of calculation procedures so that the approach is adopted for determining the modulus of the particulate composite in this study.

Substituting Eq. 3.39 and Eq. 3.7 into E_s and ν_s of Eq. 5.2, the contact radius at different phosphor composition can be determined. It is obvious that the radius will be increased with

lower effective young modulus which consistent to the stiffness of the composite.

Table 3.1: Calculated mechanical parameters of the composite with different compositions using in this study.

	$v_f = 5.57\%$	$v_f = 22.28\%$
E_c (GPa)	5.063	8.802
ν_c	0.401	0.403
K_a (m $N^{-1/3}$)	36.105	30.556

3.2.3 Stress distribution under contact surface

Sub-surface stress fields are the analytical solutions of a semi-infinite plane problem whose boundary stresses, within a contact circle of diameter $2a$, are given by Eq. 3.40 where μ is a macroscopic coefficient of friction and W is an applied load [4, 6],

$$\sigma_{zz} = -\frac{3W}{2\pi a^3}(a^2 - x^2 - y^2)^{1/2}, \tag{3.40}$$

$$\tau_{zx} = -\frac{3\mu W}{2\pi a^3}(a^2 - x^2 - y^2)^{1/2}. \tag{3.41}$$

The former condition is a contribution of the normal load whereas the tangential force produces the latter surface boundary. It can be seen that the normal contact pressure is maximum at the center of the circle which generally denoted as $P_{max} = \frac{3W}{2\pi a^2}$. Consequently, the maximum tangential surface shear stress is $Q_{max} = \mu P_{max}$

Full description of the explicit equations for three-dimensional stress fields developed under a circular contact with a presence of frictional force can be found elsewhere [6]. On the loading axis, the stress functions are reduced into following equations [6] where ν is a Poisson ratio, $\zeta = z/a$ is a dimensionless depth and superscripts N and T namely refer to a contribution of normal load and tangential force.

$$
\begin{aligned}
\sigma_{xx}^{N} &= \sigma_{yy}^{N} \\
&= P_{max}\left[(1+\nu)\left(\zeta\tan^{-1}(1/\zeta)-1\right)+\frac{1}{2(1+\zeta^2)}\right], \\
\sigma_{zz}^{N} &= P_{max}\left[-\frac{1}{1+\zeta^2}\right], \\
\tau_{xz}^{T} &= \mu P_{max}\left[-1+\frac{3}{2}\left(\zeta\tan^{-1}(1/\zeta)-1\right)-\frac{\zeta^2}{2(1+\zeta^2)}\right].
\end{aligned}
\tag{3.42}
$$

It is more convenient to express the resultant stress functions as a scalar equivalent stress defining as $\sigma_{eqv} = \sqrt{3J_2}$ where J_2 is the second deviatoric stress invariant. This term is also known as von Mises stress in which corresponds to an equivalent uniaxial stress scenario.

$$
J_2 = \frac{1}{6}\left\{(\sigma_{xx}-\sigma_{yy})^2+(\sigma_{xx}-\sigma_{zz})^2+(\sigma_{yy}-\sigma_{zz})^2\right\}+\tau_{xy}^2+\tau_{yz}^2+\tau_{zx}^2. \tag{3.43}
$$

Using symbolical computation, a more compact expression of equivalent stress along the loading axis is given by Eq. 3.44. The first term on the right hand side is depicted as a blue line in figure 3.5 whereas a red curve illustrates a contribution of frictional force. It is noteworthy mentioning that the stress at just beneath surface should be obtained from an extremely small value of ζ since $\tan^{-1}(1/0)$ is undefined. In addition to normal loads, such stress also increases as a consequence of frictional force.

$$
\left(\frac{\sigma_{eqv}}{P_{max}}\right)^2 = \frac{1}{4}\left(2(1+\nu)(\zeta\ \tan^{-1}(1/\zeta)-1)+\frac{3}{\zeta^2+1}\right)^2+\frac{3}{4}\left(3\ \zeta\tan^{-1}(1/\zeta)-\frac{\zeta^2}{\zeta^2+1}-2\right)^2\mu^2 \tag{3.44}
$$

$$
= \bar{A}_0^2. \tag{3.45}
$$

Coordinate-independent sub-surface stress under a hemispherical domain of $r \leq a$ can be approximated by an average value of σ_{eqv}/P_{max} within considering range. In other words, a uniform equivalent stress exerting beneath an interface is assumed. Hence, a total deformation volume for one cycle of rotation approximately equals to a half volume of torus (doughnut-like ring) whose major and minor radii R and r corresponds to the radii of the wear track and that of

contact region respectively. Volume of such geometric shape is given as $\frac{1}{2}(2\pi^2 Rr^2) = \pi^2 Rr^2$.

By introducing frictional force to the contact, a maximum shear stress, that is $\sqrt{J_2}$, increases as its position shifts toward to the interface and tangential force direction as shown in Fig. 3.6 [6, 7]. This therefore results in a distortion of stress contours. Nonetheless, a symmetrical stress distribution is still comparatively assumable for a small confined domain with moderate friction coefficient.

3.2.4 Prediction on the relationship of TrL intensity, applied force and contact stress

An equivalent stress is proportional to the maximum Hertzian contact pressure so that it is able to express as a function of applied force W and contact radius a. Substitution of Eq. 5.2 into such expression yields,

$$\sigma_{eqv} = k_1 W^{1/3} \tag{3.46}$$

Similarly, it is possible to describe the deformation domain of one sliding cycle as,

$$\Omega = k_2\, \pi^2\, R\, W^{2/3}. \tag{3.47}$$

Applying Eq. 3.46 and Eq. 3.47 in Eq. 6.28, one can obtain,

$$\bar{V}_{pmt} = k_3\, W^{2/3} \left[\left(\exp(k_4\, W^{2/3}) \right) - 1 \right] \tag{3.48}$$

$$\approx k_5\, W^{4/3}. \tag{3.49}$$

The resulting correlation suggests that the emission intensity may increase with applied normal load in approximately linear relationship.

3.3 Summaries

By utilizing a modified Hertzian contact theorem, it is possible to evaluate a magnitude of exerting stress as von Mises uniaxial stress caused by sliding deformation when all relevant

parameters are given. This approach results in more appropriate variable in which can be used for investigating a correlation between triboluminescent intensity and mechanical deformation.

Flowchart for evaluating a sliding contact stress of the particulate composite

1. Determination of mechanical properties of the composite
    - Employing Eq. 3.7 to calculate an effective Poisson ratio.
    - Using Eq. 3.39 to evaluate an effective young modulus.
2. Evaluating the contact radius by Eq. 5.2.
3. Obtaining the friction coefficient from experiments.
4. Calculating $\bar{A}_0$ in range of $0 < \zeta \leq 1$ from Eq. 3.44.
5. Finding P_{max} for each loading condition using the calculated radius.
6. Multiplying $\bar{A}_0$ to P_{max} to convert normal load to the equivalent stress.

Reference

[1] Sombuthawee, C., Bonsall, S., and Hummel, F. *J. Solid State Chem.* **25**, 391–399 (1978).

[2] *Thin Solid Films* **352**(1-2), 273–277 (1999).

[3] Agyeman, O., Xu, C., Suzuki, M., and Zheng, X. *J. Mater. Res.* **17**(5), 959–963 (2002).

[4] Johnson, K. *Contact Mechanics*. Cambridge University Press, (1985).

[5] Stachowiak, G. and Batchelor, A. *Engineering Tribology-3rd edition*. Butterworth-Heinemann, (2005).

[6] Hamilton, G. *Proc. Instn. Mech. Engrs.* **197**, 53–59 (1983).

[7] Hamilton, G. and Goodman, L. *J. Appl. Mech.-T ASME* **33**(2), 371–376 (1966).

[8] Oliver, W. and Pharr, G. *J. Mater. Res.* **7**, 1564–1583 (1992).

[9] Callister, W. *Materials Science and Engineering - an introduction – Sixth edition*. John Wiley & Sons, Inc., (2003).

[10] Pal, R. *Composites Part B* **36**(6-7), 513–523 (2005).

[11] Hosford, W. *Metall. Mater. Trans. A* **35**(7), 2191–2192 (2004).

[12] Aly, M., Goda, I., and Hassan, G. *IJMME-IJENS* **10**(3), 59–68 (2010).

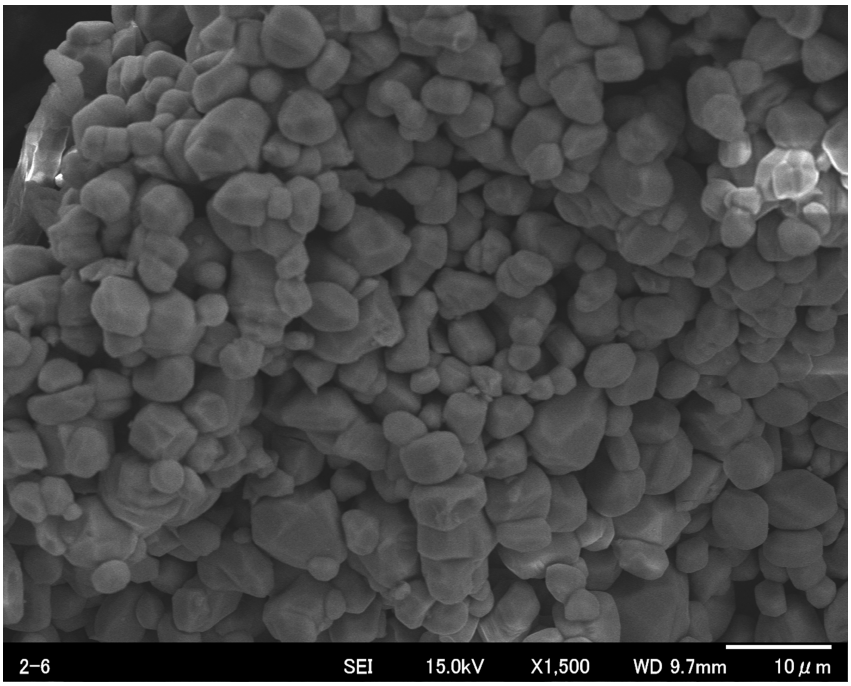

(a)

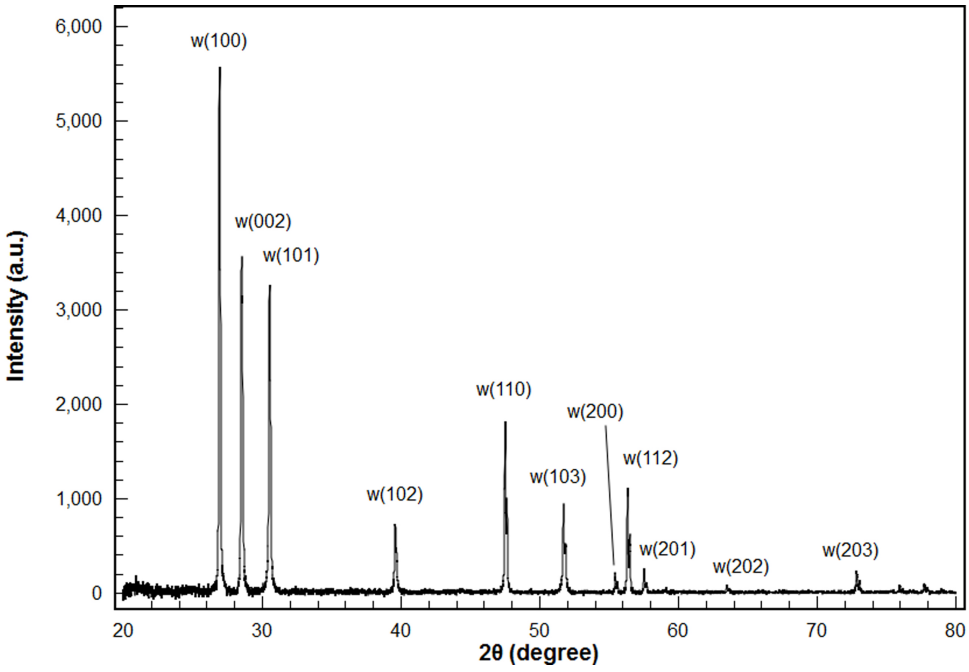

(b)

Figure 3.1: (a) SEM image and (b) XRD diffraction patterns of ZnS:Mn particles. The cubic and hexagonal phase is assigned as zb and w respectively.

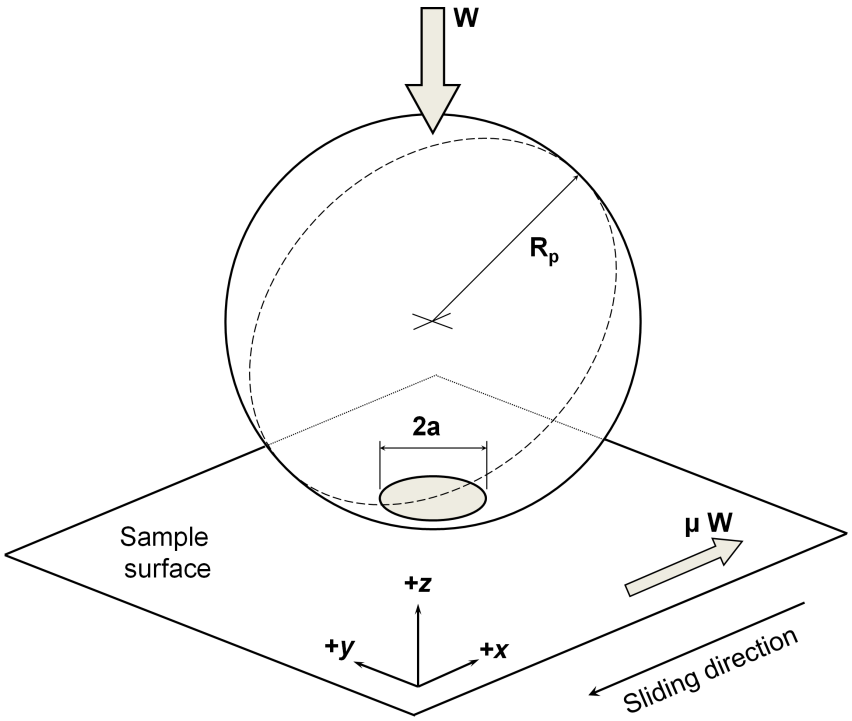

Figure 3.2: A geometrical illustration and coordinates of a sphere-plane sliding contact problem.

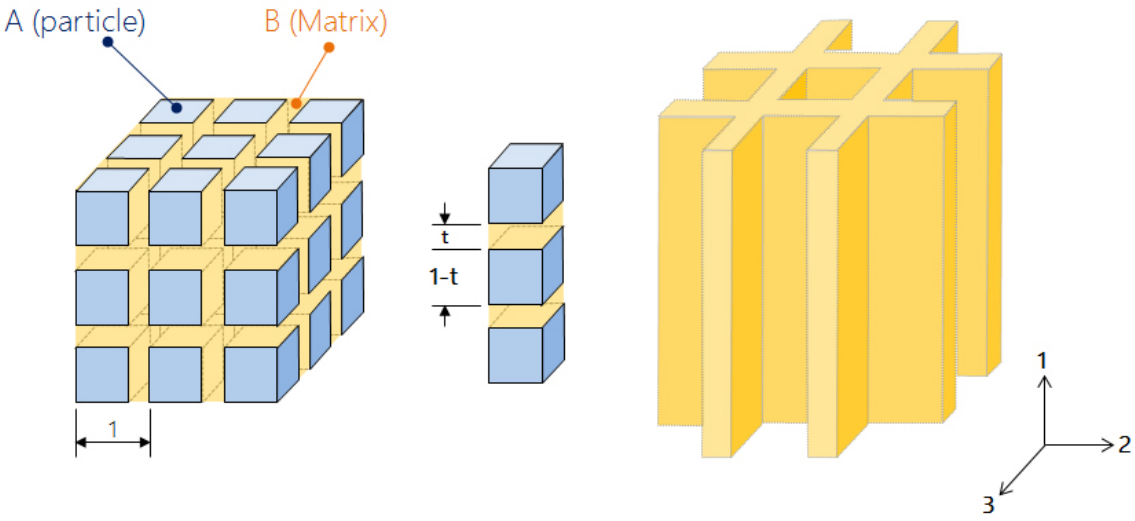

Figure 3.3: Schematic illustration of the Brick-wall model proposed by *W. F. Hosford*. Hard particles A in the shape of cubes are separated by a soft matrix B of thickness of t.

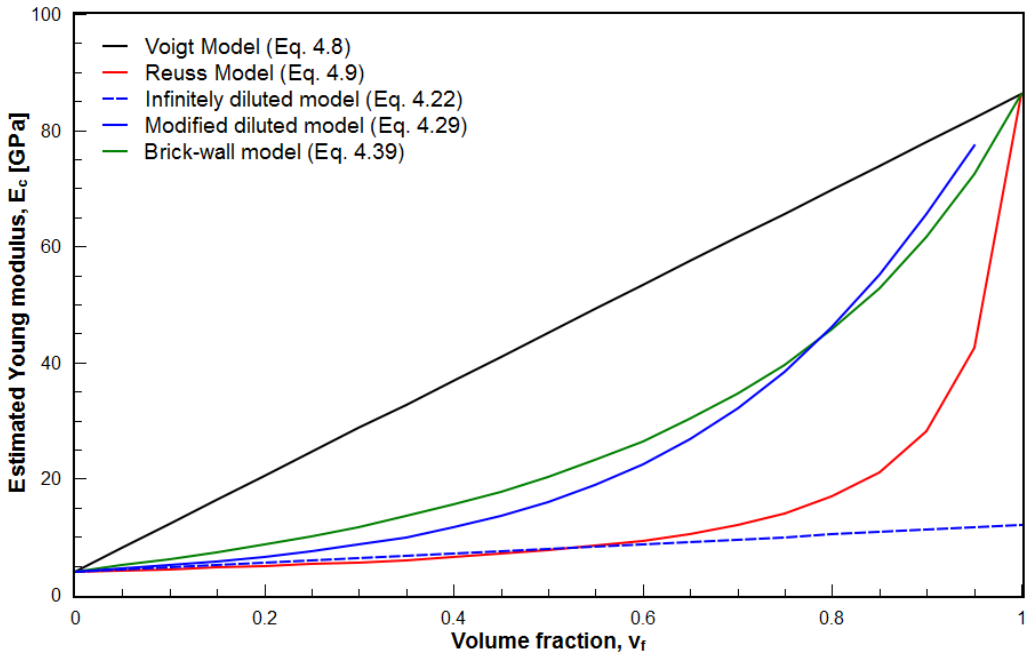

Figure 3.4: Composite Young Moduli determined by various models.

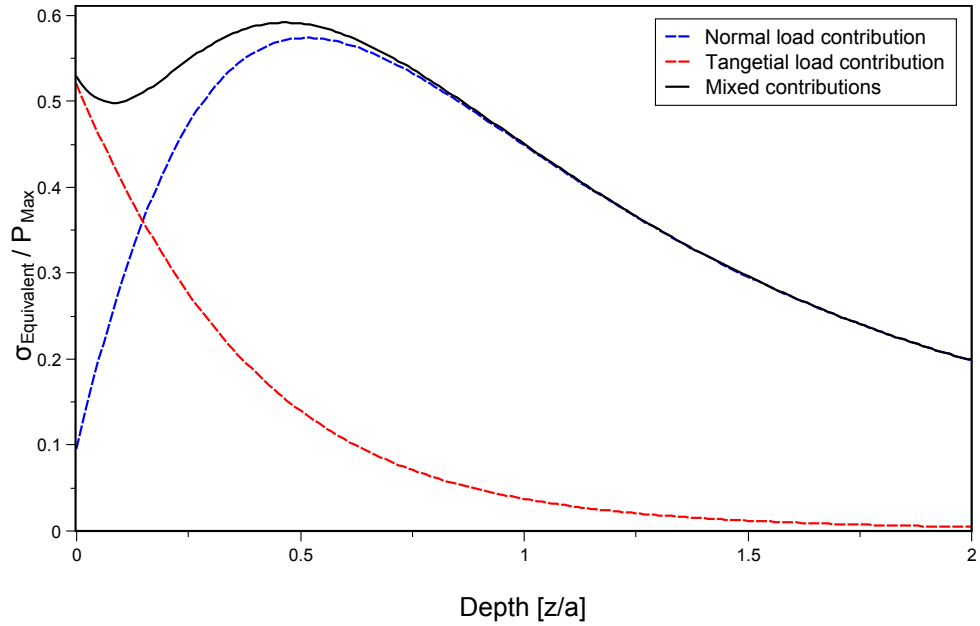

Figure 3.5: Comparison plots of an equivalent stress contributed by the normal load, the tangential force and the combination of both applied forces.

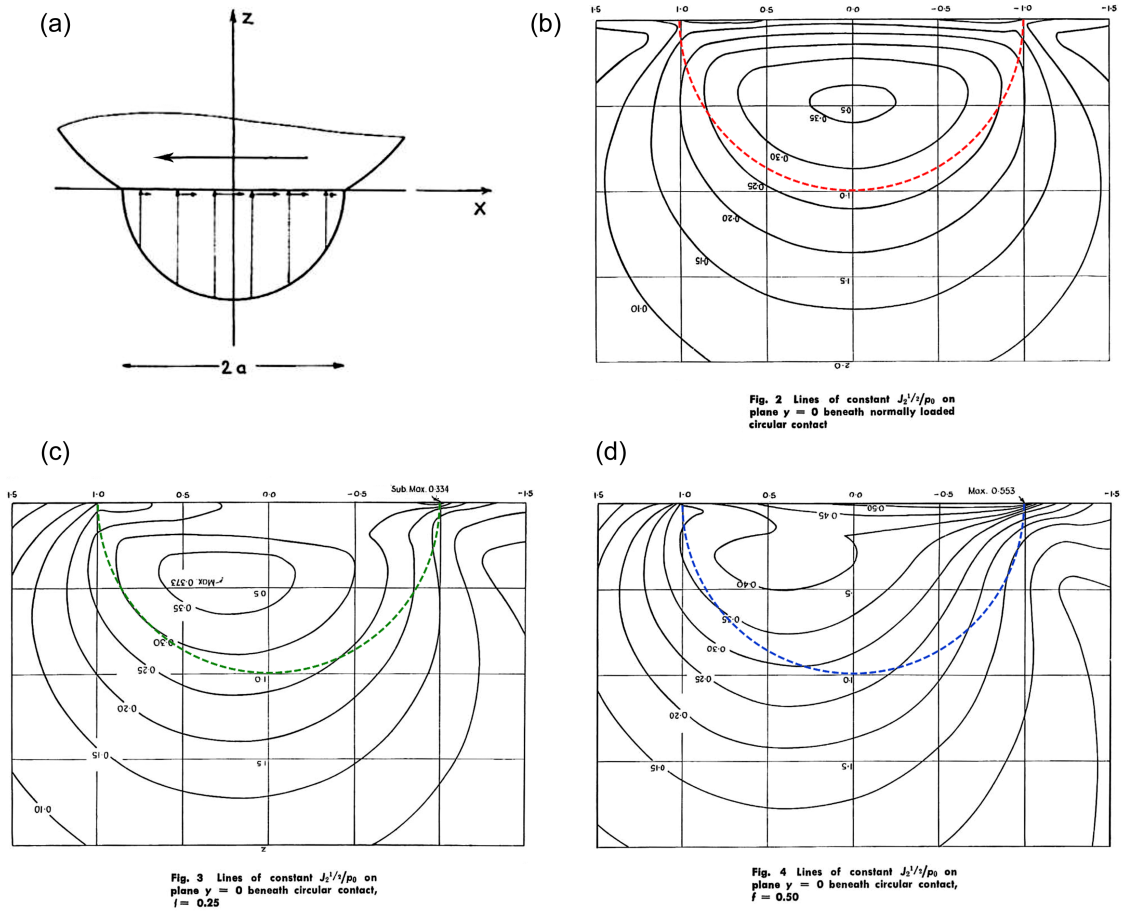

Fig. 2 Lines of constant $J_2^{1/2}/p_0$ on plane $y = 0$ beneath normally loaded circular contact

Fig. 3 Lines of constant $J_2^{1/2}/p_0$ on plane $y = 0$ beneath circular contact, $f = 0.25$

Fig. 4 Lines of constant $J_2^{1/2}/p_0$ on plane $y = 0$ beneath circular contact, $f = 0.50$

Figure 3.6: (a) A coordinate of the analysis where the frictional force exerting in $+x$-direction. (b-d) contour lines of $\sqrt{J_2}/P_{max}$ at various friction coefficients where dotted lines represent the hemispherical domain. With greater of the coefficient, the sub-surface maximum shear stress increases and its location moves toward the surface. (Reprinted from [7])

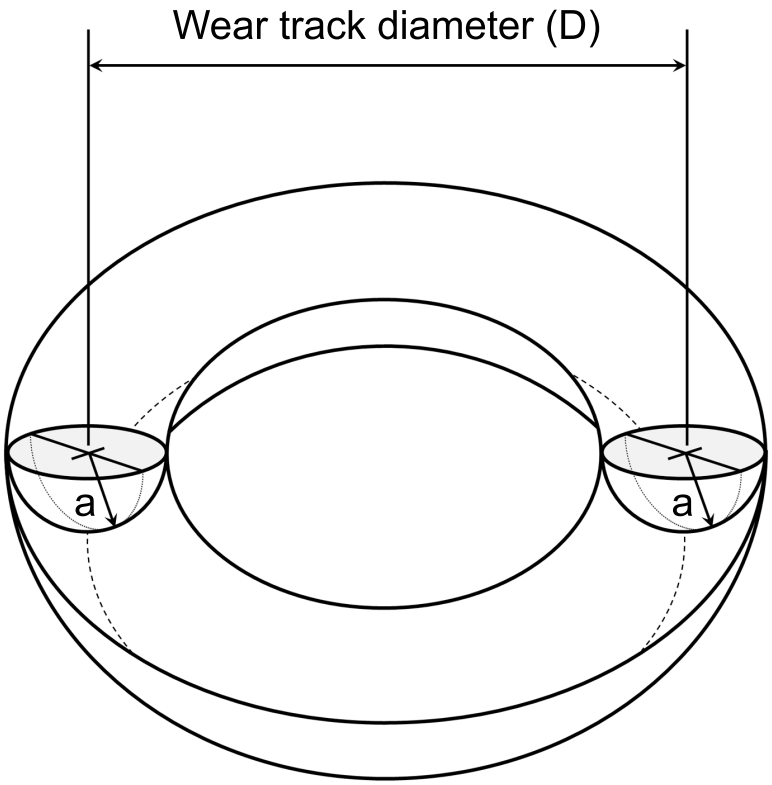

Figure 3.7: An overall deformation domain of a sphere-plane sliding contact can be viewed as a half of ring torus.

Chapter 4

Influence of applied loads and volume fraction on triboluminescence behavior of the particulate luminescent composites

4.1 Introduction

Triboluminescence (TrL) is a light emission phenomena by an external mechanical excitation, particularly for sliding contact; it is interchangeably called as mechanoluminescence (ML). Regardless of excitation source, a color of the emission from phosphors is an attribution of a level-splitting of doping elements as the result of crystal field effect [1]. Although ML has been discovered in various types of inorganic compounds for decades, i.e. doped ZnS, $ZnAl_2O_4$:Mn or rare-earth doped $SrAl_2O_4$ [2, 3], its mechanism is still debatable.

At the present time, there are two empirical theories explaining on the phenomenon. The first theory, established by *S.I. Bredikhin et. al* whom investigated the emission behavior of single crystals of doped ZnS, concluded that a motion of charged partial dislocations due to a plastic deformation introduces the electrical charges on the surface of the crystals. A surface electroluminescence pulse consisting of a characteristic emission band of Mn centers at 585 nm may be produced either by overcoming the breakdown voltage [4] or electron tunneling caused by sufficiently strong electric potential near the core of charged dislocations [5].

Later, *B.P. Chandra* and his colleges contended that such explanation is not suitable since the emission was also observed on the hydrostatically compressed Mn-doped ZnS phosphors [6], they therefore suggested that the observed luminescence is likely to be attributed to a piezo-electric field [7] and/or a triboelectricity [8] which allows electrons to be tunneled. Despite a

concise relationship of ML intensity and the applied pressure, others physical parameters, e.g. a volume fraction of the luminescent particles, phase composition or mechanical properties of the individual components, have not been taken into consideration for the case of composites.

In this chapter, the influence of external applied forces and volume fraction on frictional deformation-induced emission of ZnS:Mn/polyester resin composite is investigated by utilizing the constructed triboluminescence acquisition system mentioned in chapter 2.

4.2 Experimental procedure

4.2.1 Sample preparations

Samples were fabricated from an unsaturated polyester resin and ZnS:Mn powders, provided by Kojundo Chemical Laboratory, Japan, at 0.5 at% manganese concentration. Morphology of as-received phosphors are pebble-like particles (Fig. 3.1(a)) with an average size of 5 μm. According to XRD diffraction patterns, a hexagonal wurtzite structure with nearly random orientation, as shown in and Fig. 3.1(b), respectively. Two volumetric contents of ZnS:Mn, denoted as v_f, were prepared at 5.57 and 22.28 vol%. A moderate amount of the catalyst, i.e. methyl ethyl ketone peroxide, at 4% of the total mass was used for preventing particle sedimentation. The mixture was cast into a cylindrical polypropylene mold with a diameter of 30 mm and cured in an evacuated desiccator for 24 hours. To reproduce the identical surface roughness, the sample was polished with a 800-grit abrasive paper prior to each measurement.

4.2.2 Measurements and characterizations

Constructed triboluminescence measuring instrument is pin-on-disc model utilizing a soda-lime glass rod as sliding pin to maximize photon detection. Contact end was sharpened into a spherical tip at diameter of 825 micrometers. Triboluminescence intensity was measured by a Hamamatsu H10723-20 photomultiplier tube and its spectra were monitored using a Hamamatsu C10083-CA spectrometer. Normal load is adjustable by applied cable tension. Exerting forces and friction coefficient were determined from the deflection of elastic arm that is made of poly(methyl methacrylate) using strain gauges. Amplified gauge signals and photomultiplier

voltage were simultaneously recorded by a Graphtec GL900 multichannel data-logger.

Applied normal force was simultaneously measured with friction force as the deflection of strain-gauge attached elastic arm in which is made of poly(methyl methacrylate) polymer. Strain gauge signals were separately amplified by two cascaded LT1167 precision instrumentation operational amplifiers. All output voltages were recorded by a Graphtec GL900 data-logger. Three measurements were conducted for each loading and ZnS:Mn concentration conditions.

Loading conditions were from 0.25 to 2.00 N with constant rotational speed and track diameter of 90 RPM and 15 mm, respectively. Wear track morphologies were observed using a JEOL JSM-7000F field-emission scanning electron microscope.

4.3 Results and Discussions

4.3.1 Triboluminescence characteristics

Observed TrL emission spectrum (Fig. 4.2(a)) exhibits a broad peak at wavelength of 585 nm resembling to those of photoluminescence [9] and electroluminescence [10, 11] This suggests that stress-induced luminescence of the composite is originated solely from the phosphors. While a peak intensity tentatively increases with applied normal loads, its position is found to be force-independence implying that intermediate energy levels of Mn centers are not be influenced by external excitation. The observations are in good agreement with the report on a cyclic loading rate-independent emission spectrum of ZnS:Cu,Mn embedded in polydimethylsiloxane matrix [12].

Typical time-dependent TrL intensity and measured friction coefficient is are illustrated in Fig. 4.3. Luminescence is immediately observed as sliding started with an obvious fact that higher loading force produces stronger intensity without causing a significant change in friction coefficient. The value of friction coefficient is about 0.3–0.4 regardless of phosphor concentrations and normal loads which is within the reported range of pure polyester resin [13].

Triboluminescence intensity is considerably high at the early stage and followed by rapid convergence to a certain equilibrium value. Intense emission at the beginning is likely to be

due to a deformation of asperities. An average value of PMT voltage deduced from the second rotation, that is $\Delta t = 0.67$ second, is used to represent a total intensity in order to avoid any error contributed by surface roughness or stick-slip.

4.3.2 Correlation of tribological behavior and mechanical properties of the composite

Large oscillations in friction coefficient are observed after particular sliding distance on conditions with moderate normal load (for constant phosphor content) or low volume fraction (for constant applied force), clearly seen in Fig. 4.3**b** and Fig. 4.3**c**. a stick-slip that manifesting in a low-stiffness contacting system with insufficient lubrication and subjected to rapid change in tangential force [14, 15] which is consistent with wear track observations.

An improvement in stiffness of the composite due to volumetric content can be demonstrated by the reduction of track width. It reduces from about 100 μm to 80 μm for the case of $v_f = 5.57\%$ and $v_f = 22.28\%$ respectively which is in very good agreement to the calculated value at loading force of 2.00 N. Scuffing marks in which perpendicular to sliding direction are also the indicator of an abrupt change in exerting friction on contacting surface [14]. This observation evidences aforementioned stick-slip phenomenon.

An average value of PMT voltage deduced from the second cycle is used as the total emission intensity to avoid an overestimation due to surface roughness or stick-slip.

4.3.3 Relationship of TrL intensity and external parameters

Figure 4.5 shows that the emission intensity is likely to be proportional to applied normal loads which is considerably consistent to previous reported results [2, 16]. The result is comparatively in accordance with the predicted TrL intensity-applied force relationship mentioned in section 3.2.4. Additionally, more intense luminescence response is apparently achievable by higher content of phosphors as a consequence of the direct increase in emission probability. As discussed earlier, the mechanical properties of particulate composite is greatly governed by phase concentration so that a volumetric content of ZnS:Mn should therefore exhibit an

additional influence on triboluminescence behavior via controlling mechanical responses.

By following the procedures given in section 3.3, a correlative plot of TrL intensity and equivalent stress is obtained as shown in Fig. 4.6. Luminescence intensity increases nonlinearly with the stress which is distinctive from the plot using applied force as variable. This suggests that the correlation might be reported differently even with identical experimental conditions. Likewise a similarity between emission intensity and stress distribution, the results hence signify that the most appropriate comparative parameter is rather apparent stress.

Nonlinearity of the luminescence and the stress within elastic limit has reported previously such as empirical suggestion by *G. Alzetta et. al* as $\exp(k\Delta P^2)$ where ΔP is a magnitude of applied pressure [6] or a quadratic function proposed by *B. P. Chandra et. al* developing based on a concept of piezoelectric field-induced detrapping model [7, 17–21].

Considering the current accepted theory, a total TrL intensity is proportional to stress squared, i.e. $I = k_0\sigma^2$, where k_0 is a factor which is independent of ZnS:Mn volume fraction. Despite a good linearity when zero loading condition is omitted as depicted in Fig. 4.7, a slope of the fitting curve from different phosphor contents is not identical where a ratio of determined slopes is intriguingly close to a ratio of volume fractions. This implies that not only is the mechanical properties improved but also the emission probability of the composite is directly increased by higher volumetric concentrations.

4.4 Summaries

Influence of the applied normal loads on the emission behavior of ZnS:Mn/polyester resin composite due to sliding deformation has been investigated. Luminescence is an attribution to phosphors whose emission wavelength is not affected by external force. Triboluminescence intensity strongly depends on an amount of the luminescent phase incorporated in the composite and the stress acting on the bodies which can be controlled by an external normal loading condition or an internal mechanical properties of the composite. In addition to an approximately linear increment of emission intensity with applied forces, such relationship of triboluminescence and exerting stress is likely to be described as a nonlinear exponential growth.

Reference

[1] Yen, W., Shionoya, S., and Yamamoto, H. *Fundamentals of Phosphors*. CRC Press, (2007).

[2] Xu, C., Watanabe, T., Akiyama, M., and Zheng, X. *Mater. Res. Bull.* **34**, 1491–1500 (1999).

[3] Olawale, D., Dickens, T., Sullivan, W., Okoli, O., Sobanjo, J., and Wang, B. *J. Lumin.* **131**, 1407–1418 (2011).

[4] Bredikhin, S. and Shmurak, S. *Sov. Phys.-JETP* **46**(4), 768–773 (1977).

[5] Bredikhin, S. and Shmurak, S. *Sov. Phys.-JETP* **49**(3), 520–524 (1979).

[6] Alzetta, G., Minnaja, N., and Santucci, S. *Il Nouvo Cimento* **23**, 910–913 (1962).

[7] Chandra, B., Baghe, R., and Chandra, V. *Chalcogenide Letters* **7**(1), 1–9 (2010).

[8] Matsui, H., Xu, C., Liu, Y., and Tateyama, H. *Phys. Rev. B* **69**, 235109 (2004).

[9] Bhargava, R., Gallagher, D., Hong, X., and Nurmikko, A. *Phys. Rev. Lett.* **72**, 1–4 (1994).

[10] Tanaka, S., Kobayashi, H., Sasakura, H., and Hamakawa, Y. *J. Appl. Phys.* **47**(12), 5391–5393 (1976).

[11] Skolnick, M. *J. Phys. D: Appl. Phys.* **14**(2), 301–322 (1981).

[12] Jeong, S., Song, S., Lee, S., and Ha, N. *Adv. Mater.* **25**(43), 6194–6200 (2013).

[13] El-Sayed, A., El-Sherbiny, M., Abo-El-Ezz, A., and Aggag, G. *Wear* **184**(1), 45–53 (1995).

[14] Stachowiak, G. and Batchelor, A. *Engineering Tribology-3rd edition*. Butterworth-Heinemann, (2005).

[15] Larsen-Basse, J. *Introduction to friction, ASM Handbook Volume 18, Friction, Lubrication, and Wear Technology*. ASM International, (1992).

[16] Xu, C., Watanabe, T., Akiyama, M., and Zheng, X. *Appl. Phys. Lett.* **74**(9), 1236–1238 (1999).

[17] Chandra, V. and Chandra, B. *Opt. Mater.* **34**, 194–200 (2011).

[18] Chandra, B. *The Open Nanoscience Journal* **5**, 45–58 (2011).

[19] Chandra, B. *Int. J. Lumin. Appl.* **2**(3), 44–72 (2012).

[20] Tiwari, R., Dubey, V., and Chandra, B. *Mater. Phys. Mech.* **19**, 25–38 (2014).

[21] Chandra, V., Chandra, B., and Jha, P. *Appl. Phys. Lett.* **103**(16), 161113–1–5 (2013).

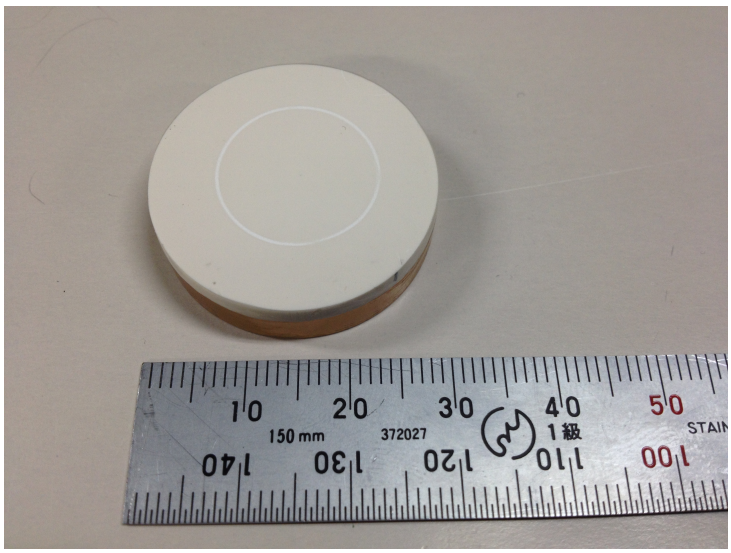

Figure 4.1: A composite specimen of ZnS:Mn particles and polyester resin.

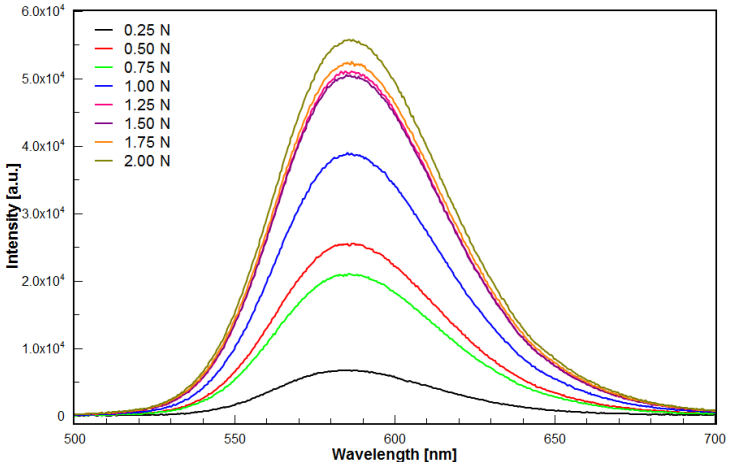

(a)

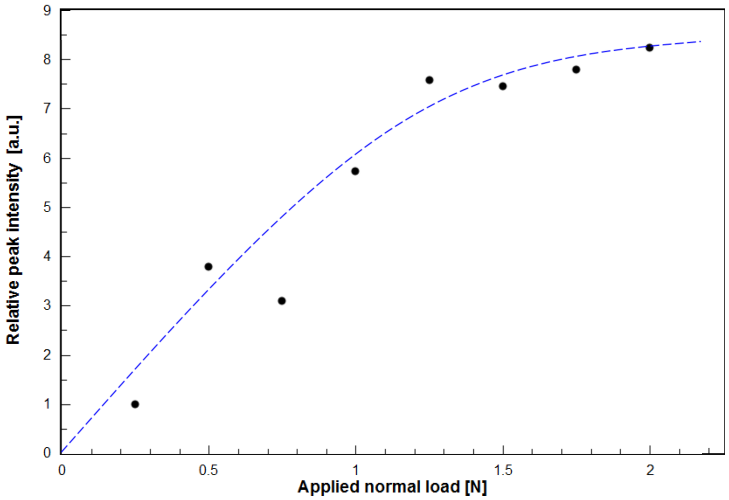

(b)

Figure 4.2: (a) Emission spectra of triboluminescence of ZnS:Mn phosphors whose peak intensity (b) tentatively increases with higher applied normal load.

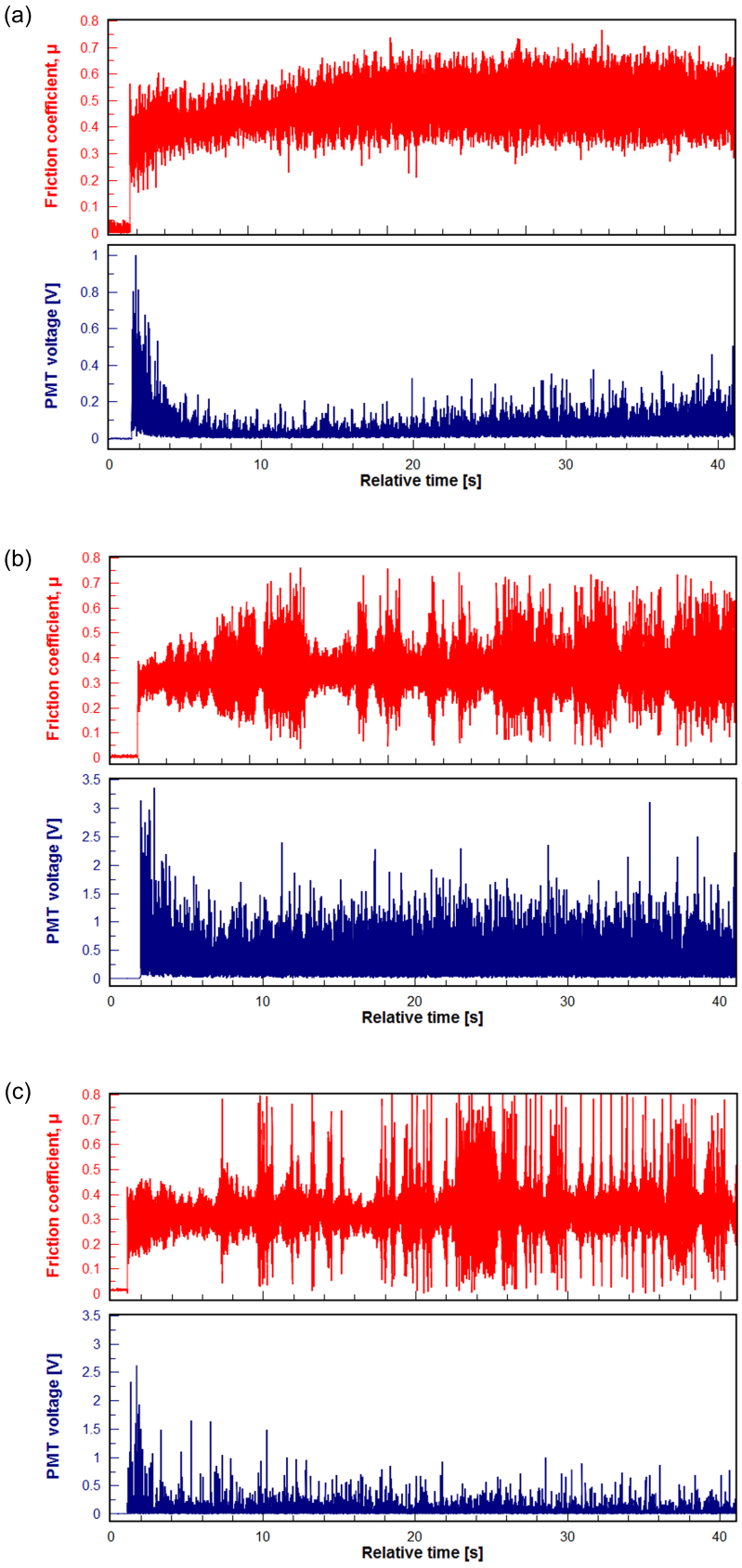

Figure 4.3: Typical pattern of emission behavior comparing to the measured friction coefficient of (a) $W = 0.50$ N and $v_f = 22.28\%$, (b) $W = 2.00$ N and $v_f = 22.28\%$ and (c) $W = 2.00$ N and $v_f = 5.57\%$.

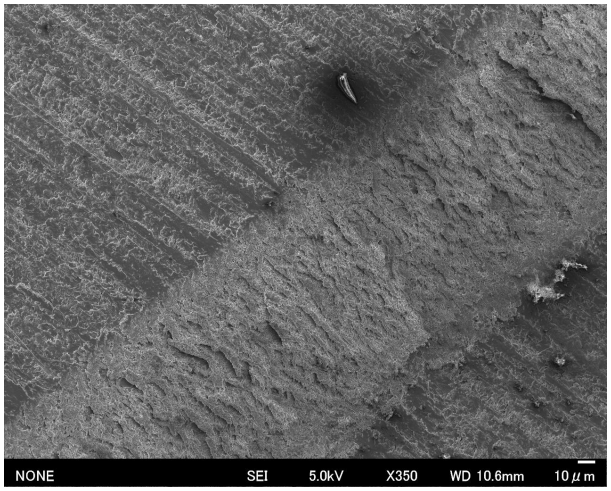

(a)

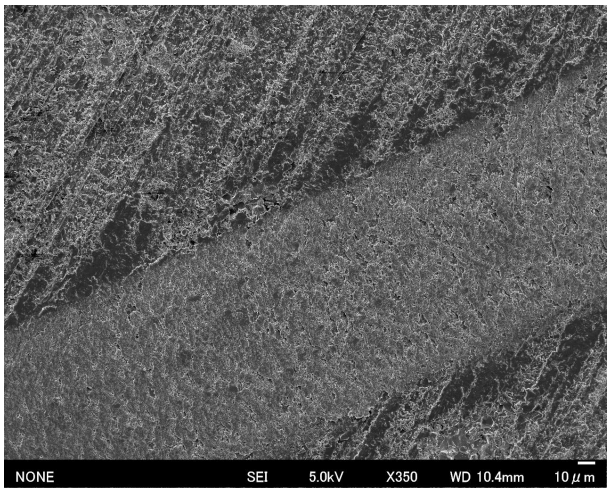

(b)

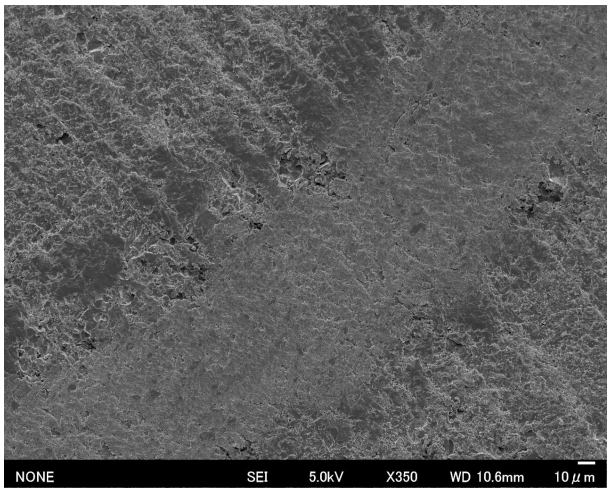

(c)

Figure 4.4: SEM images of wear track of (a) $v_f = 0.0\%$, (b) $v_f = 5.57\%$ and (c) $v_f = 22.28\%$.

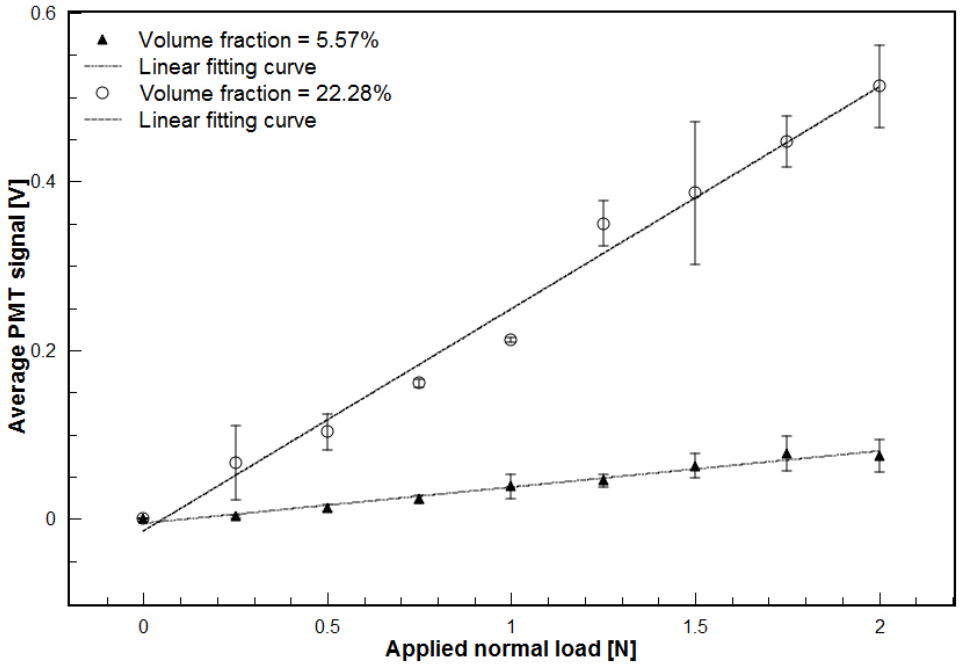

Figure 4.5: Triboluminescence intensity is strongly controlled by either of volumetric content of ZnS:Mn particles or external loading force.

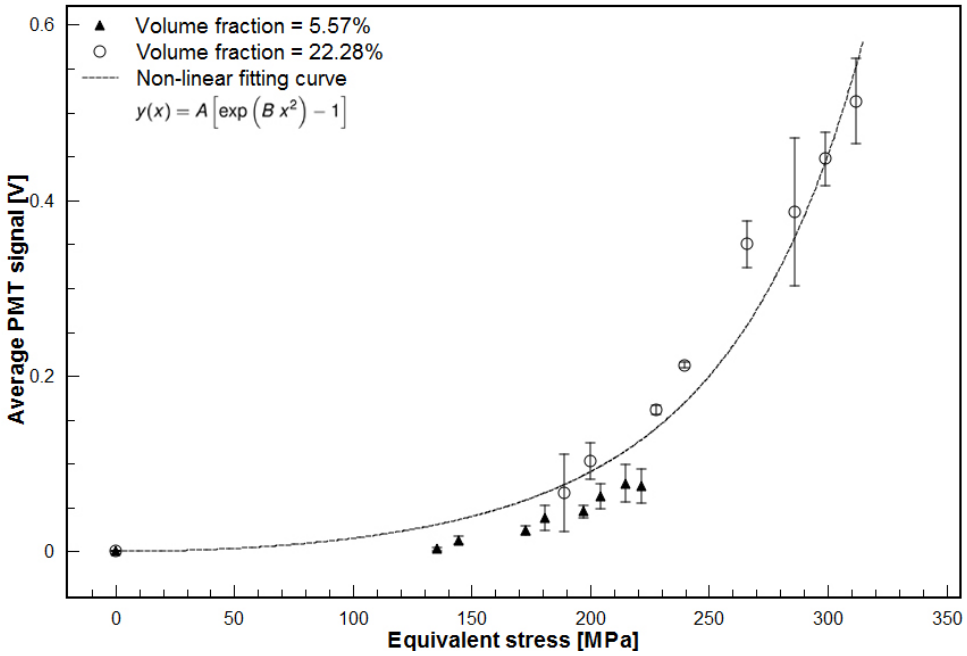

Figure 4.6: A correlative plot of triboluminescence intensity and the determined equivalent stress shows nonlinear relationship.

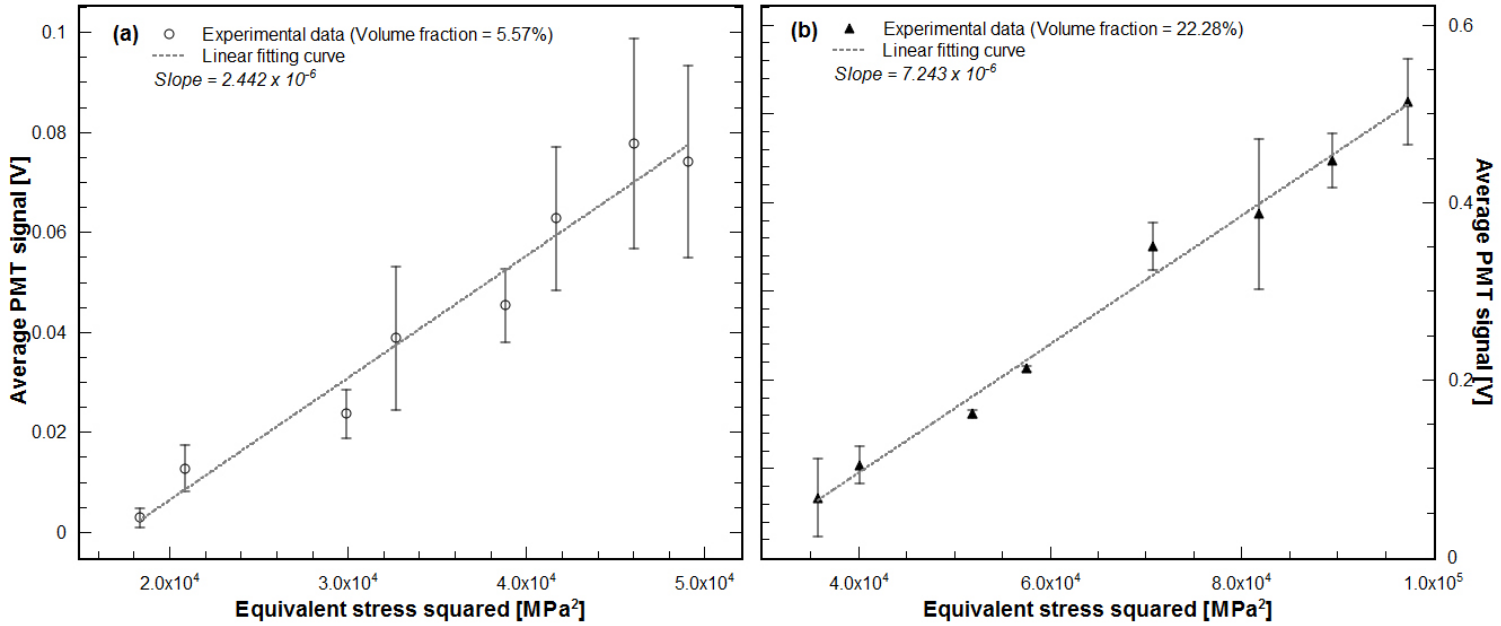

Figure 4.7: Total emission intensity is proportional to equivalent stress squared of **(a)** $v_f = 5.57\%$ and **(b)** $v_f = 22.28\%$.

Chapter 5

Mechanoluminescence and its correlation to impact energy and contact geometry

5.1 Introduction

As discussed in the preceding chapters, a visible light emission of substances being subjected to a mechanical stimulation is known as mechanoluminescence (ML) which can be found in several types of doped inorganic sulfides/oxides or organic compounds such as ZnS [1–3], $ZnAl_2O_4$ [4], $SrAl_2O_4$ [5–8], CaZnOS [9] or Europium tetrakis(dibenzoylmethide)triethylammonium [10, 11]. Although this behavior has not been fully implemented in any commercial product yet, the potential application is suggested as a modern visual force/stress sensor that might be applicable for an earthquake detection or a structural health monitoring [12, 13].

Comparing with other non-complex mechanoluminescent crystals, zinc sulfide doped with manganese is one of the excellent candidate phosphors due to its inexpensiveness, the relatively superior ML performance [1] and the outstanding reproducibility [2, 14]. Mechanoluminescent spectrum of ZnS:Mn exhibits a broad peak centering around 585 nm that is similar to the emission caused by photo-excitation [15] or external electric field [16, 17]. It is an attribution to the characteristic $^4T_1 \rightarrow ^6A_1$ energy transition of substitutional manganese centers [18, 19].

One of the frequently cited model for mechanoluminescent property has been developed based on the principle of piezoelectric field-associated electron detrapping mechanism by *B.P. Chandra* and his colleagues. Total and peak intensity are likely to increase non-linearly with the applied pressure or stress in which might be able to express as a simple quadratic relationship [14, 20, 21]. Besides, luminescent quantity is also suggested to be related to the

deformational energy, i.e. $\frac{1}{2}\frac{\sigma^2}{E}$ where σ and E refer to the stress and an elastic modulus, accordingly [14].

On the basis of energy conversion, a proportionality between ML intensity and the dropping distance or the square of impact velocity is therefore expected for impulsive deformation tests.

In spite of a favorable prediction using above mentioned expression on the projectile-based experimental results [9, 22–24], in fact, a direct correlation between the impact energy and the applied stress is less realistic and partly validates since there are not only the exerting force but also the mechanical properties and geometrical parameters of contacting solids governing the response internal stress [25, 26].

Hence, the objective is to investigate the effect of impact energy and a contribution of contact geometry on mechanoluminescent intensity of ZnS:Mn phosphors using an impulsive impact testing equipment.

5.2 Experimental procedure

The specimen was fabricated as a composite material of a transparent unsaturated polyester resin and a commercial ZnS:Mn at doping concentration of 0.5 at%, purchased from Kojundo Chemical Laboratory (Saitama, Japan), at 20% volume fraction of the phosphors. A curing process of resin was initialized using 5.0 wt% of methyl ethyl ketone peroxide for 15 minutes before incorporating with the particles to ensure uniform distribution. The mixture being casted into an aluminum crucible was fully cured at 50°C for 4 hours and resulting in the final shape of a circular disk at a diameter of 8 mm and thickness of 4 mm (Fig. 5.1(a)).

A schematic drawing of the experimental setup is depicted in Fig. 5.1(c) which composes of three main components: (I) a machine frame made with two thick stainless steel plates separating by four M8 stainless steel screw rods, (II) an 10 mm-thick aluminum see-saw lever (Fig. 5.1(b)) installed with a striking pin and (III) an impact hammer constructed from a stainless steel block attached on a 6 mm-diameter stainless steel rod at a distance L of 180 mm from the fulcrum. A rest mass m of the hammer including its arm is measured to be 41 g so that the potential energy can be calculated using $mgL\sin\theta$ at different impacting angles

($\theta = 15^\circ, 30^\circ, 45^\circ, 60^\circ$ and 90°). The specimen was attached onto the upper machine frame using a two-side adhesive tape.

Two striking pins with different tip diameters Φ_{tip} of 0.77 mm and 2.18 mm were made out of a 6 mm-diameter fused silica rod. A length from the tip to another side is 5 mm. Each pin was secured into a 6-mm diameter socket on the individual lever by a cyanoacrylate-based strain-gauge adhesive. Emitted photons were introduced onto a large photosensitive area S6967 Si PIN photodiode (Hamamatsu Photonics, Japan) through a concentric 5 mm through-hole for maximizing the optical aperture. The sensor, locating 8 mm away from the pin, and cables were permanently bonded to the bar using a standard Araldite® epoxy to improve the stability of structure and electrical connections.

The photodiode operated in a photovoltaic mode so that the diode current I_{PD} is proportional to the incident light flux with low noise background. The electrical current was converted into measurable voltage using a transimpedance amplifier circuit of OPA2134 operational amplifiers (Texas Instrument, United States) as illustrated in Fig. 5.2. Amplified voltage V_{out} equals to $R_f \times I_{PD}$ where R_f refers to a feedback resistor. It is important to notify that a $1 \pm 1\%$ MΩ resistor was used in place of $4 \pm 1\%$ MΩ for the conditions of (a) Φ_{tip} = 0.77 mm, $\theta = 60^\circ$ and (b) Φ_{tip} = 0.77 mm, $\theta = 90^\circ$ to avoid a saturation of the signal near the supplied rails. The output voltage was recorded using a GL900 data logger (Graphtec, Japan). Ten measurements were conducted for each of conditions. Prior to the consecutive experiment, the sample was polished by 1,200-grit abrasive paper to remove the previous indentation.

Total emission intensity I_t is determined from an area under the transient ML response curve using Eq. 5.1 where ΔT is an integration time of 10 ms,

$$I_t = \frac{\int I \mathrm{d}t}{\Delta \mathrm{T}}. \tag{5.1}$$

5.3 Results and Discussions

Figure 5.3(a) shows a typical transient ML response of ZnS:Mn phosphors which exhibits a pulse-like emission containing two distinguishable peaks. Such waveform has been observed in previous researches and suggested to be due to the change of applied stress during load-

ing/unloading process [6, 14, 27]. Thus, it is highly possible that an impression and an removal of the pin produces the primary and the secondary peak respectively.

C.N. Xu et. al emphasized a similarity of ML patterns to the electrical outputs of PZT piezoelectric crystals during the increase and the decrease of applied stress [2]. In this study, the first peak intensity is always higher than that of the secondary in which contradicts to their observation so that the luminescent level may correlate to a relaxation of the plastic- and the elastic deformation energy respectively. Further investigations are needed to verify such correlation.

When the pin with smaller diameter ($\Phi_{\text{tip}} = 0.77$ mm) was used, two-peaks emission behavior starts to be unobservable; a number of experimental tests showing such pattern is less than 70%. At relatively high impulsive energy (> 60 mJ), ML emission pattern becomes a single-peak pulse as shown by a dotted-curve in Fig. 5.3(b). Fractoluminescence might be account for the phenomenon since the applied energy is totally dissipated for a creation of new cleaved surfaces.

Time required to observe the first peak and the interval period are approximately constant at 200 ± 45 μs and 2.4 ± 0.8 ms respectively, regardless of the impact energy or tip diameter. While the first decay curves are found to be incapable of being perfectly fitted by either mono- or biexponential function, the second decaying behavior considerably follows the first-order exponential decay. Rise time, the first- and the second decay constant, are also independent to the external parameters with an average value of 40 ± 8 μs, 0.7 ± 0.3 ms and 1.1 ± 0.3 ms accordingly. The decay constant is in good accordance with the reported value measured by photoluminescence spectroscopy [17, 28].

It is noteworthy to mention that a restriking of the pin is not responsible for two-peaks emission behavior. It is not only because of a substantial short interval between separated peaks, time but also the appearance of additional low-intensity pulse detected in several tens of milliseconds after the first pulse (Fig. 5.3(c)).

The correlation of the maximum and the total ML intensity to impacting energies are shown in Fig. 5.4 and Fig. 5.5 accordingly. It is obvious that the higher energy introduced to the luminescent material, the more emitted photons are generated. For a large tip radius (Fig. 5.4(a)

and 5.5(a)), both luminescence quantities increase linearly with the applied energy, on the other hand, such linearity is only observed at the limited range, i.e. ≤ 40 mJ, in case of small tip diameter as seen in Fig. 5.4(b) and 5.5(b).

According to the conservation of momentum, that is $\int F\mathrm{d}t \approx F_{\mathrm{ave}}\Delta t = m\int \mathrm{d}v$, an average force F_{ave} can be treated as the constant at particular impact energy in case that the observed time parameters are invariant. Due to an identical length of the pin-to-fulcrum and the striker-to-fulcrum, it is reasonable to consider that an exerting force is equivalent to that of generated by a direct impact on the pin if the mechanical loss is negligible.

By taking the interval time as Δt, the estimated average force is ranging from 16.33 to 32.10 N which is likely be sufficient to induce plastic deformation since the pin diameter and forces are comparable to the ball diameter and minor load of Rockwell superficial hardness testing [29].

As the dissipated energy of plastic deformation is also proportional to the square of the stress (see Eq.3.2.32–Eq.3.2.34 in [30]), it is difficult to conclude that the elastic deformation is a predominant responsible for the observed linear relationship, in which being suggested in [14, 20, 21]. In this study, the plastic deformation is therefore strongly accounted for impulsive-induced light emission.

It is important to mention that such linear tendency still supports the quadratic relationship of mechanoluminescence and the applied stress or energy.

Stronger ML intensity caused by a reduction of tip radius at the similar applied energy signifies a contribution of contacting geometries. In contact mechanics, a circular region is created under a sphere-plane contacting configuration with the radius given by [25, 26],

$$a = \left[\frac{3}{8}\, d\left(\frac{1-\nu_1^2}{E_1} + \frac{1-\nu_2^2}{E_2}\right)\right]^{1/3} \sqrt[3]{F}, \tag{5.2}$$

where d is a diameter of sphere, ν is a Poisson ratio, E is an elastic modulus and F is a normal force. Subscript 1 and 2 refer to each contacting solids.

Inserting Eq. 5.2 into the maximum surface pressure, that is $\sigma_{\mathrm{H}} = 1.5F/(\pi a^2)$, the Hertzian stress boundary condition and its corresponding internal stress is proportion to $d^{-2/3}$ and there-

fore yields,

$$\frac{\sigma^2(d_1)}{\sigma^2(d_2)} = \left(\frac{d_2}{d_1}\right)^{4/3}. \tag{5.3}$$

Equation 5.3 is calculated to be 4.00 for the tip geometries used in this study which is reasonably close to a ML intensity ratio considering in range of ≤ 40 mJ, i.e. 3.36 and 4.57 for the peak and the total emission respectively. The result suggests that it is more appropriate to express mechanoluminescent behavior as a function of the stress rather than the energy as the influence of contact geometrical parameter are taken into consideration. In other words, a deformation with concentrated stress distribution is essential for producing ML effect.

It is reasonable to suggest that an application of high impact energy on the confined area can cause the fracture of ZnS:Mn particles so that a fractoluminescence emerges in addition to a non-destructive emission. Such luminescence should therefore yield higher ML intensity than that of the prediction.

5.4 Conclusions

It has been demonstrated that it is not only the magnitude of applied energy but also the geometrical parameters of contacts in which determine the intensity of mechanoluminescence of ZnS:Mn dispersed in polyester resin matrix. The results therefore signify a significant correlation between ML effect and exerting stress.

Reference

[1] Xu, C., Watanabe, T., Akiyama, M., and Zheng, X. *Mater. Res. Bull.* **34**, 1491–1500 (1999).

[2] Xu, C., Watanabe, T., Akiyama, M., and Zheng, X. *Appl. Phys. Lett.* **74**(9), 1236–1238 (1999).

[3] Xu, C., Watanabe, T., and Akiyama, M. *J. Am. Ceram. Soc.* **82**(9), 2342–2344 (1999).

[4] Matsui, H., Xu, C., Liu, Y., and Tateyama, H. *Phys. Rev. B* **69**, 235109 (2004).

[5] Shon, K.-S., Seo, S., Kwon, Y., and Park, H. *J. Am. Ceram. Soc.* **85**(3), 712–714 (2002).

[6] Jia, Y., Yei, M., and Jia, W. *Opt. Mater.* **28**(8–9), 974–979 (2006).

[7] Someya, S., Ishii, K., Saeki, M., and Munakata, T. *Opt. Lett.* **38**(7), 1095–1097 (2013).

[8] Rahimi, M., Yun, G., and Choi, J. *Acta Mater.* **77**, 200–211 (2014).

[9] Zhang, J., Xu, C., Kamimura, S., Terasawa, Y., Yamada, H., and Wang, X. *Opt. Express* **21**(11), 12976–12986 (2013).

[10] Sage, I. and Bourhill, G. *J. Mater. Chem.* **23**(2), 231–245 (2001).

[11] Bourhill, G., Pålsson, L., Samuel, I., Sage, I., Oswald, I., and Duignan, J. *Chem. Phys. Lett.* **336**, 234–241 (2001).

[12] Olawale, D., Dickens, T., Sullivan, W., Okoli, O., Sobanjo, J., and Wang, B. *J. Lumin.* **131**, 1407–1418 (2011).

[13] Xu, C. *Mechanoluminescence and Novel Structural Health Diagnosis*. NTS shuppan, (2012).

[14] Chandra, B., Xu, C., Yamada, H., and Zheng, X. *J. Lumin.* **130**, 442–450 (2010).

[15] Bhargava, R., Gallagher, D., Hong, X., and Nurmikko, A. *Phys. Rev. Lett.* **72**, 1–4 (1994).

[16] Tanaka, S., Kobayashi, H., Sasakura, H., and Hamakawa, Y. *J. Appl. Phys.* **47**(12), 5391–5393 (1976).

[17] Skolnick, M. *J. Phys. D: Appl. Phys.* **14**(2), 301–322 (1981).

[18] Yen, W., Shionoya, S., and Yamamoto, H. *Fundamentals of Phosphors*. CRC Press, (2007).

[19] Chen, W., Sammynaiken, R., Huang, Y., Malm, J., Wallenberg, R., Bovin, J., Zwiller, V., and Kotov, N. A. *J. Appl. Phys.* **89**(2), 1120–1129 (2001).

[20] Chandra, V. and Chandra, B. *Opt. Mater.* **34**, 194–200 (2011).

[21] Tiwari, R., Dubey, V., and Chandra, B. *Mater. Phys. Mech.* **19**, 25–38 (2014).

[22] Womack, F., Goedeke, S., Bergeron, N., Hollerman, W., and Allison, S. *IEEE Trans. Nucl. Sci.* **51**(4), 1737–1741 (2004).

[23] Sharma, R., Bisen, D., Dhoble, S., Brahme, N., and Chandra, B. *J. Lumin* **131**(10), 2089–2092 (2011).

[24] Jha, P. and Chandra, B. *J. Lumin* **143**, 280–287 (2013).

[25] Johnson, K. *Contact Mechanics*. Cambridge University Press, (1985).

[26] Stachowiak, G. and Batchelor, A. *Engineering Tribology-3rd edition*. Butterworth-Heinemann, (2005).

[27] Alzetta, G., Minnaja, N., and Santucci, S. *Il Nouvo Cimento* **23**, 910–913 (1962).

[28] Gumlich, H.-E. *J. Lumin.* **23**, 72–99 (1981).

[29] ASTM E18–03e1, Standard Test Methods for Rockwell Hardness and Rockwell Superficial Hardness of Metallic Materials, ASTM International, West Conshohocken, PA, 2003.

[30] Kojić, M. and Bathe, K.-J. *Inelastic Analysis of Solids and Structures*. Springer-Verlag GmbH, (2005).

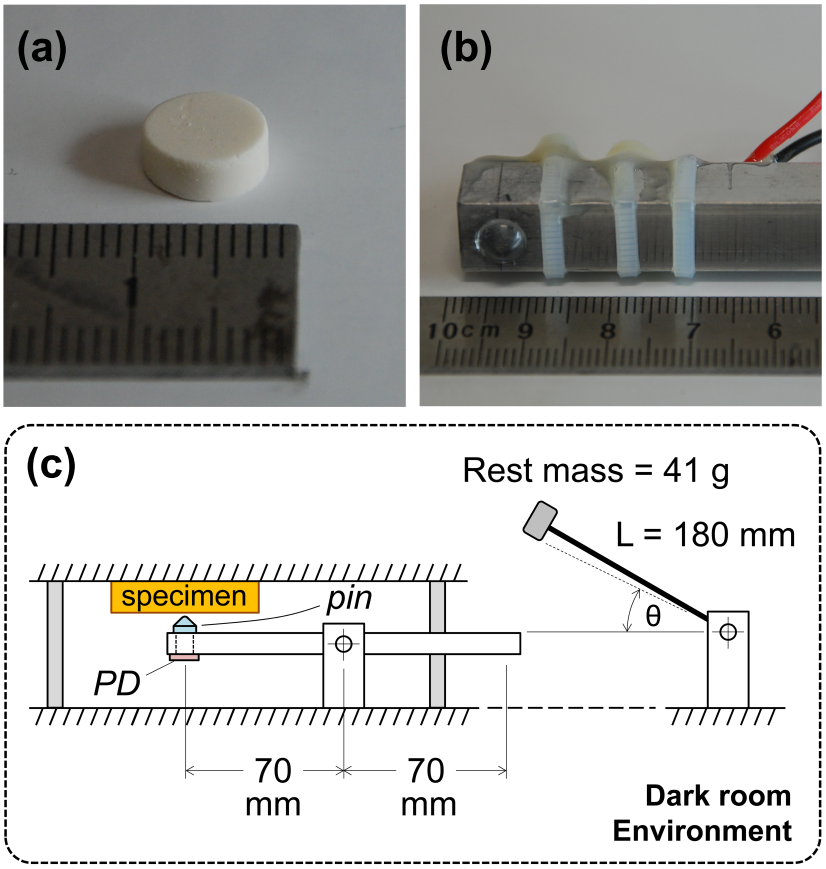

Figure 5.1: (a) Composite specimen of ZnS:Mn and the resin, (b) The loading lever with a striking pin and the photodiode in which coupled at the back of the bar and (c) a schematic of an impact testing setup using in the study where *PD* denotes the photodiode.

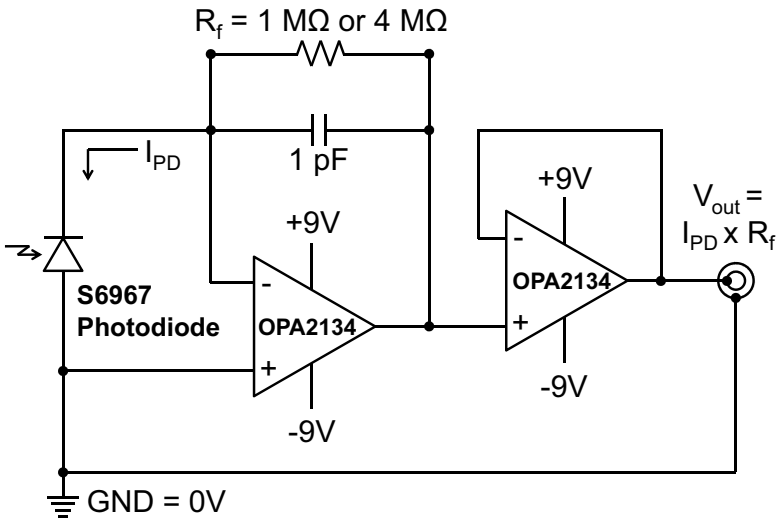

Figure 5.2: A current-to-voltage converting circuit using OPA2134.

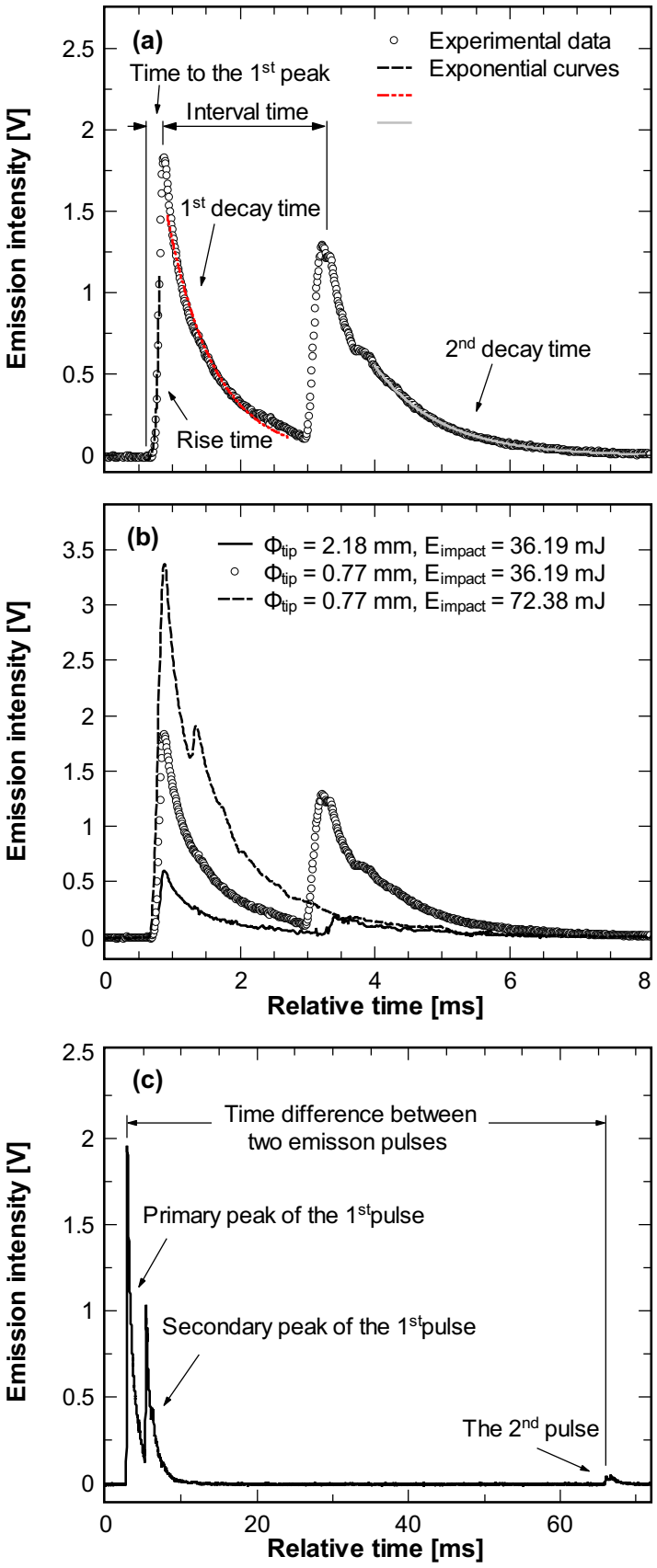

Figure 5.3: (a) Time-dependent ML intensity of ZnS:Mn subjected to impulsive load and (b) the emission characteristics observed at different experimental conditions. Both (a) and (b) share the same horizontal scale and (c) a small pulse observing after the first emission.

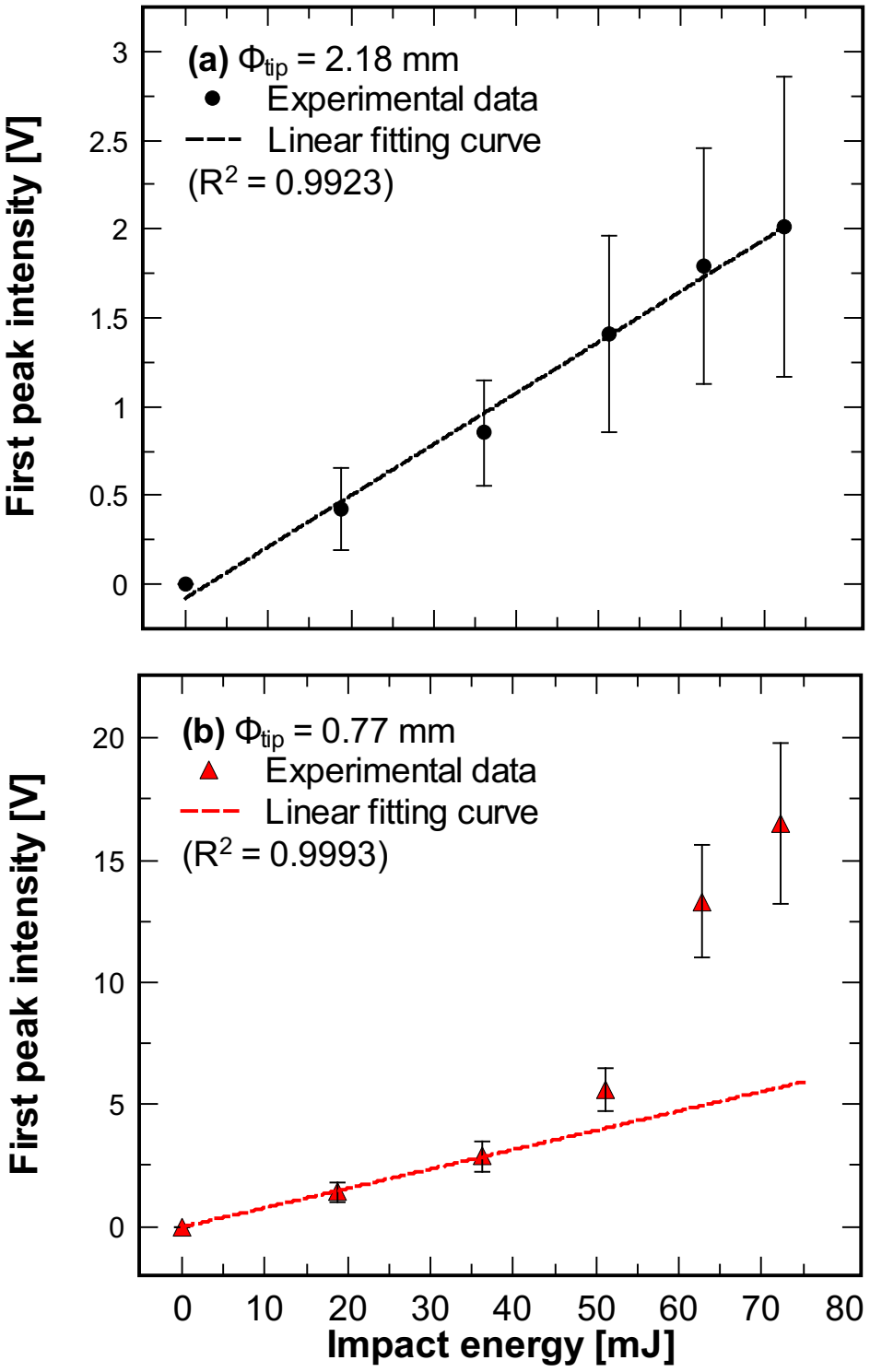

Figure 5.4: Peak intensity of ZnS:Mn at different impact energies measured from (a) large and (b) small tip diameter.

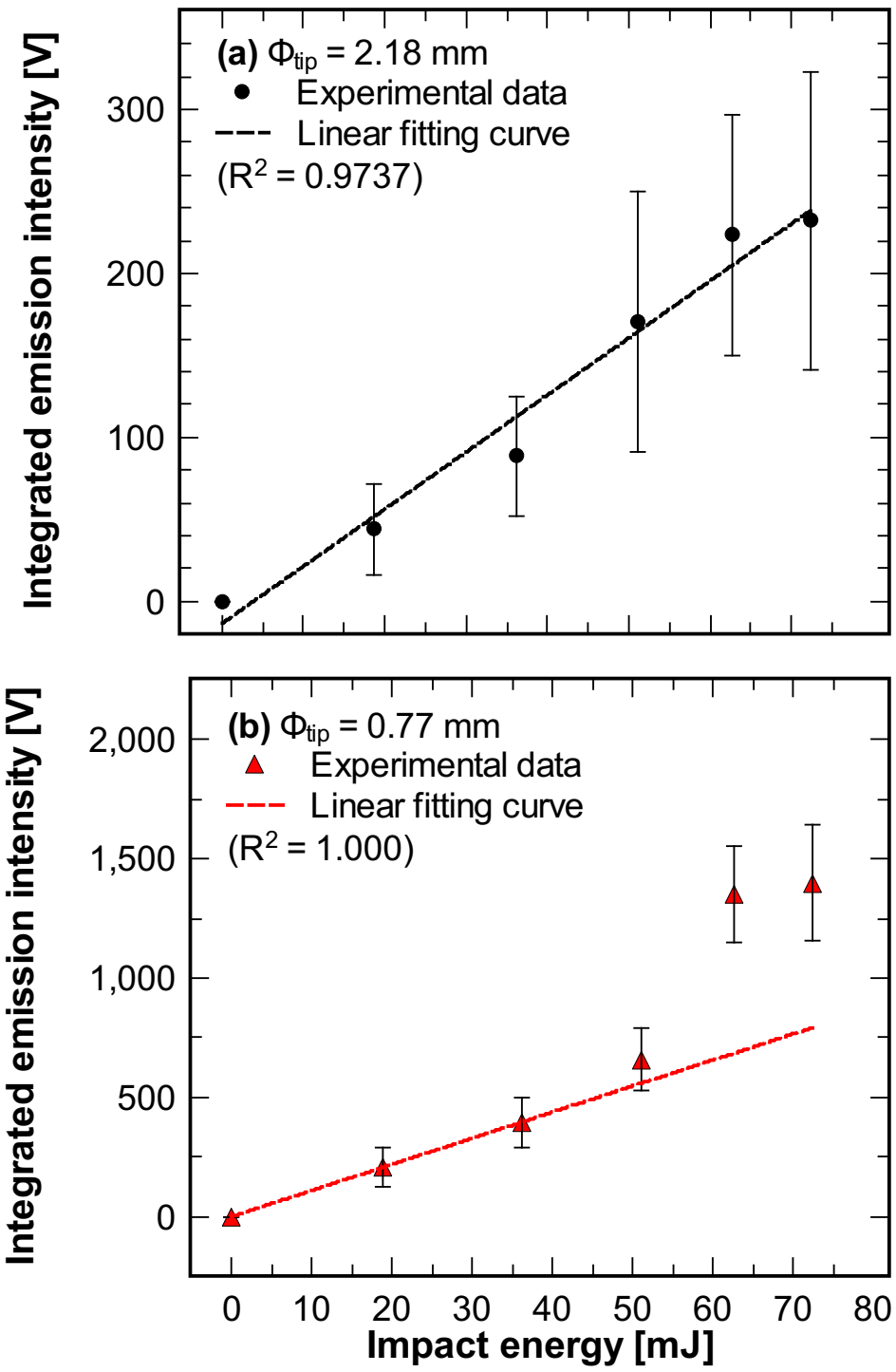

Figure 5.5: Total emission intensity of ZnS:Mn as a function of impact energies observed from (a) large and (b) small tip diameter. Fitting range is similar to that using in Fig. 5.4(b).

Chapter 6

Mechanism and its mathematical expressions of stress-induced luminescence of ZnS:Mn phosphors

6.1 The electromechanical coupling energy and its constitutive relations [1–3]

When the material is subjected to the external force, it will response to the action in sense of deformation. The mechanical stress σ_{ij} and strain ε_{ij} are the measurement of force per unit area and deformation of a deformable body, respectively. They are usually described as the second-rank tensor. The constitutive relation between stress and strain tensors can be established by generalized Hooke's law in tensor expression as Eq. 6.1,

$$\sigma_{ij} = c_{ijkl}\,\varepsilon_{kl} \text{ and } \varepsilon_{ij} = s_{ijkl}\,\sigma_{kl} \tag{6.1}$$

where c_{ijkl} is a forth-rank stiffness tensor whereas s_{ijkl} is called elastic compliance tensor.

Dielectric refers to the materials that are susceptible to the electric field. As non-zero charges are created, it results into a field-induced internal polarization. This behavior usually occurs in the materials containing polarity. In analogy to mechanical actions, it is possible to express such connections in terms of the response electric displacement **D** upon the applied field **E**, or vise versa, as shown in Eq. 6.2 where χ_0 is a space permittivity = 8.854×10^{-12} F m^{-1} and κ_{ij} is the electric susceptibility,

$$\mathbf{D}_i = \chi_0 (1 + \kappa_{ij}) \mathbf{E}_j = \chi_0 \chi_r \mathbf{E}_j = \chi_{ij} \mathbf{E}_j. \tag{6.2}$$

For certain types of dielectric crystals that do not contain centrosymmetricity, they can also produce internal polarization as the consequence of mechanical application. This phenomenon is known as piezoelectricity. Therefore, a total electric displacement of piezoelectric material is written as Eq. 6.3 where d_{ikl} is third-rank piezoelectric strain tensor,

$$\mathbf{D}_i = d_{ikl} \sigma_{kl} + \chi_{ij} \mathbf{E}_j. \tag{6.3}$$

Due to the non-centrosymmetricity of ZnS crystals, either of cubic or hexagonal modification, one should expect the piezoelectric response from the compound [4].

According to the principle of energy conservation and the first law of thermodynamics, an increment of the internal energy per unit volume of the closed system dU equals to a summation of the thermal energy δQ and total thermodynamic works δW. Importantly, an identical sign convention is employed on both terms, i.e. the energy in which added into the system is positive,

$$\mathrm{d}U \equiv \delta Q + \delta W. \tag{6.4}$$

If these proceeding assumptions are held: (i) an insignificant heat gain/loss, (ii) a pure elastic deformation and (iii) an absence of phase transformation, the system can be considered as *the reversibly adiabatic* where the entropy change dS is zero; $\delta Q \equiv TdS = 0$, hence, the external works will solely contribute to the increase of the internal energy of the system.

The change of the internal energy density is therefore a summation of the fundamental works done by the elastic deformation and the electrical field polarization,

$$\mathrm{d}U \approx \delta W = \sigma_{ij} \, \mathrm{d}\varepsilon_{ij} + \mathbf{E}_m \, \mathrm{d}\mathbf{D}_m. \tag{6.5}$$

By integrating the preceding expression, the total internal energy density being stored in

the infinitesimal volume is described as Eq. 6.6,

$$U = \frac{1}{2}\,\varepsilon_{ij}\,\sigma_{ij} + \frac{1}{2}\,\mathbf{E}_m\,\mathbf{D}_m. \tag{6.6}$$

Let us consider the mechanical strain ε_{ij} and the electric field $\mathbf{E}_m$ as independent variables. Hence, the definition and the exact differential of the thermodynamic potential called electric enthalpy H is given as Eq. 6.7a and Eq. 6.7b, respectively,

$$H = U - \mathbf{E}_m\,\mathbf{D}_m, \tag{6.7a}$$

$$\mathrm{d}H = \sigma_{ij}\,\mathrm{d}\varepsilon_{ij} - \mathbf{D}_m\,\mathrm{d}\mathbf{E}_m. \tag{6.7b}$$

A definition of the strain and the electric displacement as a partial derivative of H is obtainable as following where a superscript denotes a variable which being kept constant. It is noteworthy to state that $\partial\varepsilon_{ij}/\partial\varepsilon_{ji} = 0$ when i $\neq$ j,

$$\sigma_{ij}(\varepsilon_{ij},\mathbf{E}_m) = \left(\frac{\partial H}{\partial \varepsilon_{ij}}\right)^{E},\ \ \mathbf{D}_m(\varepsilon_{ij},\mathbf{E}_m) = -\left(\frac{\partial H}{\partial \mathbf{E}_m}\right)^{\varepsilon}. \tag{6.8}$$

Applying Eq. 6.3 and Eq. 6.7a into Eq. 6.6, one can derive the final form of the electric enthalpy density of which the electromechanical coupling effect is included [5]:

$$H = \frac{1}{2}\,c^{E}_{ijkl}\,\varepsilon_{ij}\,\varepsilon_{kl} - e_{nij}\,\varepsilon_{ij}\,\mathbf{E}_n - \frac{1}{2}\,\chi^{\varepsilon}_{nm}\,\mathbf{E}_n\,\mathbf{E}_m, \tag{6.9}$$

where e_{nij} is piezoelectric stress coefficients which are defined as $d_{nkl}\,c_{klij}$.

The linear constitutive equations of piezoelectric materials can be established from the definition of the stress and the electric displacement (Eq. 6.8) with Eq. 6.9.

$$\sigma_{ij} = c^{E}_{ijkl}\,\varepsilon_{kl}\ -\ e_{ijn}\,\mathbf{E}_n \tag{6.10a}$$

$$\mathbf{D}_m = e_{mkl}\,\varepsilon_{kl}\ +\ \chi^{\varepsilon}_{mn}\,\mathbf{E}_n. \tag{6.10b}$$

Explicit expressions of the coupling-associated internal energy density is therefore described in Eq. 6.11 where U_{El}, U_{Di} and U_{Cp} is the elastic, dielectric and piezoelectric energy

density namely,

$$\frac{1}{2}\,\sigma_{ij}\,\varepsilon_{ij} = \frac{1}{2}\,c^{E}_{ijkl}\,\varepsilon_{kl}\,\varepsilon_{ij} - \frac{1}{2}\,e_{ijn}\,\mathbf{E}_{n}\,\varepsilon_{ij} = U_{El} - U_{Cp}, \tag{6.11a}$$

$$\frac{1}{2}\,\mathbf{D}_{m}\,\mathbf{E}_{m} = \frac{1}{2}\,e_{mkl}\,\varepsilon_{kl}\,\mathbf{E}_{m} + \frac{1}{2}\,\chi^{\varepsilon}_{mn}\,\mathbf{E}_{n}\,\mathbf{E}_{m} = U_{Cp} + U_{Di}. \tag{6.11b}$$

According to IRE standard [2, 6], a piezoelectric coupling coefficient k^2 is defined as a ratio of the squared of interaction energy density and the product of stored elastic and dielectric energy densities. In spite of the fact that the coefficient is also considered as a ratio of the dissipated work to the supplied energy which is proposed by IEEE standard [5], those definitions refer to identical physical meaning as the ratio of applied energy in which be mutually transformed into another energy form;

$$k^2 = \frac{U^2_{Cp}}{U_{El}\,U_{Di}} = \frac{e^2_{ijn}}{c^{E}_{ijkl}\,\chi^{\varepsilon}_{mn}}. \tag{6.12}$$

Taking into account an equilibrium condition, a net force exerting on continuum body should be zero; $\tilde{\sigma}_{ij,j} + b_i = 0$ where $\tilde{\sigma}_{ij,j}$ is the applied mechanical force and b_i is called body force. The divergence of the electromechanical coupling stress (Eq. 6.10a) is therefore given as,

$$c^{E}_{ijkl}\,\varepsilon_{kl,j} - e_{ijn}\,\mathbf{E}_{n,j} = 0. \tag{6.13}$$

Equation 6.13 suggests that the force resulting from the coupling effect is the body force and its magnitude equals to that of pure mechanical deformation.

For a homogeneity of electric displacement inside the continuum, that is $\mathbf{D}_{m,m} = 0$,

$$e_{mkl}\,\varepsilon_{kl,m} + \chi^{\varepsilon}_{mn}\,\mathbf{E}_{n,m} = 0. \tag{6.14}$$

Inserting Eq. 6.12 and Eq. 6.14 into Eq. 6.13, it is possible to express the equilibrium state of the force inside the coupling interaction-associated continuum medium; the emerging body force $c^{E}_{ijkl}\,k^2\,\varepsilon_{kl,j}$ is recognized as the contribution of piezoelectricity and can also related to

the depolarizing-field effect [2]:

$$c^{E}_{ijkl}\,\varepsilon_{kl,j} + c^{E}_{ijkl}\,k^2\,\varepsilon_{kl,j} = 0. \tag{6.15}$$

The force field inside non-piezoelectric materials whose $k^2 = 0$ is therefore identical to that of externally applied stress whereas the additional force emerges corresponds to its piezoelectric properties.

For the case of zero electric field, an amount of coupling energy due to piezoelectric effect can be described as a function of the stress where $\beta_{nm} = \chi^{-1}_{nm}$. It should be noted that $\mathbf{E}_n$ in the equation is regarded as the deformation-induced electric field.

$$\begin{aligned} H^{pz} &= e_{nij}\,\varepsilon_{ij}\,\mathbf{E}_n \\ &= d_{nkl}\,\sigma_{ml}\,\mathbf{E}_n \\ &= d_{nkl}\,\sigma_{ml}\,\beta_{nm}\,\mathbf{D}_m \\ &= d_{nkl}\,\sigma_{ml}\,\beta_{nm}\,d_{mij}\,\sigma_{ij} \\ &= \beta_{nm}\,d_{mij}\,d_{nkl}\,\sigma_{ij}\,\sigma_{kl}. \end{aligned} \tag{6.16}$$

Constitutive equations of piezoelectric effect of hexagonal ZnS crystals, corresponding to P63M space group, are given as following,

$$\begin{bmatrix} \sigma_1 \\ \sigma_2 \\ \sigma_3 \\ \sigma_4 \\ \sigma_5 \\ \sigma_6 \\ \mathbf{D}_1 \\ \mathbf{D}_2 \\ \mathbf{D}_3 \end{bmatrix} = \begin{bmatrix} c_{11} & c_{12} & c_{13} & 0 & 0 & 0 & 0 & 0 & -e_{13} \\ c_{12} & c_{11} & c_{13} & 0 & 0 & 0 & 0 & 0 & -e_{13} \\ c_{13} & c_{13} & c_{33} & 0 & 0 & 0 & 0 & 0 & -e_{33} \\ 0 & 0 & 0 & c_{44} & 0 & 0 & 0 & -e_{15} & 0 \\ 0 & 0 & 0 & 0 & c_{44} & 0 & -e_{15} & 0 & 0 \\ 0 & 0 & 0 & 0 & 0 & c_{66} & 0 & 0 & 0 \\ 0 & 0 & 0 & 0 & e_{15} & 0 & \chi_{11} & 0 & 0 \\ 0 & 0 & 0 & e_{15} & 0 & 0 & 0 & \chi_{11} & 0 \\ e_{13} & e_{13} & e_{33} & 0 & 0 & 0 & 0 & 0 & \chi_{33} \end{bmatrix} \begin{bmatrix} \varepsilon_1 \\ \varepsilon_2 \\ \varepsilon_3 \\ \varepsilon_4 \\ \varepsilon_5 \\ \varepsilon_6 \\ \mathbf{E}_1 \\ \mathbf{E}_2 \\ \mathbf{E}_3 \end{bmatrix}$$

Let us consider an applied uniaxial stress exerting perpendicular to the basal plane of wurtzite ZnS phase, its corresponding enthalpy density can be expressed as the following equation. A crystallographic orientation distributing factor α is introduced for the case of polycrystalline sample. Validity of the presumption of uniaxial stress and the determination of distribution parameter will be further discussed in the proceeding chapter.

$$H^{pz} \approx \alpha\, \beta_{33}\, d_{33}^2\, \sigma_{33}^2. \tag{6.17}$$

Due to a polycrystallinity of ZnS phosphors as depicted by XRD diffraction patterns (see Fig. 3.1(b)), it is important to employ an approach to transform into a single crystal-orientation. According to the coordinate transformation using rhombohedral lattice system, a hexagonal structure can be converted into the corresponding cubic, and vise versa. The schematic of their relationship is illustrated in Fig. 6.1. Transformation matrices can be found in [7, 8].

Orthogonality of cubic structure allows subsequent vectorial operation and therefore an inner product of $\langle 111 \rangle$ and $\langle \mathrm{hkl} \rangle$ direction of corresponding cubic lattice can be performed to determine a spatial orientation of particular diffraction plane with respect to the basal plane of hexagonal structure. It is important to notify that there is no restriction that a calculated $\langle \mathrm{hkl} \rangle$ of corresponding cubic lattice have to follow the *selective rules* of reflection.

In order to take into consideration XRD intensity, an additional factor α is defined as following equation where $\bar{I}_i = \dfrac{I_i}{\sum I_i}$ is a relative intensity and ψ_i is an inner product of $\langle 111 \rangle$ and $\langle \mathrm{hkl} \rangle$ of i-th peak,

$$\alpha = \sum_i \bar{I}_i \psi_i. \tag{6.18}$$

According to the diffraction results being summarized in table 6.1, α equals to 0.3574 in this study.

Table 6.1: Corresponding value of required parameter for α determination.

(hkl)-Hexagonal	(hkl)-Cubic	$\bar{I}_i$ (a.u.)	ψ_i	$\bar{I}_i\psi_i$
w(100)	c($\bar{2}$ 1 1)	0.318	0.000	0.000
w(002)	c(1 1 1)	0.203	1.000	0.203
w(101)	c($\bar{1}$ 1 1)	0.186	0.333	0.062
w(102)	c($\bar{1}$ 2 2)	0.040	0.577	0.023
w(110)	c($\bar{1}$ 0 1)	0.102	0.000	0.000
w(103)	c($\bar{1}$ 5 5)	0.052	0.728	0.038
w(200)	c($\bar{2}$ 1 1)	0.0107	0.000	0.000
w(112)	c($\bar{2}$ 1 4)	0.0623	0.378	0.024
w(201)	c($\bar{7}$ 5 5)	0.0138	0.174	0.0024
w(203)	c($\bar{5}$ 7 7)	0.0124	0.469	0.0058
			$\alpha =$	0.3574

6.2 Contribution of deformation to the electrical properties of semiconductors

An influence of deformation on electrical characteristics of semiconductors has been investigated for decades. An increase of anisotropic DC conductivity of plastically deformed CdS and ZnS single crystals was observed along with the reduction of the optical transmittivity spectra near absorption edge. The conductivity increased with the degree of deformation, but decreased with higher temperature. The phenomenon is interpreted as the result of dislocations that may introduce energy levels, e.g. acceptor sites, within the band gap [9, 10].

The behavior is also observed in other types of systems such as TiN [11], n-GaN [12, 13], GaAs [14], multilayered GaN-AlN-GaN [15, 16], heterostructure of $Al_xGa_{1-x}N$/GaN [17] or ZnO nanowires [18, 19], leading to the application of strain sensors or strain-effect transistors.

The theoretical model used for explaining a change of resistivity of elastically deformed semiconductors is Shockley theory that considers the flow of carrier at p-n junction. For an

ideal Schottky diode, the thermionic emission current I is given as,

$$I = SA^*T^2 \exp\left(-\frac{q\phi_B}{\eta kT}\right)\left[\exp\left(\frac{qV}{\eta kT}\right) - 1\right] \tag{6.19}$$

where S, ϕ_B, A^* and η are the effective Richardson constant, the Schottky barrier height (SBH), the area of Schottky diode and the ideality factor in which is close to a unity, respectively. An influence of stress on SBH was illustrated by a linear relationship between the logarithm of current and the applied stress [14].

Considering n-type semiconductor connected to metallic electrode, a partial neutralization of piezoelectric polarization charges at the interface may result into the shift of Fermi level and consequently the change in Schottky barrier height. Of course, the polarity of polarization also plays an important role in controlling the resistivity of the crystal, that is the negatively surface charges will result in a reduction of the barrier height.

Although the modified Shockley theory and the proposed mechanism share a mutual concept of the shift of Fermi level of the semiconductor, the main differences are likely to be (i) the considering circuitry or electrical boundary and (ii) the localization of Fermi level change.

In other words, the polarized surface charges due to piezoelectricity are recognized as an additional built-in electric field and consequently increase *the electrostatic potential energy* of carriers at the interface for a close-circuit situation whereas our proposed model is considering the contribution of *stored piezoelectrical energy* caused by the deformation in an open-circuit connection.

6.3 Excitation process of stress-induced luminescence

Unlike photoluminescence that required an excitation photon with energy greater or equals to the bandgap of luminophors, among of three possible mechanisms for electroluminescence of doped ZnS, the so-called Poole-Frenkel emission refers an injection of electrons from their traps under the electric field of 10^8 V m^{-1} [20].

As mentioned in the first chapter, *B.P. Chandra et. al* suggested a reduction of electron trap depths is caused by localized high piezoelectric constant. The concept of trap ionization

was referenced to [21]. The cited article written by *I. Chudáček* however mentioned that a pressure-induced electric field strength of $\approx 10^6$ V m^{-1} is not sufficient to cause **a direct ionization of the recombination centers.** Therefore, the local electric field enhancement caused by lattice distortion should be responsible for such excitation and produce triboluminescence. The estimated field strength was about 10^8 V m^{-1} at the applied pressure of about 1 GPa.

A number of researches about the effect of mechanical deformation on to the trap depth of doped ZnS is quite limited. By using thermoluminescence measurement, *J.W. Hook III and H.G. Drickamer* [22] reported that the activation energy of high temperature green glow peak increases with higher applied pressure. The emission is assigned to a recombination of Cl^--associated traps that locate below the conduction band and Zn vacancies. The authors therefore postulated a similarity of trap depths and the energy difference of donor states and conduction band minimum. Pressure-dependent trap depth was observed in the literature [23, 24].

Despite of a consistency in the required field to cause an emission, it thus lacks of scientific evidence to support the possibility of trap reduction by piezoelectric field.

Associated piezoelectric enthalpy generated from a spherical crystallite with diameter of d can be approximated by Eq. 6.20,

$$H_{total}^{pz} = \left(\beta_{33}\, d_{33}^2\, \sigma_{33}^2\right) \left(\frac{1}{6}\, \pi\, d^3\right). \tag{6.20}$$

Considering the extreme scenario where the energy produced inside a 60-nm crystallite is entirely transferred to a single electron. Also, the applied uniaxial stress of 100 MPa is assumed to perfectly exert along c-axis. It turns out to be about 1.97×10^{-19} J, that is 1.23 eV. Direct excitation are not able to take place as the value is considerably smaller than the bandgap of ZnS.

On the other hand, the estimated energy is significantly close to shallow donor trap depth in which reported as 0.2–0.4 eV [23, 24]. This signifies that an excitation is likely to be the consequence of high energetic electrons deliberated from electron traps near the conduction band edge and a piezoelectric enthalpy is responsible for stimulation of electrons.

6.4 Determination of carrier population in semiconductors

Let us assume a homogeneous energy distribution and zero temperature gradient, inside an infinitesimal unit volume with the electromechanical coupling energy H^{pz}, it constitutes of n electrons whose thermal energy equals kT. Therefore, a probability of finding the energy level E_i being occupied is governed by Fermi-Dirac distribution, as expressed in Eq. 6.21 where E_f is called chemical potential or Fermi level, k is Boltzmann's constant (1.381×10^{-23} J K^{-1}) and T is a temperature. Noting that E_f gives F(E_i) = 0.5 at temperature of 0 K,

$$\mathrm{F}(E_i) = \frac{1}{1+\exp\left(\frac{E_i - E_f}{kT}\right)}. \tag{6.21}$$

Taking a negligible thermal energy into account, that is $E_i - E_f \gg kT$, the distribution function is simplified as,

$$\mathrm{F}(E_i) \approx \exp\left(-\frac{E_i - E_f}{kT}\right). \tag{6.22}$$

Net population of electrons occupying in conduction band where its minimum edge is E_c can be approximated by Eq. 6.23,

$$\begin{aligned} n_0 &\equiv \int_{E_c}^{\infty} F(E_i)\, g(E_i)\, \mathrm{d}E \\ &\approx N_c \exp\left(-\frac{E_c - E_f}{kT}\right). \end{aligned} \tag{6.23}$$

where g(E_i) is a density of state of the level E_i that equals $\frac{1}{2\pi^2}\left(\frac{2m_e}{\hbar^2}\right)^{3/2}\sqrt{E_i - E_c}$ for bulk material, $\mathrm{N}_c = 2\left(\frac{m_e kT}{2\pi\hbar^2}\right)^{3/2}$, m_e is an effective mass of electron and $\hbar = h/2\pi$ is reduced Planck constant.

A change in number of free electrons population in the perturbed system with Fermi level of $E_f + \phi$ can be estimated from the following equation,

$$\Delta n_0 = n_0 \left[\exp\left(\frac{\phi}{kT}\right) - 1\right]. \tag{6.24}$$

According to a definition of chemical potential as the partial derivative of thermodynamic

potential with respect to the mass of constituents in the adiabatic closed system [25, 26], a piezoelectric-associated enthalpy density can be regarded as an effective energy distributed to the infinitesimal domain containing a charged particle and responsible for the shift of Fermi level caused by deformation. The model is very analogous to an explanation for the improvement of electrical conductivity in n-type doped semiconducting materials.

The increase of energetic electrons are suggested to be accounted for the shift of Fermi level rather than their kinetic energy, i.e. a change in kT, in which might be portrayed by *hot electrons* [20]. This is mainly due to a lack of appropriate approach to estimate the amount of energy being given to individual electrons.

6.5 Contribution of piezoelectric enthalpy to light emission: A proposal of alternative mechanism of triboluminescence

Population of free electrons in conduction band of host crystals increases by deformation. Hence, the change of electrons concentration can be expressed as Eq. 6.25 by considering that the shift of Fermi level is proportional to the electrical enthalpy, i.e. $\phi = \gamma H^{pz}$,

$$\Delta n^* = n_0 \left[\exp\left(\frac{\gamma\, \alpha\, \beta_{33}\, d_{33}^2}{kT}\, \sigma_{33}^2 \right) - 1 \right]. \tag{6.25}$$

where γ is an energy-transferring coefficient and n_0 is an electron concentration of the stress-free ZnS crystals being reported as about 1×10^{15} cm^{-3} at room temperature [27, 28].

On the assumption of homogeneous energy distribution, an increase of electrons inside domain Ω containing phosphors at fraction of v_f can be approximated by,

$$N_e \approx v_f \cdot \Omega \cdot n_0 \left[\exp\left(\frac{\gamma\, \alpha\, \beta_{33}\, d_{33}^2}{kT}\, \sigma_{33}^2 \right) - 1 \right]. \tag{6.26}$$

For a recombination process of excited electrons and holes taken place at the luminescence

centers produces photon with an efficiency of η,

$$\begin{aligned} N_{pht} &= \eta \cdot N_e \\ &= \eta \cdot v_f \cdot \Omega \cdot n_0 \left[\exp\left(\frac{\gamma\, \alpha\, \beta_{33}\, d_{33}^2}{kT}\, \sigma_{33}^2 \right) - 1 \right]. \end{aligned} \tag{6.27}$$

Final expression for PMT output signal in which relating to TrL intensity and the sliding shear stress can be achieved by inserting Eq. 6.27 into Eq. 2.14,

$$\begin{aligned} \bar{V}_{pmt} &= LS \cdot k_{\mathrm{m}} \cdot \bar{E} \cdot \frac{1}{\Delta t} \cdot \eta \cdot v_f \cdot \Omega \cdot n_0 \left[\exp\left(\frac{\gamma\, \alpha\, \beta_{33}\, d_{33}^2}{kT}\, \sigma_{33}^2 \right) - 1 \right] \\ &\Downarrow \\ y(x) &= A \left[\exp\left(Bx^2 \right) - 1 \right]. \end{aligned} \tag{6.28}$$

Due to the first-degree approximation of $\exp(x)$ is $x+1$, the formulation is reduced to $y \approx Cx^2$ for the case that the applied stress is low. This is similar to a correlation of the total intensity and the applied pressure proposed by *B.P. Chandra et. al* [29–33].

6.6 Summaries

Alternative mechanism for triboluminescence of ZnS:Mn phosphors with the mathematical expression of the emission intensity and the stress which including the contribution of volume fraction and multiple crystallographic orientation of ZnS crystals are fully developed based on a perspective of the electromechanical coupling energy. The process of triboluminescence are as the following where its schematic is shown in Fig. 6.3,

1. As doped ZnS phosphors are subjected to the deformation, a piezoelectricity-associated enthalpy is produced.

2. Due to an energy conservation, the electric enthalpy contributes to an increase of stored potential energy of electrons.

3. Detrapping of electrons from shallow traps takes place so that the concentration of free electrons in conduction band increases.

4. Holes will be captured by the luminescent centers while the excited electrons tend to return its lower energy state.
   $(Mn^{2+}) + \oplus \rightarrow (Mn^{3+})^*$

5. The excited electrons recombine with holes captured in the centers.
   $(Mn^{3+})^* + e^- \rightarrow (Mn^{2+})^*$

6. The emission of photon is an attribution of de-excitaion of the centers.
   $(Mn^{2+})^* \rightarrow (Mn^{2+}) + h\nu$.

The total emission intensity is found to be non-linearly increased with the applied stress as expressed by $A\left[\exp\left(Bx^2\right) - 1\right]$ where a pre-exponential A contains characteristic parameters of the photodetectors and the composite as well as an efficiency of photon conversion of luminescent centers whereas a piezoelectric response of ZnS crystals is described in B-factor. Its approximation is a simple quadratic relationship for low applied stress.

Reference

[1] Mason, W. *Piezoelectric Crystals and Their Applications to Ultrasonics*. Van Nostrand, (1949).

[2] Ikeda, T. *Fundamentals of Piezoelectricity*. Oxford University Press, (1990).

[3] Ballas, R. *Piezoelectric Multilayer Beam Bending Actuators - Static and Dynamic Behavior and Aspects of Sensor Integration*. Springer Berlin Heidelberg, (2007).

[4] Burns, G. *Solid State Physics*. Academic Press, Inc., (1985).

[5] *ANSI/IEEE Std 176-1987, IEEE Standard on Piezoelectricity* (1988).

[6] *Proceedings of the IRE* **46**(4), 764–778 (1958).

[7] O'Keefe, M. and Hyde, B. *Crystal Structures, No. 1: Patterns & Symmetry*. Mineralogical Society of American, (1996).

[8] Müller, U. *Symmetry Relationships between Crystal Structures – Applications of Crystallographic Group Theory in Crystal Chemistry*. Oxford University Press, (2013).

[9] Merchant, P. and Elbaum, C. *Solid State Commun.* **20**(8), 775–778 (1976).

[10] Merchant, P. and Elbaum, C. *Solid State Commun.* **26**(2), 73–75 (1978).

[11] Yang, X., Chu, M., Huang, A., and Thompson, S. *Solid-State Electron.* **79**, 142–146 (2013).

[12] Liu, Y., Kauzer, M., Nathan, M. I., Ruden, P., Dogan, S., Morkoç, H., Park, S., and Lee, K. *Appl. Phys. Lett.* **84**(12), 2112–2114 (2004).

[13] Bykhovski, A., Kaminski, V., Shur, M., Chen, Q., and Khan, M. *Appl. Phys. Lett.* **68**(6), 818–819 (1996).

[14] Chung, K., Wang, Z., Costa, J., Williamson, F., Ruden, P., and Nathan, M. *Appl. Phys. Lett.* **59**(10), 1191–1193 (1991).

[15] Bykhovski, A., Gelmont, B., and Shur, M. *J. Appl. Phys.* **74**(11), 6734–6739 (1993).

[16] Gaska, R., Yang, J., Bykhovski, A., Shur, M., Kaminski, V., and Soloviov, S. *Appl. Phys. Lett.* **71**(26), 3817–3819 (1997).

[17] Eickhoff, M., Ambacher, O., Krötz, G., and Stutzmann, M. *J. Appl. Phys.* **90**(7), 3383–3386 (2001).

[18] Zhou, J., Gu, Y., Fei, P., Mai, W., Gao, Y., Yang, R., Bao, G., and Wang, Z. *Nano Lett.* **8**(9), 3035–3040 (2008).

[19] Zhu, R. and Yang, R. *Nanotechnology* **25**(34), 1–6 (2014).

[20] Yen, W., Shionoya, S., and Yamamoto, H. *Fundamentals of Phosphors*. CRC Press, (2007).

[21] Chudáček, I. *Czech. J. Phys. B* **16**(6), 520–524 (1966).

[22] Hook III, J. and Drickamer, H. *J. Appl. Phys.* **49**, 2503–2507 (1978).

[23] House, G. and Drickamer, H. *J. Chem. Phys.* **67**, 3221–3226 (1977).

[24] Lang, J., Dreger, Z., and Drickamer, H. *J. Appl. Phys.* **71**, 1914–1918 (1992).

[25] Ragone, D. *Thermodynamics of Materials, Volume 1*. John Wiley & Sons, Inc., (1994).

[26] Gaskell, D. *Introduction to the Thermodynamics of Materials*. CRC Press, (2003).

[27] Gordon, N. and Allen, J. *Solid State Commun.* **37**, 441–443 (1981).

[28] Jeon, S., Bang, S., Lee, S., Kwon, S., Jeong, W., Jeon, H., H.J.Chang, and Park, H.-H. *J. Korean Phys. Soc.* **53**(6), 3287–3295 (2008).

[29] Chandra, B., Baghe, R., and Chandra, V. *Chalcogenide Letters* **7**(1), 1–9 (2010).

[30] Chandra, V. and Chandra, B. *Opt. Mater.* **34**, 194–200 (2011).

[31] Chandra, B. *The Open Nanoscience Journal* **5**, 45–58 (2011).

[32] Chandra, B. *Int. J. Lumin. Appl.* **2**(3), 44–72 (2012).

[33] Tiwari, R., Dubey, V., and Chandra, B. *Mater. Phys. Mech.* **19**, 25–38 (2014).

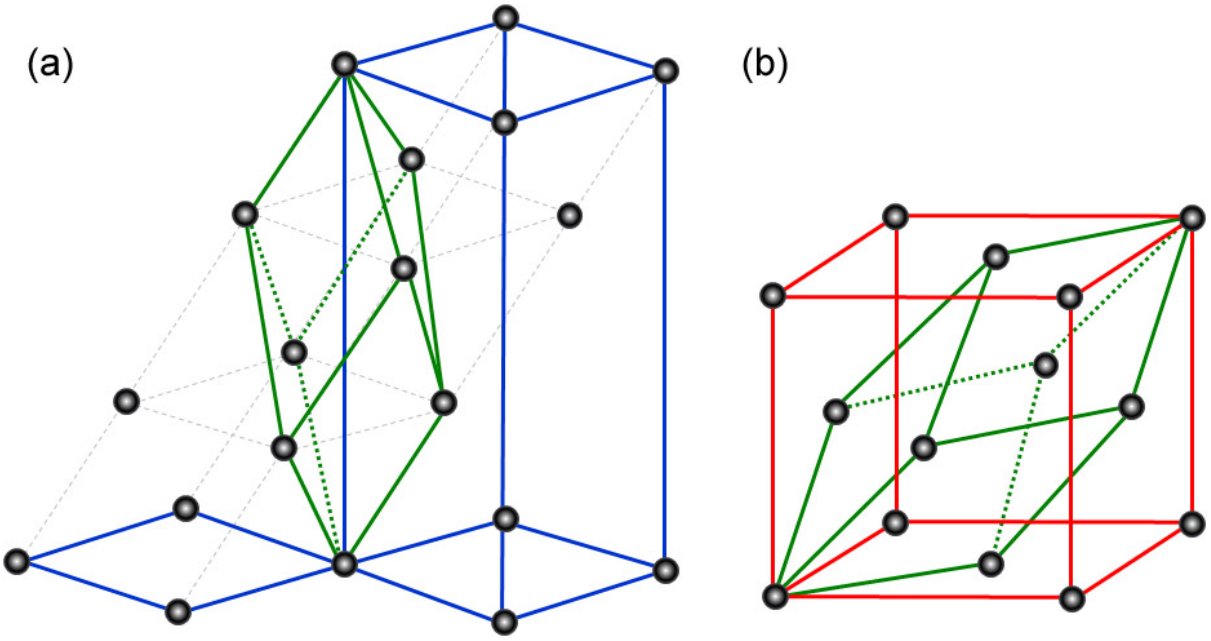

Figure 6.1: Hexagonal (blue) and cubic (red) structures mutually share a rhombohedral cell (green). Diagonal of the mutual lattice corresponds to a close packing direction of either hexagonal or cubic, that is $\langle 0002 \rangle$ and $\langle 111 \rangle$, respectively.

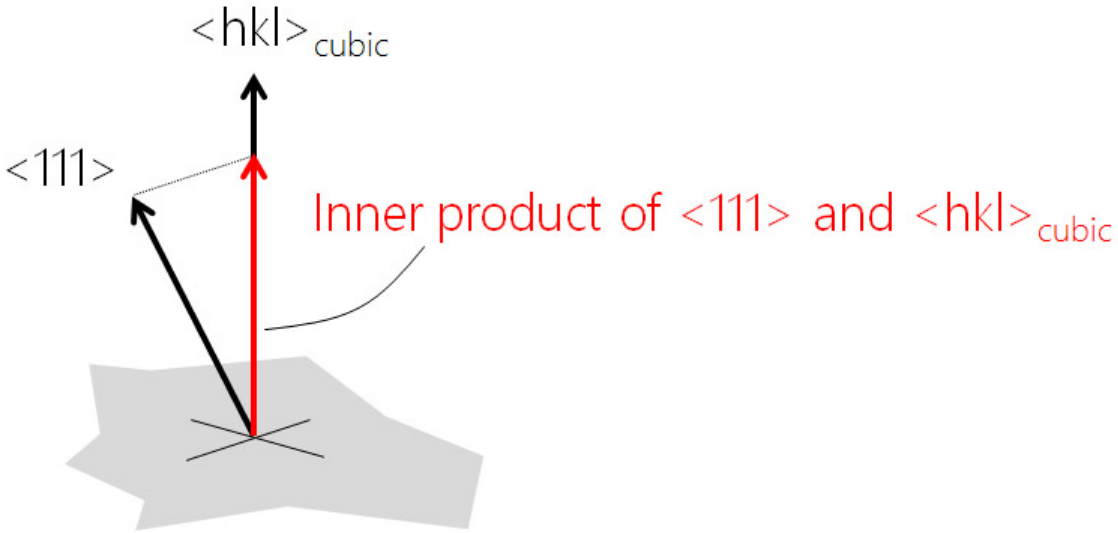

Figure 6.2: Orthogonality of cubic lattice allows us to determine a component of close-packed direction from any given direction.

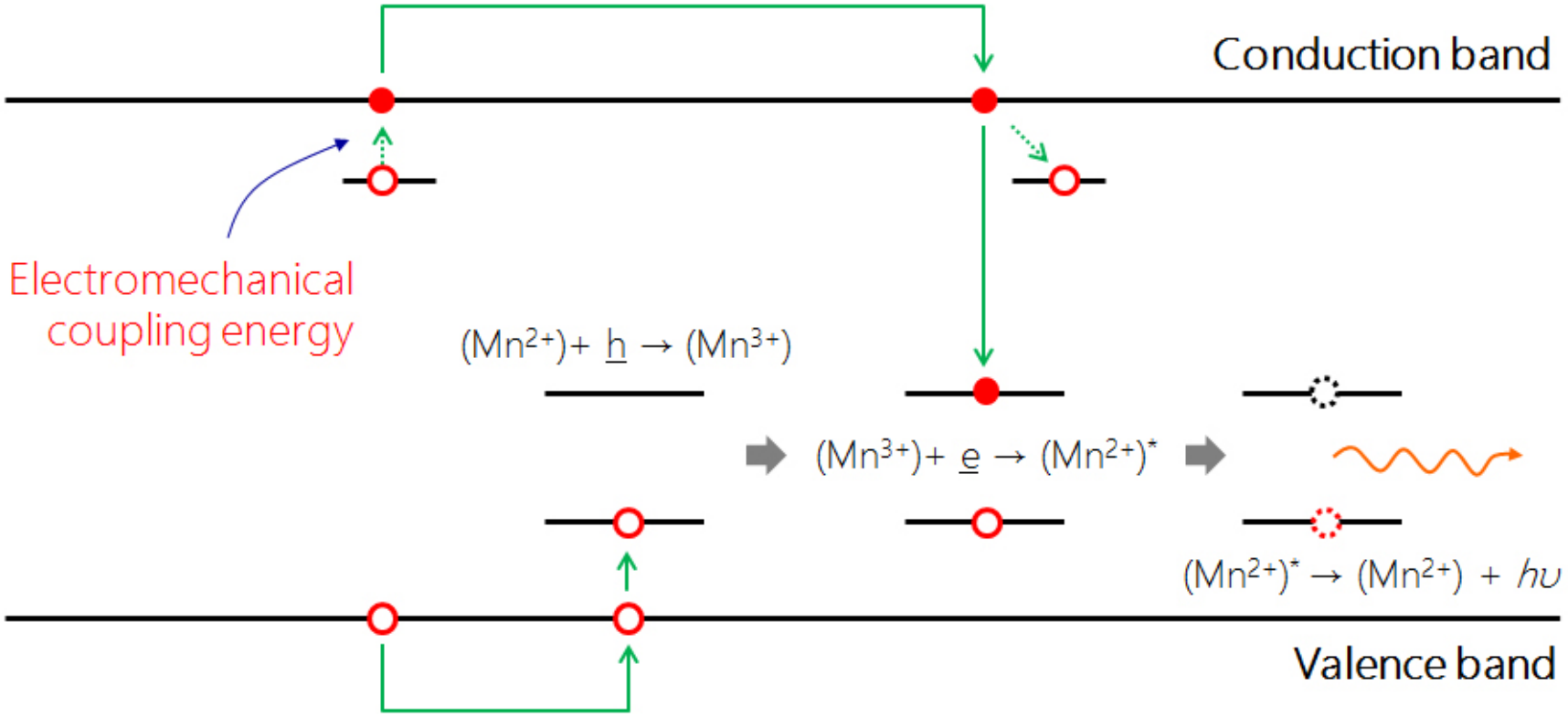

Figure 6.3: Schematic of the proposed mechanism of triboluminescence behavior as a consequence of piezoelectric coupling energy.

Chapter 7

Applicability of the proposed mechanism and discussions

Despite of an excellent experimental results indicating the importance of contact geometry on mechanoluminescence of ZnS crystals, it is unfortunate to conduct further analysis since there is no appropriate approach to determine a magnitude of exerting force during impact. Therefore, this chapter mainly focuses on the results from sliding deformation experiment (Chapter 4)

7.1 Reiteration of the proposed mechanism of triboluminescence of ZnS:Mn

It is well demonstrated that a deformation-induced emission is rather relating to applied stress. To calculate the stress exerting in particulate composite and contact geometries, young modulus is required to be firstly determined for given volumetric concentration of phosphors as well as Poisson ratio. As the stiffness increases by addition of particles, a contacting radius reduces and consequently results into higher maximum Hertzian contact pressure. Equivalent stress, so-called von Mises stress, along loading axis can be an approximation of the apparent stress as friction coefficient is provided. By the assumption of symmetry and homogeneity of stress distribution within a hemispherical domain whose diameter equals to the contact radius, it is therefore possible to consider the determined equivalent stress as exerting uniaxial stress due to a geometry of sliding contact.

Deformation of non-centrosymmetric ZnS:Mn crystals results into a generation of an electrical enthalpy so that the internal energy increases. According to a thermodynamic definition

of Fermi level as the partial derivative of the enthalpy with respect to the mass of constituents, it is possible to regard those electromechanical coupling energy as a shift of Fermi level. A change of electron concentration in conduction band can be approximated from Fermi-Dirac distribution function.

Recombination of excited electrons and holes takes place at energy levels produced by doping Mn^{2+} ions, resulting in a characteristic yellow emission. Taking into account the efficiency of luminescence centers, a number of emitted photons should be proportional to a total number of excited electrons. With all information of emission spectrum of ZnS:Mn, deformation time and a control voltage on photomultiplier tube, a signal of the detector is able to determine a number of photonic emission.

7.2 Interpretation of factors and coefficients associating in the model

Luminous sensitivity, LS This is a conversion factor of the photomultiplier tube. Electrons produced by photoelectric effect are multiplied by dynode stages in which connected to positive voltage. A multiplication factor (also known as the gain of detector) is manipulated by controlling voltage supplied into a terminal of the tube as illustrated in Fig. 7.1 [1]. According to the certificate of performance issued by the manufacturer (Fig. 7.2), the sensitivity at controlling voltage of 1.0 volts is 3.17×10^8 V lm^{-1}. To avoid higher background noise, a low controlling voltage of 0.6 volts was used which yields corresponding luminous sensitivity of $3.17 \times 10^8 \times \frac{2.519 \times 10^4}{2.139 \times 10^6} = 3.73 \times 10^6$ V lm^{-1}.

Maximum sensitivity of human eyes, k_m The parameter equals to 683 lm W^{-1} which is related to a conversion coefficient from the radiant quantity to the luminous one standardized by International Commission on Illumination (CIE) in 1931 [2]. It has a physical meaning of a luminous power which is equivalent to a unity radiance power emitted from a monochromatic emission at $\lambda = 555$ nm.

Effective photonic energy, $\bar{E}$ This term represents an effective energy possessed by a single photon emitted from a non-monochromatic radiation. As mentioned in section 2.3.1, It is defined as an integration of a product of two Gaussian functions, depicted in Fig. 2.11, and subjected to be changed with different emission spectra. The constant is numerically calculated as 0.308 eV per photon for the characteristic emission of ZnS:Mn phosphors.

Time period, Δt This denotes a deformation time which can be calculated from a rotational speed so that $\Delta t = \frac{60}{RPM}$ for one rotation.

Electron-photon conversion coefficient, η The coefficient illustrates an conversion efficiency of Mn^{2+} centers, that is its quantum efficiency.

Volume fraction of the phosphor, v_f A direct contribution of volume fraction on emission behavior is indicated by the parameter. Linear relationship between PMT voltage and the fraction has been reported by *S. Someya et. al* [3, 4].

Deformation volume, Ω It equals to $\pi^2 R r^2$ where R and r corresponds to a radius of wear track and that of contacting region, respectively. The parameter is rather variable since the contact radius is a function of applied load and mechanical properties of the assembled bodies.

Stress-free electron concentration, n_0 A carrier concentration of annealed ZnS deposited film is reported to be about 1×10^{15} cm^{-3} at room temperature [5, 6].

Energy transferring factor, γ The coefficient is suggested to be the characteristic constant of the material indicating a comparative efficiency of changing in Fermi level by external stimulations.

Crystallographic orientation distribution factor, α This coefficient is introduced for eliminating the effect of polycrystallinity of phosphors. As discussed in the preceding chapters, the applied stress and the piezoelectric polarization are considered to occur perpendicular to

the basal plane of wurtzite phase. This parameter is a summation of the weighted (111)-components. In this study, a value of α is calculated to be 0.3574.

7.3 Determination of energy transferring factor and photon conversion efficiency

Defining two new variables V^* and B:

$$V^* = \frac{\bar{V}_{pmt}}{(LS \cdot k_{\mathrm{m}} \cdot \bar{E}) \cdot \left(v_f \cdot \Omega \cdot \frac{1}{\Delta t}\right) \cdot n_0}, \tag{7.1}$$

$$B = \gamma \cdot \frac{\alpha\, \beta_{33}\, d_{33}^2}{kT} \cdot 10^{-12}. \tag{7.2}$$

where 10^{-12} is required for units consistency since the stress is expressed in scale of *MPa*.

Rearrangement of Eq. 2.12 yields,

$$\ln\left(\frac{V^*}{\eta} - 1\right) = B\sigma_{eqv}^2. \tag{7.3}$$

To satisfy boundary conditions, a value of η should be less than a unity and produces a linear fitting curve between $\ln\left(\frac{V^*}{\eta} - 1\right)$ and σ_{eqv}^2 with y-intercept at zero whereas a slope of the plot can be used for determination of energy transferring factor. As shown in Fig. 7.3, the most satisfactory η is found as 0.2396 whereas the transferring coefficient is calculated to be as 0.3332 at room temperature. Values of β_{nm} and d_{ij} of wurtzite ZnS can be found from table 1.1.

Although the Fermi level shift due to piezoelectric-associated energy is theoretically reasonable and experimentally proven as aforementioned, there is no reported parameter which allows us for comparing with the determined transferring coefficient γ. On the other hand, an electron-photon conversion efficiency η is interestingly in good agreement with reported internal quantum efficiency of ZnS:Mn nanocrystals with an average size of 30 Å at 18% [7]. This also emphasizes an applicability of the theoretical model proposed to be useful for determination of luminescence characteristic of piezoelectric phosphors.

7.4 Summaries

It has been demonstrated that the proposed mechanism of triboluminescence of ZnS:Mn as the result of electromechanical coupling energy shows an excellent applicability in broad deformation conditions. Main advantages of the models compared to other proposed mechanism are (i) all constants and parameters appearing in the expressions are calculable with conceptualized physical meaning and (ii) the influence of volume fraction of phosphors and multiple crystallographic orientation have been taken into consideration. On the other hands, a major disadvantage of the theory is its relatively complex than others. Electron-photon conversion factor determined from the model is found to comparable with the reported internal quantum efficiency of Mn^{2+} centers.

Reference

[1] Hamamatsu Photonics. *Metal Package PMT - Photosensor Module H10723 series*. Japanese version.

[2] International Committee on Illumination. `http://www.cie.co.at/index.php/LEFTMENUE/index.php?i_ca_id=298`. Online; accessed October, 2014.

[3] Someya, S., Ishii, K., Saeki, M., and Munakata, T. *Opt. Lett.* **38**(7), 1095–1097 (2013).

[4] Ishii, K., Someya, S., Saeki, M., and Munakata, T. *T. Jpn. Soc. Mech. Eng. C* **79**(806), 3721–3731 (2013).

[5] Gordon, N. and Allen, J. *Solid State Commun.* **37**, 441–443 (1981).

[6] Jeon, S., Bang, S., Lee, S., Kwon, S., Jeong, W., Jeon, H., H.J.Chang, and Park, H.-H. *J. Korean Phys. Soc.* **53**(6), 3287–3295 (2008).

[7] Bhargava, R., Gallagher, D., Hong, X., and Nurmikko, A. *Phys. Rev. Lett.* **72**, 1–4 (1994).

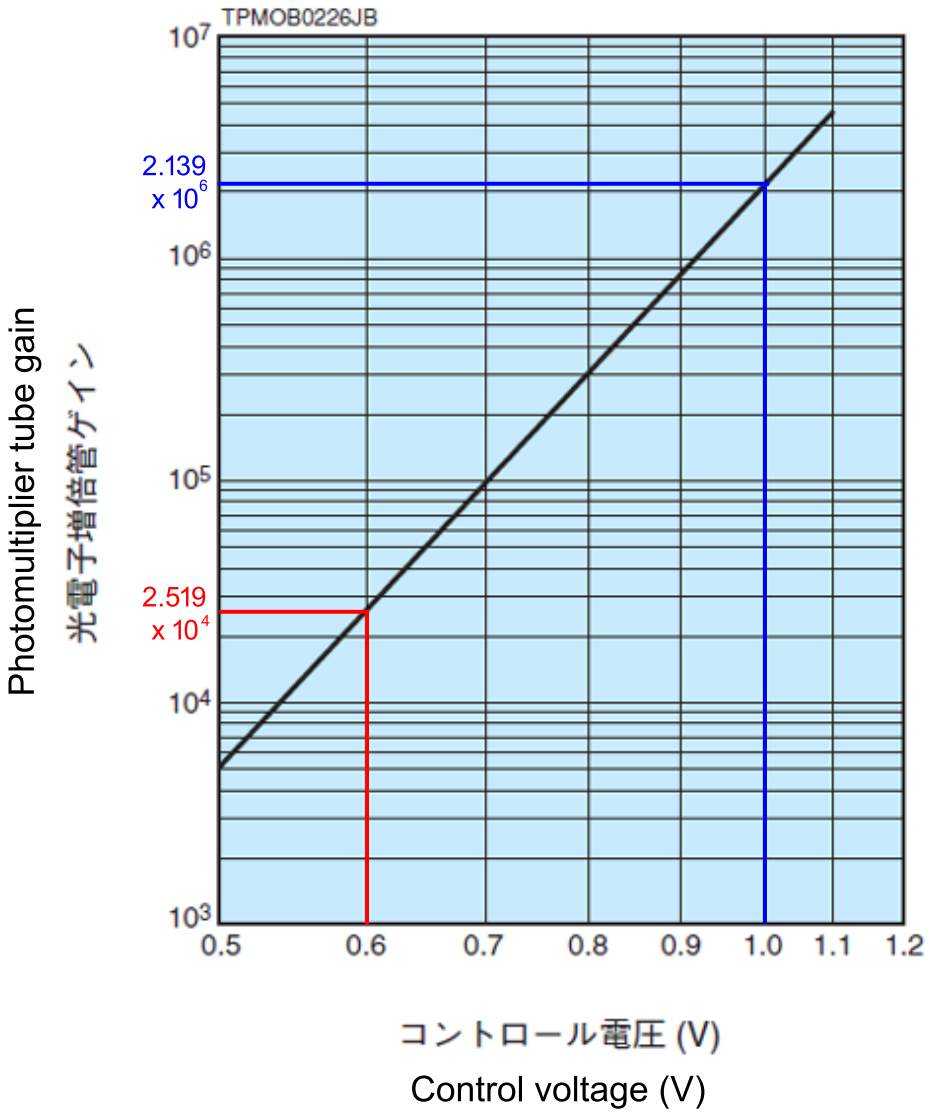

Figure 7.1: PMT gain as a function of control voltage. The red line represents a gain obtaining at a controlling voltage of 0.60 volts whereas the value of 1.0 volts corresponding to the reference value is illustrated in blue. (Reprinted from [1])

試 験 成 績 表

JNO. 279766
PAGE 1 OF 1

2014年 4月 9日

東京工業大学 大岡山キャンパス 御中

光 センサモジュール : H10723-20

御注文番号 (SD02014-00224323)

数 量 1

浜松ホトニクス株式会社
電子管事業部
〒438-0193 静岡県磐田市下神増 314 番地の 5
TEL (0539) 62-5245
FAX (0539) 62-2205

NOTES	(1) (2) (3) 光源 : 2856 K標準タングステンランプ (2) 使用フィルタ : 東芝 R-68 (3) コントロール電圧 : +1.0 V						
Serial Number	(1) 陰極感度 (Sk) μA/lm	(2) 陰極 赤感度比 (R/W) $x10^{-3}$	(3) 出力感度 (Sp) $x10^{5}$ V/lm	(4) 出力 オフセット 電圧 (Vos) mV			
39970005	481.0	449.0	3170.0	−1.1			

HAMAMATSU

検査印 森

Figure 7.2: A certificate of H10723-20 PMT performance issued by Hamamatsu Photonics.

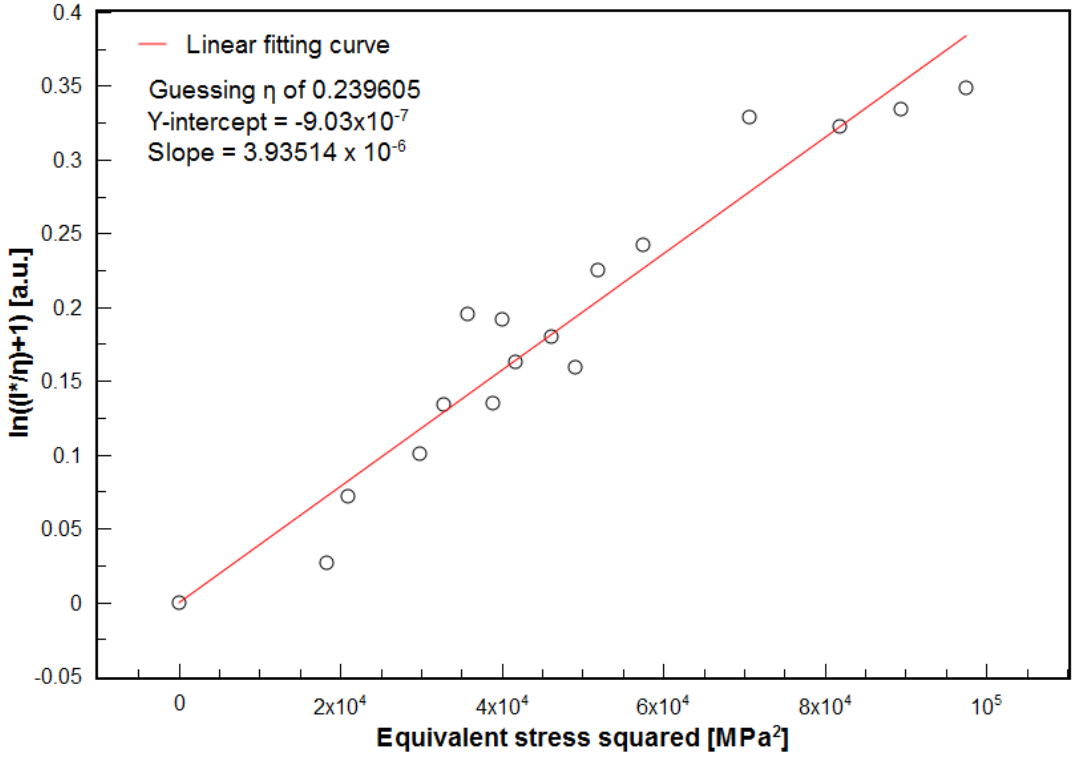

Figure 7.3: Comparative plot between $\ln\left(\frac{V^*}{\eta}-1\right)$ and σ^2_{eqv} using for determination of electron-photon conversion factor and energy transferring coefficient.

Chapter 8

Conclusions

Triboluminescence of ZnS:Mn phosphors dispersed in polymeric material has been investigated on different methods: sliding deformation and impact testing. Because the commercial testing equipment is not designed for measuring the properties, it is important to develop such acquisition setups.

For a pin-on-disc triboluminescence measuring apparatus, it composes of three major sections: a mechanical loading mechanism, a load determination circuit and the optical measuring systems. Friction coefficient and a magnitude of normal forces can be simultaneously determined from a deflection of poly(methyl methacrylate) elastic arm. Voltage signals from the gauges are amplified by the cascaded operational amplifier ICs. This setup is used to investigate the influence of applied normal load, volumetric content of ZnS:Mn and frictional conditions. On the other hand, an impact testing method is employed for observing the effect of contacting geometries and impacting energy by utilizing different radius of glass pins and striking angles, respectively.

Stronger luminescence can be achieved by a) higher mechanical force/energy, b) reducing of contact area, c) increasing phosphor content in the composite and d) higher coefficient of friction. The results shows a linearity between total emission intensity and applied force/energy. It is important to notify the aforementioned conditions are accounted for high exerting stress.

Influence of phosphors content can be explained as a direct increase of light-emittable domain and an indirect governing factor on the effective mechanical properties of the composite. The latter can be confirmed by a noticeably change in track width and damages for different volumetric content of ZnS:Mn particles in the composite.

Modified Hertzian contact mechanics indicates the fact that there is not only a magnitude of force but also the mechanical properties and friction coefficient which govern the sub-surface stress. The von Mises stress which estimated from the response fields is assigned as a uniaxial compression. Luminescence quantity is found to be nonlinearly increased with the applied stress, however, the results are inconsistent to a simple quadratic; it is likely to resemble exponential function.

Taking into account a non-centrosymmetry of ZnS crystals and a conservation of energy principle, a piezoelectricity is responsible for the electromechanical coupling energy generation and therefore produces more energetic electrons. It is possible consider that the excited particles may deliberate from their shallow traps into conduction bands. Likewise a doping effect in semiconductors, the increment of electrons population in conduction band suggestively corresponds to the shift of Fermi level so that Fermi-Dirac distribution function can be employed for estimating the electron distributing probability and their population in conduction band of host crystals.

The process of triboluminescence proposed in the study are shown as follows:

1. Piezoelectricity-associated enthalpy is produced during the deformation of phosphors.

2. Electric enthalpy contributes to an increase of stored potential energy of electrons.

3. Electrons possibly escape from shallow traps and therefore increase the population of free electrons in conduction band.

4. Luminescent centers may capture holes from valence band while the excited electrons tend to return its lower energy state.
   $(Mn^{2+}) + \oplus \rightarrow (Mn^{3+})^*$

5. The excited electrons recombine with holes captured in the centers.
   $(Mn^{3+})^* + e^- \rightarrow (Mn^{2+})^*$

6. The emission of photon is an attribution of de-excitation of the centers.
   $(Mn^{2+})^* \rightarrow (Mn^{2+}) + h\nu$.

Mathematical model developed based on above mechanism is given as $A\left[\exp\left(Bx^2\right)-1\right]$ where a pre-exponential A includes the following factors: a detector efficiency, a spectral distribution, a volume fraction, and internal efficiency of luminescent centers while a piezoelectric property and crystallographic orientation of ZnS host crystals can be comprehended by an exponent coefficient B. Interestingly, its first-order approximation becomes a quadratic function which is consistent to the most frequently cited model.

To our knowledge, this is the first research in fields of mechanoluminescence that employs contact mechanics for direct calculation of the apparent stress. In spite of the fact that the theoretical model is relatively difficult to be implemented, it allows us for better understanding a correlation between stress-induced luminescence and external stimulation. Main advantage over the current model developed by *B.P. Chandra et. al* is a straightforward approach for determination of excited electron population in conduction band using well-know Fermi-Dirac distribution function.

However, the proposed theory is still incapable to explain an emission behavior of non-piezoelectric phosphors and a requirement of UV-irradiation prior to the measurement in doped $SrAl_2O_4$. Also, it is not suitable for describing time-dependence emission behavior due to an intensive application of statistic thermodynamics, solid-state physics and contact mechanics.

Publications

List of Publications

1. S. Leelachao, S. Muraishi, S. Tannomiya, J. Shi and Y. Nakamura, *Correlation of triboluminescence and contact stresses in ZnS:Mn/polymeric matrix composite*, J. Lumin. (2015). (Under the second review. Updated on September 26, 2015)

2. S. Leelachao, S. Muraishi, S. Tannomiya, J. Shi and Y. Nakamura, *Mechanoluminescence of ZnS:Mn phosphors and its correlation to impact energy and contact geometry*, Opt. Lett. **40** 4468–4471 (2015). Accepted.

List of Presentations

1. S. Leelachao and S. Muraishi. *A laboratory-scale pin-sliding instrument for triboluminescence measurement*. The 39th International Conference on Metallurgical Coating and Thin Films, San Diego, United states, April 2012.

2. S. Leelachao, S. Muraishi, T. Sannomiya, J. Shi and Y. Nakamura. *Structural and Optical Properties of Ion Beam Sputter Deposited ZnS:Mn Films*. The 8th International Forum on Advanced Materials Science and Technology, Fukuoka Institute of Technology, Fukuoka, Japan, August 2012.

3. S. Leelachao, S. Muraishi, T. Sannomiya, J. Shi and Y. Nakamura. *Stress-activated Light Emission Phenomenon of Mn-doped ZnS phosphors*. The 2nd ACEEES, Huntington beach, United states, December 2013.

Acknowledgments

First of all, I am deeply grateful to my academic supervisor, Associate Professor Shinji Muraishi, for offering the excellent opportunity by accepting as his student and providing efforts for teaching, giving good advises and supervision throughout the period of stay in Japan since Master degree. With his expertises, a large number of questions and inquiries are resolved as well as the superior guidances for researches. Importantly, he is not losing a faith and giving encouraging motivations. I would like to thank my academic advisor, Professor Yoshio Nakamura, for giving permission to join this laboratory, as well as Professor Ji Shi, for several helpful discussions relating to semiconducting materials.

Associate Professor Takumi Sannomiya is very appreciative of being as the *effective* supervisor during the first year of PhD student, introducing me to Professor K. Nakayama for gaining concepts for developing the early prototype of triboluminescent measuring setup, giving important discussions and *unofficial* lectures on the optical properties of materials and optical measurements and allowing of using his precious spectrometer.

Thanks to all previous and present members of Nakamura-Shi laboratory for their assistances, supports and entertainments during the period of student.

Special thanks are giving to Doctor Satoshi Someya as is one of few researchers on the field of stress-induced emission in Japan. Without a permission to visit his laboratory at AIST in Tsukuba, it was difficult to figure out the important instruments required for this study.

I would like to express my gratitude to my former advisor, Associate Professor Patama Visuttipitukul and Assistant Professor Tachai Luangvaranunt, for providing this invaluable opportunity for introducing this laboratory when the hope of finding the advisor in Tokyo Institute of Technology for application of the scholarship was nearly gone.

Speaking of friends, I am grateful to Mr. Sirichai Pornsarayuth for being as good senior, roommate and my first electronics-relating teacher, the amplifying circuits will not be successful if there were no answers from him. Also, Miss Rungrawee Wattanapornprom and Miss Chompunoot Wiraseranee are very supporting when the great depression attacked during staying in Japan. Especially, Mr. Chaiyapat Tangpatjaroen, the best friend and academic competitor since Bachelor degree in Chulalongkorn University.

Lastly, I would like to show my deepest loves for perpetual support and understanding to my parents and families. Their encouragement has brought me through difficult times. Without them, I may not be able to be strong and thinking positively for pursuing the excellency.